可應用於光學微機電系統之新型微致動器開發與整合

研究生：洪振鈞　　　　　　　　　　　　　　　　指導教授：邱俊誠 博士

國立交通大學電控工程研究所博士班

摘要

在光學系統的應用與整合上，微機電致動器扮演著相當重要的角色。由於對光學品質的要求，在致動器的設計上常常被賦予需要更平坦的鏡面以及能與系統做整合的要求。本論文分別針對結構鏡面平坦度以及高系統整合能力兩項需求分別設計且製作了全像 DVD 讀取時使用到的 phase shifter 及手機相機防手振時所需使用到的 image stabilizer 兩組元件。在 phase shifter 的設計製作中, 利用 TSMC 0.35 μm CMOS MEMS 製程製作 surface micomachining 元件, 經由後製程保留 40 μm 厚的質量塊達到鏡面平坦的要求, 並經由光罩設計以及 HF vapor 的後製程製作出 high filter factor(95%)之 phase shifter 元件。元件本身是利用 CMOS MEMS 製程所完成，相當適合進行元件與後續電路做整合規劃。在 image stabilizer 部分，利用 silicon on glass 以及 flip chip bonding 的技術分別設計出兩款不同的 MEMS image stabilizer，其高深寬比結構造就高驅動力與承載能力。由於其高深寬比結構可提供較強的結構剛性, 元件能夠與市售的 image sensor 做封裝整合。其作動規格符合 300~500 萬畫素之手機相機拍攝時進行防手振補償, 再者, 利用特殊的封裝技術將 image sensor 封裝在懸空的高深寬比微機電結構上並且進行打線作業。設計完成之 MEMS image stabilizer 僅有 500 μm 厚相當適合組裝於手機中, 進行手機防手振作業。

Design, Implementation and Integration of Novel Micro Actuators for Optical MEMS Applications

Student：Chen-Chun, Hung Advisor：Dr. Jin-Chern Chiou

Institute of Electrical and Control Engineering
National Chiao-Tung University

Abstract

MEMS actuators play very important rule in recent optical systems. Because of the requests of excellent optical quality and easy packaging function, optical MEMS actuators are usually designed with flatness reflection or diffraction mirrors, high suspended capability, and higher output force. In this dissertation, two kinds of optical devices, phase shifters and image stabilizers, are designed and fabricated and implemented. In the design of MEMS phase shifter, we utilize the TSMC O.35 μm CMOS MEMS foundry process to manufacture the micromirror array. CMOS foundry process offers the probability of easy integration of MEMS devices and circuits. To eliminate the warped phenomenon of micromirror array, a 40 μm reserved proof mass is designed and fabricated by the self-design post process. Furthermore, by the design of hidden net electrode, this device achieves a high fill factor of more than 90% without an additional flip-chip bonding process and is suitable to attach in holographic DVD pickup head for reading application. In the design of image stabilizer, the proposed stabilizers are designed as a two axis decoupling XY stages. By the design of high aspect ratio structure, this device is with large force output, and adequately strong to suspend an image sensor for anti-shaking photographic function. Furthermore, based on the design of the special wire bonding assisted holder, the image sensor can be successfully bonded to the image stabilizer. Additionally, electrical signals of the image sensor can be connected and integrated with the output circuits based on the signal spring design.

誌謝

敲了兩個月的鍵盤，終於敲到了誌謝這一欄。很不真實，卻由電腦裡諸多的研究數據與實驗結果分析資料夾中見到了由記憶斧鑿斑斑所留下的纍纍痕跡。終於夏蟬語語，鳳凰展豔，在送走多屆的碩班學弟後也該是我離開的時候了。

能讓自己順利的完成學業，步上人生另一個階段，心裡除了些許歡欣，些許離愁，卻也滿心由衷的感激。求學的路途上甚幸能夠跟隨邱俊誠教授，在其研究團隊中兢兢業業學習成長。無論是在研究上的指導以及生活上的照顧，學生感銘五內。

實驗室中一起成長的博士班師兄弟們，已經畢業的同學志良、以及尚在為畢業粹練的學弟們，禮忠、尚緯、志瑋、冠州、君穎、以及後續進來的學弟們，感謝各位在實驗以及研究上的討論與協助，方能讓我順利的拿到學位。希冀各位都能夠儘早拿到學位。當然，日後要喝酒唱歌，或甚騎車等活動，時間允許我也一定奉陪到底。

碩班的學弟們來來去去好幾屆，由衷的感謝你們，每每需要你們在實驗上的幫忙時總能得到你們適時的支援，感謝你們的協助，方能讓我順利的完成計畫的執行以及論文的成形。已經畢業的權隆、慶華等學弟，感謝你們對我論文上的幫助，不論是製程的支援以及圖檔美工的協助。正在為畢業努力的如錚、彥期、宗穎、永鋒以及彥樟，再堅持下去，學長相信你們都能如期畢業的。

最後，最最感謝的是來自家人的支持與鼓勵，感謝親愛的雙親，您們的生養教育以及鼓勵，讓我能在研究上無後顧之憂，感謝兄、嫂、妹妹、妹夫以及幾個小朋友一路相伴，在生活上以及精神上的支持，沒有你們一切的一切將不會如此圓滿。所有我所努力獲得的一切，吾願與您們一起分享。謝謝各位！！

振鈞 2010/06

CONCENT

中文摘要 I

ABSTRACT II

誌謝 III

CONCENT IV

LIST OF FIGURE VII

LIST OF LIST X

SYMBOL LIST XI

CHAPTER 1 : INTRODUCTION 1

1.1 MICRO-SYSTEMS BACKGROUND 1
1.2 REVIEW OF OPTICAL MEMS DEVICES 3
1.3 DISSERTATION WORK 9
1.3.1 Objectice 9
1.3.2 Outline 10

CHAPTER 2 : FABRICATION AND MANUFACTURE PROCESS 12

2.1 INTRODUCTION 12
2.2 BULK-MICROMACHINING 12
2.2.1 Si wet etching 13
2.2.2 Si dry etching 14
2.3 INDUCTIVELY COUPLED PLASMA ETCHING PROCESS 16
2.3.1 Icp etching mechanism 17
2.3.2 Bosch etching process 18
2.4 TSMC 0.35 μM CMOS MEMS 20
2.5 HF VAPOR ETCHING PROCESS 22
2.6 CONCLUSION REMARK 23

CHAPTER 3 : CMOS-MEMS ELECTROSTATIC MICROMIRROR ARRAY PHASE SHIFTER 24

3.1 INTRODUCTION 24
3.2 DESIGN CONCEPT OF MEMS BASE PHASE SHIFTER 27
3.3 THEORETICAL ANALYSIS AND FEM SIMULATION OF MEMS BASE PHASE SHIFTER 29
3.3.1 Static behavior 29

3.3.2 Resonant frequency 31
3.4 FABRICATION PROCESS OF MEMS BASE PHASE SHIFTER 33
3.5 EXPERMENTAL AND MEASUREMENT RESULTS OF MEMS BASE PHASE SHIFTER 36
3.5.1 Flatness of the micromirror 36
3.5.2 Static characteristic measurement 38
3.5.3 Frequency response measurement 40
3.6 SUMMARY 41
3.7 CONCLUSION REMARK 41

CHAPTER 4 : CMOS-MEMS HIGH FILL FACTOR MICROMIRROR PHASESHIFTER 42

4.1 INTRODUCTION 42
4.2 DESIGN CONCEPT 43
4.3 THEORETICAL ANALYSIS AND FEM SIMULATION 46
4.3.1 Static Behavior 46
4.3.2 Resonant Frequency 49
4.4 FABRICATION PROCESS 50
4.5 EXPERMENTAL RESULTS 55
4.5.1 Flatness of the micromirror 55
4.5.2 Static characteristic measurement 57
4.5.3 Frequency response measurement 58
4.6 SUMMARY 59
4.7 CONCLUSION REMARK 59

CHAPTER 5: DECOUPLING XY STAGE APPLICED IN CELLPHONE CAMERA IMAGE STABILIZER 60

5.1 INTRODUCTION 60
5.1.1 Introduction of MEMS image stabilizer 60
5.2 DESIGN CONCEPT OF MEMS IMAGE STABILIZER 62
5.2.1 Principles of operation of electrostatic comb-drive actuator 62
5.2.2 Design of decoupling structure 63
5.2.3 Design and calculation of range of motion of decoupling XY stage 68
5.3 FEA MODELING STRUCTURE 69
5.3.1 Static simulation 69
5.3.2 Dynamic simulation 71
5.4 FABRICATION PROCESS 72
5.4.1 Fabrication of image stabilizer 72
5.4.2 ICP Etching uniformity 74
5.4.3 Design of ICP uniformity improvement by mask layout design 76
5.5 PACKAGING OF IMAGE STABILIZER 78
5.6 EXPERMENTAL RESULTS AND DISCUSSION 80
5.7 SUMMARY 82

CHAPTER 6: DESIGN, FABRICATION, AND PACKAGING OF MEMS IMAGE STABILIZER 83

6.1 INTRODUCTION 83
6.2 CONCEPT AND STRUCTURE DESIGN 83
6.2.1 Structure design of XY stage 83
6.2.2 Design and estimation of spring stiffness 86
6.3 SYSTEM MODELING AND FEA SIMULATION 89
6.3.1 Simulation of the main structure decoupling of the proposed image stabilizer 90
6.3.2 Simulation of the resonant frequency for the proposed image stabilizer 91
6.4 FABRICATION PROCESS 92
6.4.1 Fabrication processes of structure layer and substrate holder 92
6.4.2 Wire bonding and device packaging 97
6.5 RESULTS AND DISCUSSIONS 100
6.6 SUMMARY 102
6.7 CONCLUSION REMARK 103

CHAPTER 7: CONCLUSIONS 104

7.1 INTRODUCTION 104
7.2 CONTRIBUTIONS 104
7.2.1 Post process was developed to improve CMOS MEMS structure flatness and reach high fill factor of micromirror.. 104
7.2.2 MEMS Phase shifter and Image stabilizer were designed, fabricated and verified 105
7.2.3 Novel type image stabilizer applied in cellphone camera for anti-shaking function.......... 105
7.2.4 Novel packaging and wire bonding function assembled by flip-chip bonding technology.105
7.3 SUGGESSTIONS AND FUTURE WORKS.. 106

REFERENCES .... .107

LIST OF FIGURE

Figure 1.1 DMD (The Digital Micromirror) device....2

Figure 1.2 3D Michigan Probe array....2

Figure 1.3 SEM of two STEC micromirrors....5

Figure 1.4 Photograph of a micromechanical 2 × 2 optical fiber switch....6

Figure 1.5 The illustration of the H-beam optical switch device....6

Figure 1.6 Vertical mirror and fiber grooves for tapered fibers fabricated by DRIE Etching....7

Figure 1.7 Optical switch with a movable mirror driven by electrostatic comb structures....8

Figure 1.8 The post-flow for DRIE CMOS process for flat device application....8

Figure 2.1 MEMS applications using Si bulk micromachining....14

Figure 2.2 Illustration of RF-plasma dry etching....15

Figure 2.3 Plasma etching mechanism....16

Figure 2.4 Schematic diagram of an STS inductively coupled etch system....17

Figure 2.5 Illustration of helical coil chamber....18

Figure 2.6 llustration of Bosch process....19

Figure 2.7 High aspect ratio structure shaped by Bosch process....19

Figure 2.8 Cross-section view of the TSMC CMOS MEMS process....21

Figure 2.9 Post process of the TSMC CMOS MEMS process....21

Figure 2.10 HF vapor etching process....23

Figure 3.1 Illustration of holographic optical system....25

Figure 3.2 The schematic of the individual mirror pixel....28

Figure 3.3 The deformation of the simplified micromirror model with 70V dc bias voltage....31

Figure 3.4 The simulation result of Z-axis displacement versus voltage....31

Figure 3.5 **The diagram of clamped-clamped beam with a center mass 32**

Figure 3.6 **Post-CMOS fabrication process flow 35**

Figure 3.7 **SEM picture of phase shifter 36**

Figure 3.8 **WYKO interferometer 37**

Figure 3.9 **Surface flatness of the micromirror device 38**

Figure 3.10 **The experimental diagram of static characteristic measurement.....39**

Figure 3.11 **The static characteristic of the micromirror 39**

Figure 3.12 **The frequency response of the micromirror 40**

Figure 4.1 **The schematic of an individual mirror pixel.......................................45**

Figure 4.2 **The deformation of the actual micromirror model with 3V DC bias voltage 48**

Figure 4.3 **The simulation result of Z-axis displacement versus driving voltage.49**

Figure 4.4 **Post-CMOS fabrication process flow 53**

Figure 4.5 **SEM pictures of the proposed micromirror phase shifter...................54**

Figure 4.6 **X-direction surface flatness of the micromirror device 56**

Figure 4.7 **The static characteristic of the micromirror 57**

Figure 4.8 **The frequency response of the micromirror 58**

Figure 5.1 **Illustration of comb-finger pair driving principle...............................63**

Figure 5.2 **Schematic illustration of decoupling XY stage 64**

Figure 5.3 **Illustration of driving modes of decoupling XY stage.........................65**

Figure 5.4 **Illustration of folded-flexure spring 67**

Figure 5.5 **Illustration of relationship between number of blur pixels and hand shake angle 68**

Figure 5.6 **Decoupling simulation of the XY stage...70**

Figure 5.7 **Dynamic model shapes of XY-stage 72**

Figure 5.8 **Fabrication process flow of image stabilizer..74**

Figure 5.9 **Etching testing in different etching areas...75**

Figure 5.10 Illustration of bad etching uniform 75

Figure 5.11 Phenomenon of overetching in ICP releasing process without compensation design 77

Figure 5.12 Optical image and SEM images of MEMS-based XY decoupling stage 77

Figure 5.13 Flip-chip bonding process 78

Figure 5.14 Pictures of XY stage bonded to image sensor 79

Figure 5.15 Static measurement of XY stage 81

Figure 5.16 Measurement result of dynamic nature frequency 82

Figure 6.1 Illustration of driving modes of decoupling XY stage 85

Figure 6.2 Structure design of XY stage 87

Figure 6.3 Illustrations of (a) decoupling structures, (b) decoupling flexure beams and (c) folded flexure beams 89

Figure 6.4 Schematic of decoupling simulation 92

Figure 6.5 Fabrication process of device layer of the image stabilizer 95

Figure 6.6 Fabrication process of image stabilizer 97

Figure 6.7 Photographs of image stabilizer 97

Figure 6.8 SEM pictures of part of image stabilizer 98

Figure 6.9 Package and wire bonding process of the image stabilizer 100

Figure 6.10 Photographs of package and wire bonding process of the image stabilizer 100

Figure 6.11 Photographs of image stabilizer with wire bonding package 101

Figure 6.12 Static measurement of XY stage in X- and Y-directions 102

Figure 6.13 Measurement result of resonant frequency 103

LIST OF TABLE

Table 5.1 Specifications of the image stabilizer 67

Table 4.2 Specifications of the image stabilizer 90

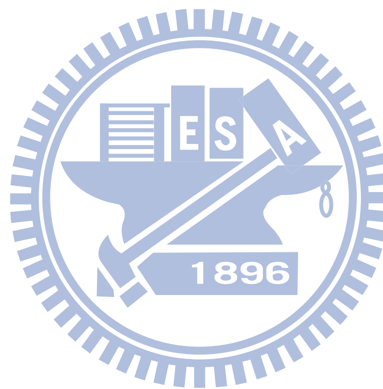

SYMBOL LIST

CHAPTER 3

ρ	Radius of curvature
ℓ	Half length of micromirror
d	The mirror peak-to-valley deformation
σ_A	The residual stresses of materials A
σ_B	The residual stresses of materials B
t_A	The thicknesses of materials A
t_B	The thicknesses of materials B
F	The electrostatic force in comb finger pairs
N	The number of comb fingers
C	The capacitance of comb fingers
V	The applied dc bias voltage
z	Displacement of movable fingers
ε	The dielectric constant in air
L	The finger length
g	The finger gap
n	The number of layers in the flexure beam
k	The equivalent spring stiffness of the micromirror
E_i	The Young's modulus of each layer
I_i	The moment of inertia of each layer
L_A	The length of the equivalent clamped-clamped beam

$\boldsymbol{m_A}$	The mass of the equivalent clamped-clamped beam
$\boldsymbol{M_A}$	The mass of the micromirror

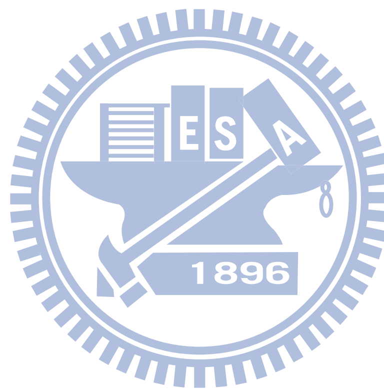

CHAPTER 4

F	The electrostatic force between the electrodes
C	The capacitance between the electrodes
V	The applied dc bias voltage
d	The gap between electrodes
z	The vertical displacement along the actuation direction
ε	The dielectric constant in air
A	The overlap area of top and bottom electrodes
k	The equivalent spring stiffness of the micromirror
n	The number of layers in the flexure beam
E_i	The Young's modulus of each layer
I_i	The moment of inertia of each layer
L_A	The length of the equivalent clamped-clamped beam
m_A	The mass of the equivalent clamped-clamped beam
M_A	The mass of the micromirror

CHAPTER 5

$\boldsymbol{U}$	The energy associated with the applied electric potential V
$\boldsymbol{F}$	The driving electrostatic force
$\boldsymbol{d}$	The gap between the fixed and movable comb fingers
$\boldsymbol{C}$	The capacitance between the fixed and movable comb finger
$\boldsymbol{N}$	The number of pairs of comb fingers
$\boldsymbol{V}$	The applied dc bias voltage
ε_r	The relative permittivity of the dielectric material
ε_o	The permittivity in air
$k_{x\text{-}system}$	The equivalent spring stiffness of the system in the X direction
$k_{y\text{-}system}$	The equivalent spring stiffness of the system in the Y direction
k_{fixed}	The fixed folded-beam spring stiffness
$k_{movable}$	The stiffness of the movable folded-beam spring in the X direction
$k_{x\text{-}fixed}$	The fixed folded-beam spring stiffness in the X direction
$k_{y\text{-}fixed}$	The fixed folded-beam spring stiffness in the Y direction
$k_{x\text{-}movable}$	The stiffness of the movable folded-beam spring in the X direction
$k_{y\text{-}movable}$	The stiffness of the movable folded-beam spring in the Y direction
$\boldsymbol{E}$	Young's modulus
I_a	The moments of inertia of beam a

I_b	The moments of inertia of beam b
L_a	The length of beam a
L_b	The length of beam b
k_{xx}	The stiffness of a single folded-flexure spring in the y-direction when the driven force is parallel to the x-direction
k_{xy}	The stiffness of a single folded-flexure spring in the y-direction when the driven force is parallel to the x-direction
k_{yy}	The stiffness of a single folded-flexure spring in the y-direction when the driven force is parallel to the y-direction
k_{yx}	The stiffness of a single folded-flexure spring in the x-direction when the driven force is parallel to the y-direction
BP	The blurring pixel
θ_L	The horizontal angle of camera
P_H	The total numbers of horizontal blur pixel
$F_{resonant}$	The resonant frequency
k	Stiffness of the device structure
M	The mass of the XY stage

CHAPTER 6

$k_{x\ decoupling\ beam}$	The stiffness of the decoupling beam of figure 6.3(b) in the x-direction
$k_{y\ decoupling\ beam}$	The stiffness of the decoupling beam of figure 6.3(b) in the y-direction
E_d	The young' modulus of the decoupling flexure beam in figure 6.3(b)
L_d	The length of the decoupling flexure beam in figure 6.3(b)
b_d	The width of the decoupling flexure beam in figure 6.3(b)
h_d	The thickness of the decoupling flexure beam in figure 6.3(b)
K_D	The stiffness ratio of the decoupling beam in figure 6.3(b)
$k_{x\text{-}folded\ beam}$	The stiffness of a folded beam in the x-direction in figure 6.3(c)
$k_{y\text{-}folded\ beam}$	The stiffness of a folded beam in the y-direction in figure 6.3(c)
E_f	The young' modulus of the decoupling flexure beam in figure 6.3(b)
L_f	The length of the decoupling flexure beam in figure 6.3(c)
b_f	The width of the decoupling flexure beam in figure 6.3(b)
h_f	The thickness of the decoupling flexure beam in figure 6.3(c)
$k_{x\text{-}system}$	The total stiffness of the main suspension beam in x-direction
$k_{y\text{-}system}$	The total stiffness of the main suspension beam in y-direction
k_{system}	The stiffness ratio of the proposed image stabilizer

$\boldsymbol{F_{resonant}}$	The resonant frequency
$\boldsymbol{k}$	Stiffness of the device structure
$\boldsymbol{M}$	The mass of the XY stage

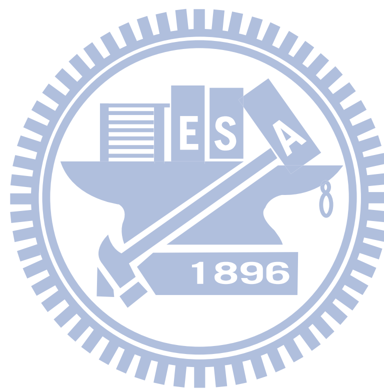

CHAPTER Ⅰ

Introduction

1.1 MICRO-SYSTEMS BACKGROUND

"Micro-Electro-Mechanical Systems" (MEMS) refers to a comprehensive integration technique for realizing various micro elements, including micro actuators, sensors, micro structures and others. In 1959, the Nobel Prize Winner, Dr. Richard P. Fenyman claimed, "There is plenty of room at the bottom," in an Annual Meeting of American Applied Physical Society [1], and said that he expected the vigorous development of MEMS in the future. In the past several decades, the small world has been an area of constant research in physics, biology, and engineering [2]. As the development of semiconductor fabrication approaches reaches maturity, various miniature MEMS devices are now designed, fabricated and realized to replace traditional elements. There are numerous advantages, including power saving, saving, shorter response times and others. MEMS devices can also be fabricated simultaneously with their driving or sensing circuits in a compatible IC manufacture process, such as a CMOS MEMS process. Recently, familiar MEMS devices not only in the consumer 3C market but also in medical treatment and disease detection. In the consumer 3C market, the MEMS technique is utilized to design and fabricate devices, such as micromirrors [3,4], accelerometers [5], inject printer heads [6], pressure sensors [7] and others. Figure 1 presents the well-known DMD (digital micromirror device), developed by Texas Instruments (TI), which is employed in projector lights, providing high-brightness, high-contrast, and high-reliability [8]. Accelerometers are typically embedded into airbags to detect and protect the drivers from serious damage when a car accident occurs [9].

The MEMS-based inkjet nozzle arrays provide a higher dpi resolution in printing pictures [10]. The MEMS-based pressure sensor can be attached to notebook computers for fingerprint identification [11]. In the medical field, the MEMS technique is employed to detect physiological signal , such as in EEG, EOG and EMG. Figure 1.2 presents Michigan Probe micro needle arrays, which are utilized as microscale neural sensors for recording chronic cortical signals [12].

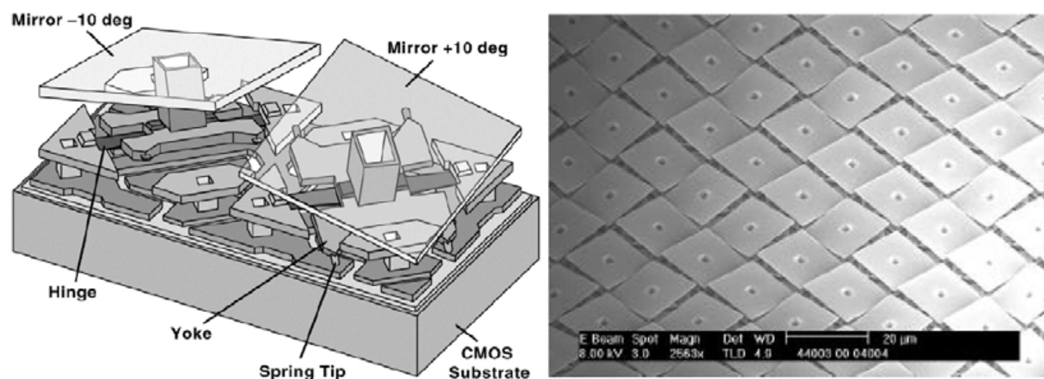

Figure 1.1 DMD (The Digital Micromirror) device [8]

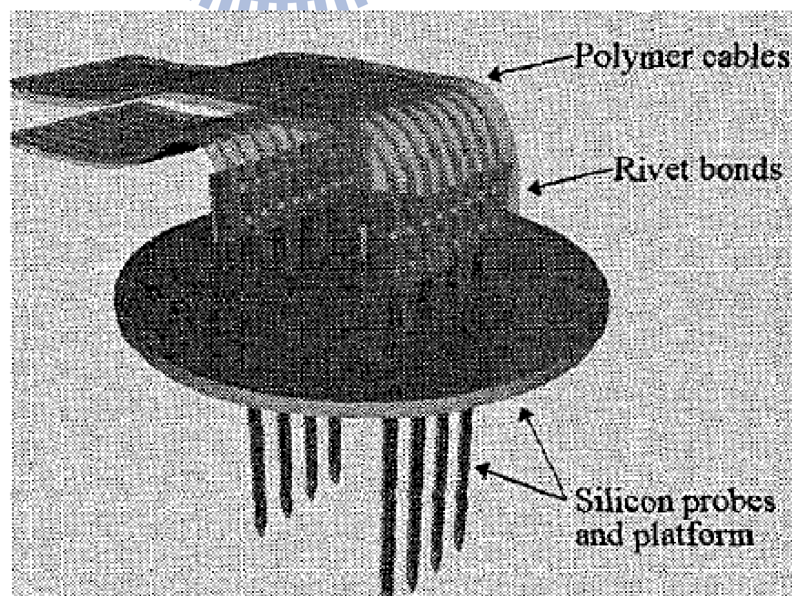

Figure 1.2 3D Michigan Probe array [12]

The fabrication of fundamental MEMS is based on the Si manufacturing process, which includes bulk micro machining and surface machining. In the future, to integrate devices and circuits, Si-based machining will still play the most important role in the fabrication of MEMS and the realization of the system-on-a-chip concept. However, in the bio-MEMS field, the most important issue is the safety of the materials used in MEMS devices. Accordingly, alternative fabrication processes that use more biocompatible materials and protect human health, such as PDMS hot embossing, are applied developed. With a diversity of design functions and manufacturing processes, the MEMS approach provides various means of overcoming design limits and of increasing the output of the IC and medical industries.

1.2 Review of Optical MEMS Devices

The fabrication of fundamental MEMS is based on the Si manufacturing process, which includes bulk micro machining and surface machining. In the future, to integrate devices and circuits, Si-based machining will still play the most important role in the fabrication of MEMS and the realization of the system-on-a-chip concept. However, in the bio-MEMS field, the most important issue is the safety of the materials used in MEMS devices. Accordingly, alternative fabrication processes that use more biocompatible materials and protect human health, such as PDMS hot embossing, are applied developed. With a diversity of design functions and manufacturing processes, the MEMS approach provides various means of overcoming design limits and of increasing the output of the IC and medical industries.

The use of the MEMS technique for fabricating optical systems can be traced back to the early 1960s. Today, it has an more important role in the manufacture of optical devices. Various key

components in the optical system have been replaced by MEMS devices. Typical MEMS actuators, including micro-mirrors, shutters or structures integrated with optical systems and related circuits, are abundantly available in the consumer electrical market. The MEMS technique is mostly employed to fabricate optical components for optical displays and telecommunication systems. In a projector display system, the DMD (digital micromirror device) is critical [8]. In a telecommunications system, dynamic optical add–drop multiplexers (OADM) [13], two-dimensional (2-D) optical crossconnects (OXC) [14]–[15], three-dimensional (3-D) OXC [16], [17], wavelength-selective switches [18]–[21], variable optical attenuators (VOA) [22], tunable wavelength filters [23], and wavelength tunable vertical-cavity surface-emitting lasers (VCSEL) [24], [25] are adopted as domain devices [26,27].

Regarding the optical system, when considering the needing of higher mirror flat accuracy, smooth structures and larger device size, characteristics of surface machining MEMS devices usually can not to satisfy those issues. Surface-machined MEMS devices generally cannot deliver to meet the requirements of high mirror flatness, smooth structures and larger devices, because the residual stress created in the fabrication process seriously deforms the large thin film structure and inhibits its application in optical domain. High-aspect-ratio structures (HARS) are utilized in optical MEMS systems because they support greater flatness of reflection or diffraction mirrors, high suspension capacity, and higher driving force. The residual stress induces less warping in bulk micromachined MEMS devices than in surface micromachined MEMS devices, because the form have high-aspect-ratio structures and higher structural stiffness. When in high-frequency operating mode, dynamic structural deformation always occurs in surface-micromachined MEMS devices, limiting the designed optical resolution [28,29]. In 2002, Robert A. Conant *et al.* presented a Staggered Torsional Electrostatic Combdrive (STEC) fabrication process for

ES A 1896

fabricating mirrors with high aspect ratios with high-torque actuators, allowing high-speed optical scanning with large angular deflections [30]. Figure 1.3 presents a 550 mm-diameter mirror that can be used to scan through an optical angle of 24.9° at a 34 kHz resonant frequency with a static and dynamic deformation of less than 30 nm.

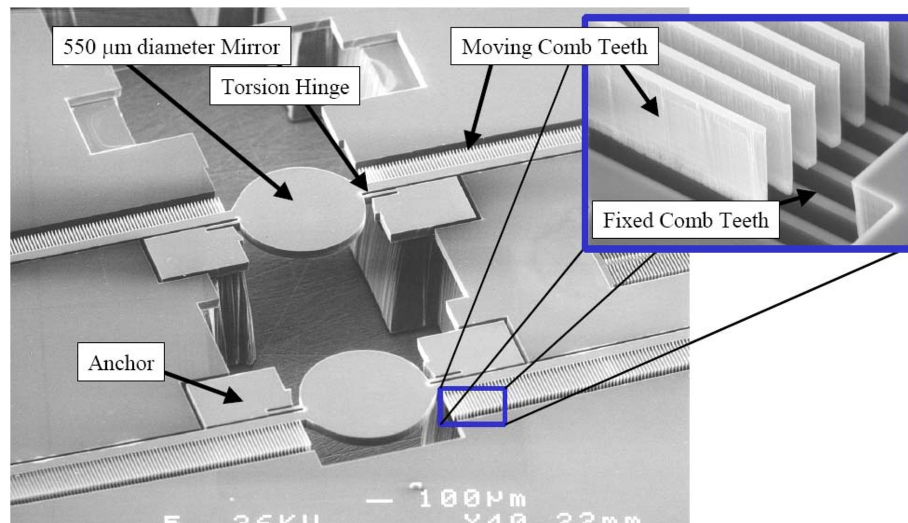

Figure 1.3 SEM of two STEC micromirrors [30]

1896

Devices with bulk structures are commonly adopted in optical fiber switches because of their high stiffness and high actuation force. Peter Kopka *et al.* presented thermally-driven coupled cantilever actuators in micromechanical 1 × 4 and 2 × 2 optical fiber switches for multi-stable switching. Figure 1.4 presents the design of coupled U-shaped cantilevers that allow a lateral movement of optical fibers to eliminate angular displacements [31]. To trap optical fiber and enable to move through a large distance, this actuator is designed with high aspect ratio and a height of 85um. Another design fixes the optical fiber and exchanges the transmission of light using an optical switch. W. C. Chen *et al.* presented an H-beam actuator, a reflective micro-mirror,

and an arched buckle spring to demonstrate a new compact latched 2 × 2 optical switching device. The measured optical switching characteristics include a switching time of 5 ms under a 25 V dc pulse back reflection loss of −52 dB, a cross-talk of −60 dB, an insertion loss of 0.8 dB, a polarization-dependent loss of 0.03 dB, and a wavelength-dependent loss of 0.11 dB [32].

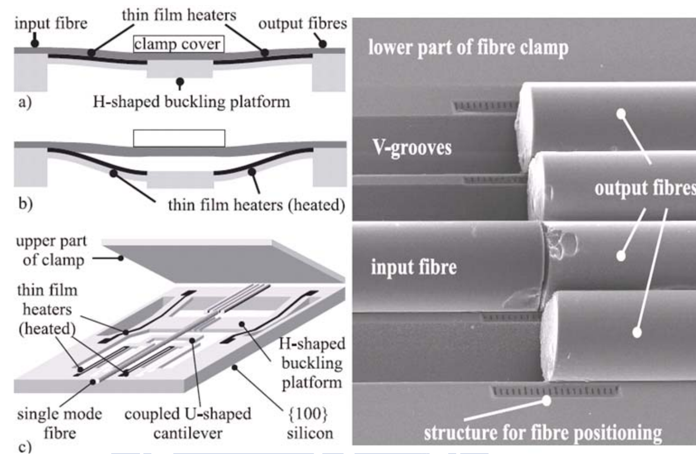

Figure 1.4 Photograph of a micromechanical 2 × 2 optical fiber switch [31]

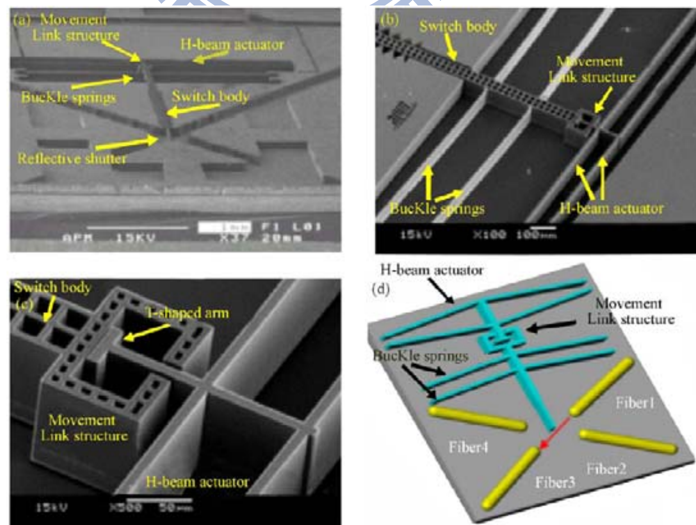

Figure 1.5 The illustration of the H-beam optical switch device [32]

Most of the MEMS actuators applied in optical system are designed as electrostatic actuator because of its integration feasibility with driving circuits, scalability for a large mirror array of devices and low power consumption characteristics. When considering with designing an electrostatic actuator with large driving force, it always involves high aspect ratio structure because the HARS can offer more parallel plates area and result in more electrostatic actuation force. Cornel Marxer et al. reported on vertical mirrors fabricated by deep reactive ion etching of silicon. The mirror height is 75 μm, covering the fiber core of a single-mode fiber when the latter is placed into a groove of equal depth and etched simultaneously with the mirror [33]. Figure 1.6 presents the Sutter-type vertical mirror for characterization of the mirror's reflectivity. The similar design also can be found in multi-direction mirror array. W. H. Juan et al. presented the design of High-Aspect-Ratio Si Vertical Micromirror Arrays for optical fiber switching [34]. Figure 1.7 presents the design optical switch with 800 μm -long, 3 μm -wide, and 50 μm -thick folded suspension beams. High-aspect-ratio Si dry etching technology allows tall and narrow fingers to be fabricated, which provide a large electrostatic force at low voltage to reduce power consumption. Accordingly, a switching array that can a lateral mirror movement of 34 μm at a low driving voltage of 30 V was realized .

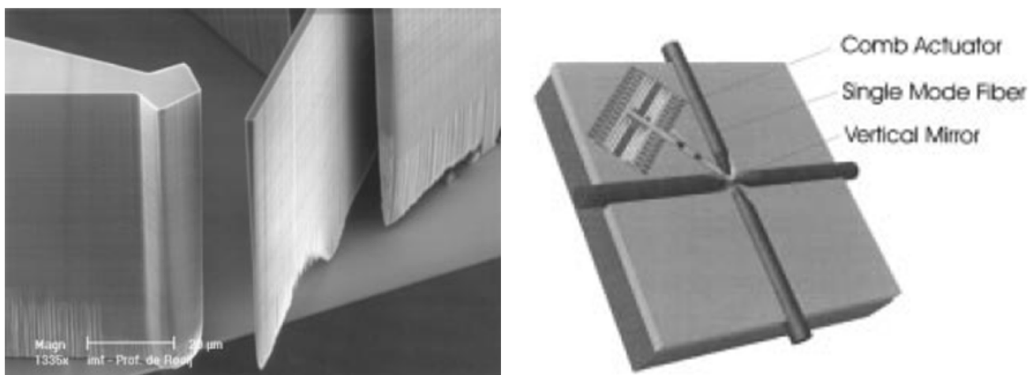

Figure 1.6 Vertical mirror and fiber grooves for tapered fibers fabricated by DRIE [33]

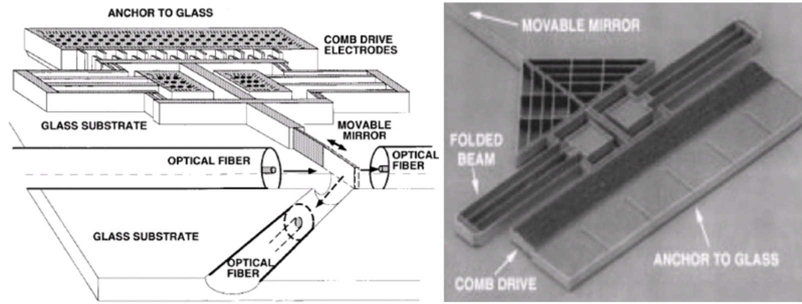

Figure 1.7 Optical switch with a movable mirror driven by electrostatic comb structures [34]

Some hybrid fabrications are applied to improve mirror flatness and integrate the micro actuator and circuits. In 2002, Huikai Xie et al. proposed the post-CMOS process integrated the CMOS thin film mirror and bulk structure to yield a flat structure, higher sensitivity, and lower driving voltage [35]. As shown in Figure 1.8, a deep RIE process is utilized to form high aspect ratio structure after the SiO_2 layer is released by RIE etching. Comparing to the traditional post release process, a high aspect ratio structure was saved under the thin film device and induced less

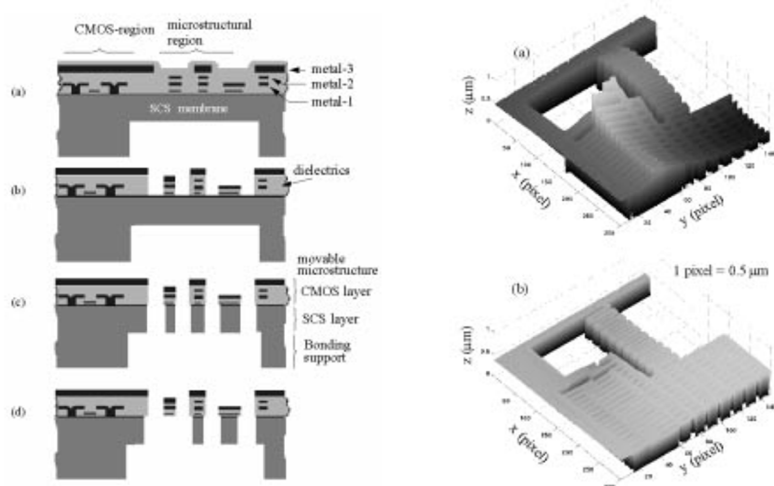

Figure 1.8 The post-flow for DRIE CMOS process for flat device and circuit integration [35]

1.3 DISSERTATION WORK

1.3.1 Objective

In various optical systems in the field of optical MEMS, not only the characteristic of flatness mirror surface, but also the large loading and actuation force play important roles in different type optical system. The main purpose of this dissertation is to elucidate various devices with bulk structures and various specifications applied in optical MEMS systems. The objectives of this investigation are as follows.

a. To develop a composite fabrication method for optical MEMS devices manufacturing and integration.
b. To design and fabricate CMOS MEMS phase shifter with very flat and high fill factor mirror arrays; and
c. To design and fabricate MEMS base image stabilizer with structures with high aspect ratio for a high structural loading and a large output force; and

In the first part of this dissertation, various fabrication processes for forming structures in this dissertation are introduced, including the ICP (Inductively Coupled Plasma) etching, CMOS MEMS process, and HF vapor etching process.

In the second part of the dissertation, we demonstrate two kinds of CMOS MEMS phase shifters with the characteristic of flat micromirror array. Two kinds of phase shifter micro-mirror

array are designed, fabricated and measured. The two phase shifters are fabricated by using the TSMC 2P4M CMOS MEMS foundry process and self-design post processes. By the special high aspect ratio back side proof mass design, the curved surfaces of micro mirrors are suitable eliminated, and the roughness of those two phase shifter will be reduced to the allowable range for blue ray DVD reading application. By special HF vapor fabrication and net electrode design, this phase shifter can achieve the characteristic of high fill factor and low actuation voltage.

In the third part of this dissertation, we demonstrate the MEMS base image stabilizer with aspect ratio structure applied in high loading capacity and large actuation force. Two kinds of image stabilizer are designed, fabricated, and measured. Owing to the designed structure with the high aspect ratio, those devices can load a 3 million pixel image sensor and move by controlled voltage. Meanwhile, the special self-design package function allows the MEMS-based image stabilizer to be fabricated with a small device thickness, making it is suitable for cell phones anti-shaking function.

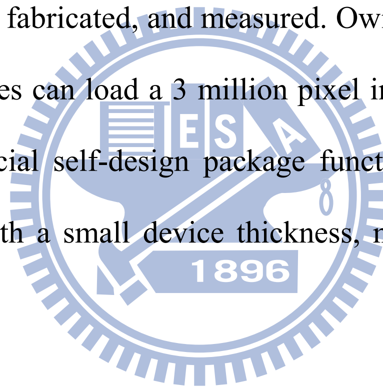

1.3.2 Outline

The dissertation is organized as follows. Chapter 2 introduces the fabrication process relative to this dissertation, includes the CMOS MEMS process, bulk micromachining, the ICP anisotropic etching process, the CMOS-MEMS process and the HF vapor process. Devices are fabricated using these procedures.

Chapter 3 and Chapter 4 describe two kinds of phase shifter array. These two phase shifters are designed and fabricated by the CMOS MEMS surface micromachining and self-design post

process. Under the CMOS MEMS surface foundry process, the phase shifter mirror is curved by residual stress. By the design of backside high aspect ratio proof mass reservation, the flatness of micro mirror array will be saved and suitable for blue ray DVD application.

Chapter 5 and Chapter 6 describe the large output and high loading ability of high-aspect-ratio device by two kinds of MEMS based image stabilizers. These two image stabilizers are design and fabricated by the silicon on glass process and flip-chip bonding technique, respectively. These two image stabilizers are capable of loading a 3 million pixel image stabilizer and can be driven with 25 μm displacement and excellent decoupling effect to be suitable for anti-shaping function applied in cell phone camera.

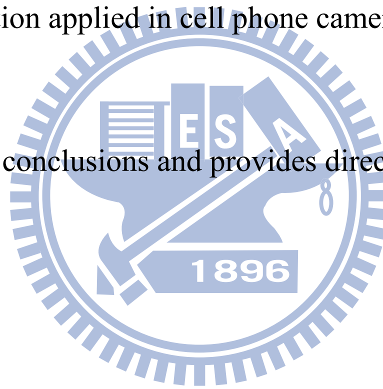

Finally, Chapter 7 draws conclusions and provides directions for future research.

CHAPTER Ⅱ

FABRICATION AND MANUFACTURE PROCESS

2.1 INTRODUCTION

In this dissertation, two phase shifters and image stabilizers are designed, fabricated, and packaged using several manufacture procedures. Besides the ICP etching process that is utilized to form a structure with a high aspect ratio, various fabrication processes are employed, including CMOS MEMS foundry and HF vapor etching process, to manufacture phase shifters, and a flip-chip bonding process is employed to package the image stabilizer. Section 2.2 presents a simple overview of the bulk micromachiningetching process used to form devices with high aspect ratios. Section 2.3 comprehensively discusses ICP etching process and its applications. Section 2.4 introduces the TSMC 2P4M CMOS MEMS foundry utilized in this dissertation. Section 2.4 introduces the HF vapor etching process.

2.2 BULK-MICROMACHINING

In MEMS development, Si MEMS fabrication plays the most important role so far because of its mature well-known technique and easy integrated with semiconductor fabrication process. In usual, Si MEMS process can be classified with surface micromachining and bulk micromachining. Bulk micromachining is commonly used to manufacture structures with high aspect ratios by etching Si substrates. According to the etch function, bulk micromachining can

be classified into wet etching and dry etching.

2.2.1 Si wet etching

Wet etching normally involves chemical etching using a liquid, such as HNA (HNO_3+HF), KOH, EDP and TMAH. Since the etching rate can vary with direction, wet etching is divided into isotropic etching and anisotropic etching. In isotropic etching, the etching rates are the same in all directions. For this method, the most common etchant is HNA [35]. Controlling the ratio of HNO_3 to HF enables Si etching at high etching speed or to produce a smooth surface. Anisotropic etching has different rates on different crystal planes. For this method, the most commonly used etching liquid is EDP [36], KOH [37], and TMAH. Generally, Si etching in the <111> direction is much slower than in the <110> or <100> directions. Si anisotropic etching can be utilized to shape various special structures, OR such as V-grooves, bridges, nozzles, and others, as presented in Fig. 2.1 [38,39].

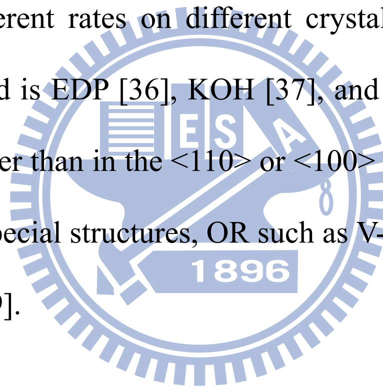

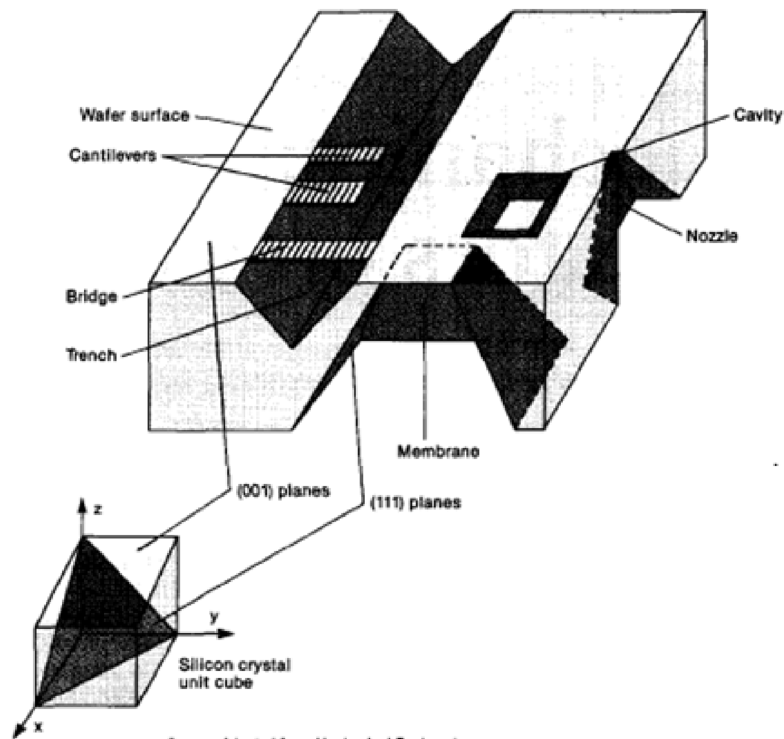

Figure 2.1 MEMS applications using Si bulk micromachining [39]

2.2.2 Si dry etching

In wet etching, the etch reactants are liquid and shape isotropic or anisotropic structures, but in dry etching, the etch reactants come form a gas or vapor phase source and are typically ionized. The difference between Si wet and dry etching is that the etchants of isotropic and anisotropic etching in dry etching are the same. Gaseous fluorine-based atoms or ions are generally utilized as the reactive species to etch the exposed Si film. This etching mechanism involves chemical and physical etching process. Si dry etching can also be classified into isotropic and anisotropic etching. This reaction of Si etching is isotropic and even provides less etching selectivity than wet etching. When the sidewall passivation function is introduced into the reactive process, Si

dry etching becomes anisotropic. Figures 2.2 and 2.3 show the Si dry etching mechanism. In the chemical mechanism, RF power generates fluorine-containing etching species, ionized species interact with the surface of Si, to yield volatile products, which are finally pumped away by a vacuum pump. In physical mechanism, gas ions are accelerated and strike Si substrate with high kinetic energy, some energy is then transferred to surface atoms, leading to Si removal. Chemical etching mechanism offers isotropic and high selectivity. On the contrary, physical etching mechanism offers highly anisotropic and low selectivity. In Si dry etching, the chemical and physical reactions occur simultaneously.

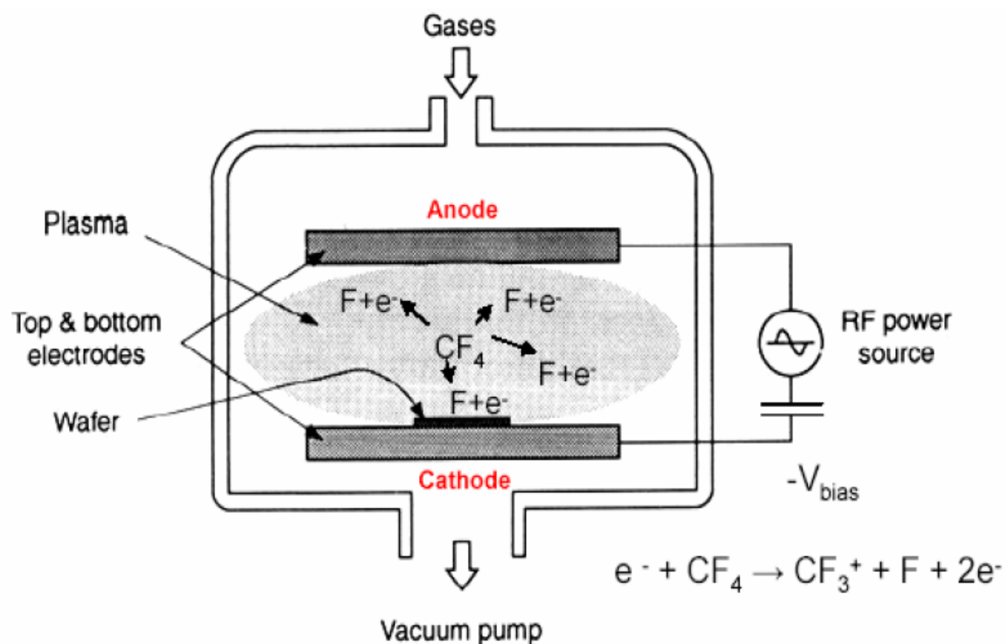

Figure 2.2 illustration of RF-plasma dry etching [40]

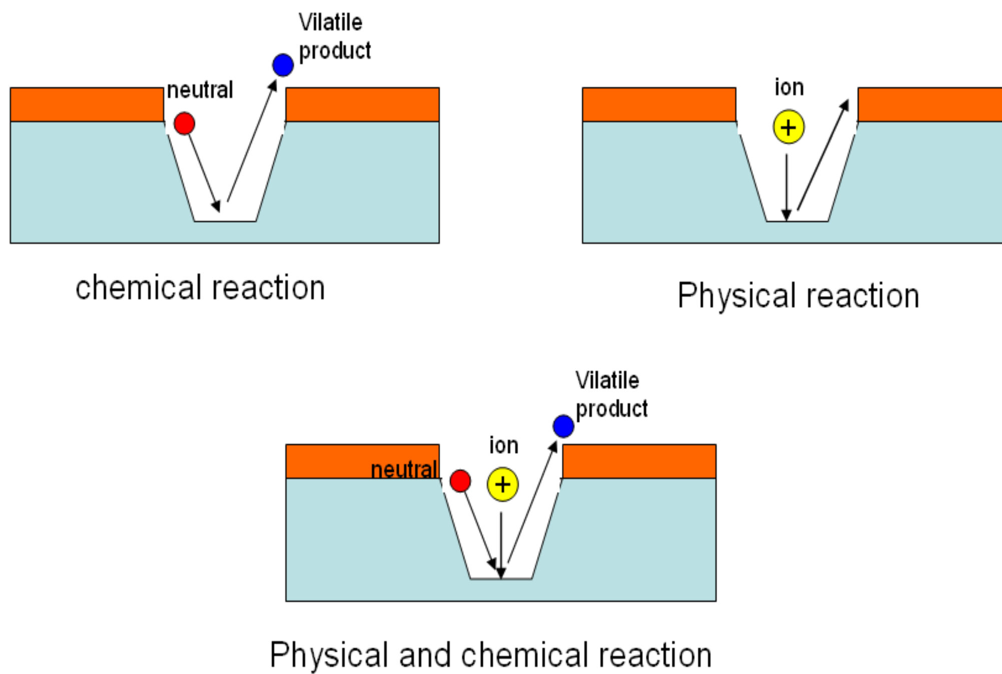

Figure 2.3 Plasma etching mechanism [41]

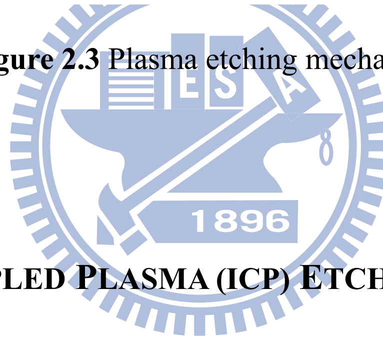

2.3 INDUCTIVELY COUPLED PLASMA (ICP) ETCHING PROCESS

As mentioned above, dry Si etching process can yield a structure with higher aspect ratio than wet Si etching. Many kinds of dry etching procedures can shape high aspect ratio structures, such as ICP (Inductively Coupled Plasma) etching electron cyclotron resonance (ECR), helicon, reactive ion etching (RIE), and others. Among those techniques, ICP etching provides the highest aspect ratio etching capability because of its greater scalability and wider operating window [42].

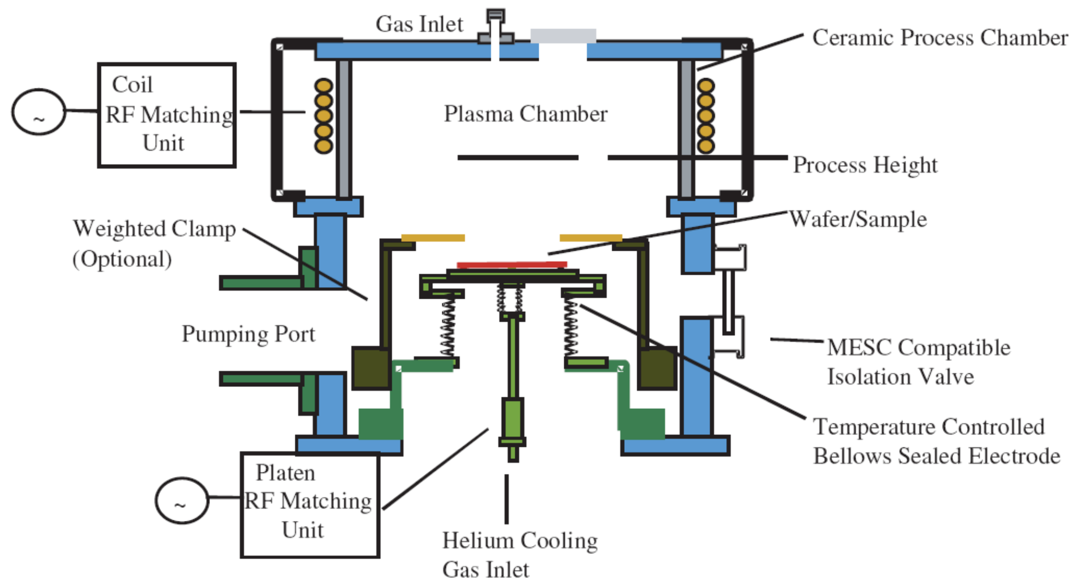

Figure 2.4 Schematic diagram of an STS inductively coupled etching system [42]

2.3.1 ICP etching mechanism

The ICP etching process is characterized by high etching rate and good sidewall angle control, based on the power control of high dense plasma. Figure 2.4 schematically depicts an STS inductively coupled etching system. Figure 2.5 displays the plasma generation system, which is established with an RF coupling electromagnetic field energy unit [43]. The ICP etching system has another helical coil RF matching unit, as well as the plated RF matching unit, to enhance the etching mechanism. In Si etching, the fluorine-based containing plasma can be obtained form various sources, such as SF_6 and CF_4. Then, more reactive ions are produced and accelerated by a helical coil RF matching unit, to bombard the Si wafer and increase the etching rate.

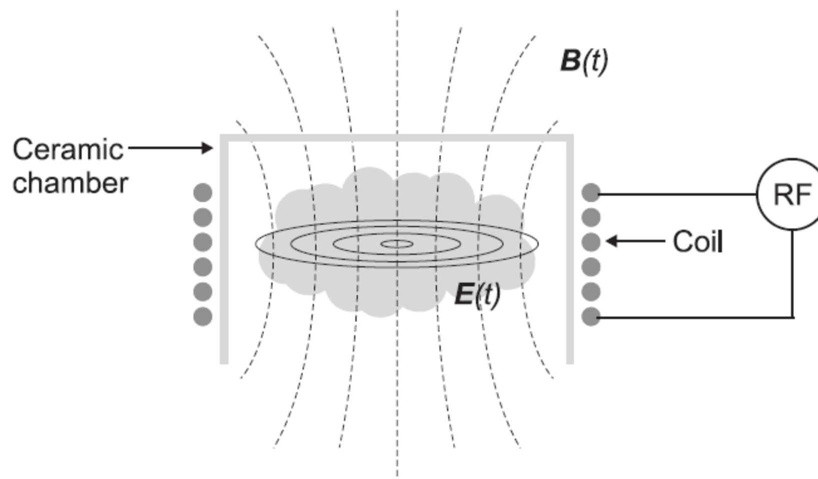

Figure 2.5 illustration of helical coil chamber [43]

2.3.2 Bosch etching process

The Bosh Company invented the Bosch etching process with alternate etching and passivation operation mechanisms. Besides the etching process, they introduced a passivation process into the reaction to protect the sidewall of the etching trench. By the protection mechanism, the Bosch etching process yields a structure with a higher aspect ratio than other etching mechanism. Figure 2.6 presents the reaction mechanism [44]. In Bosch processing with the etching step, SF_6 is utilized as the etchant source to provide fluorine-based etching species. In passivation processing, C_4F_8 is introduced to induce polymerization and form a polymer film to cover the Si surface. The fluorine-based etching species to bombard Si and the polymer film only in the vertical direction, leaving the sidewall. By this protection mechanism, the Bosch process can yield a structure with a high aspect ratio of more than 30:1 [45]. Figure 2.7 shows the high aspect ratio structure obtained by etching by the Bosch process.

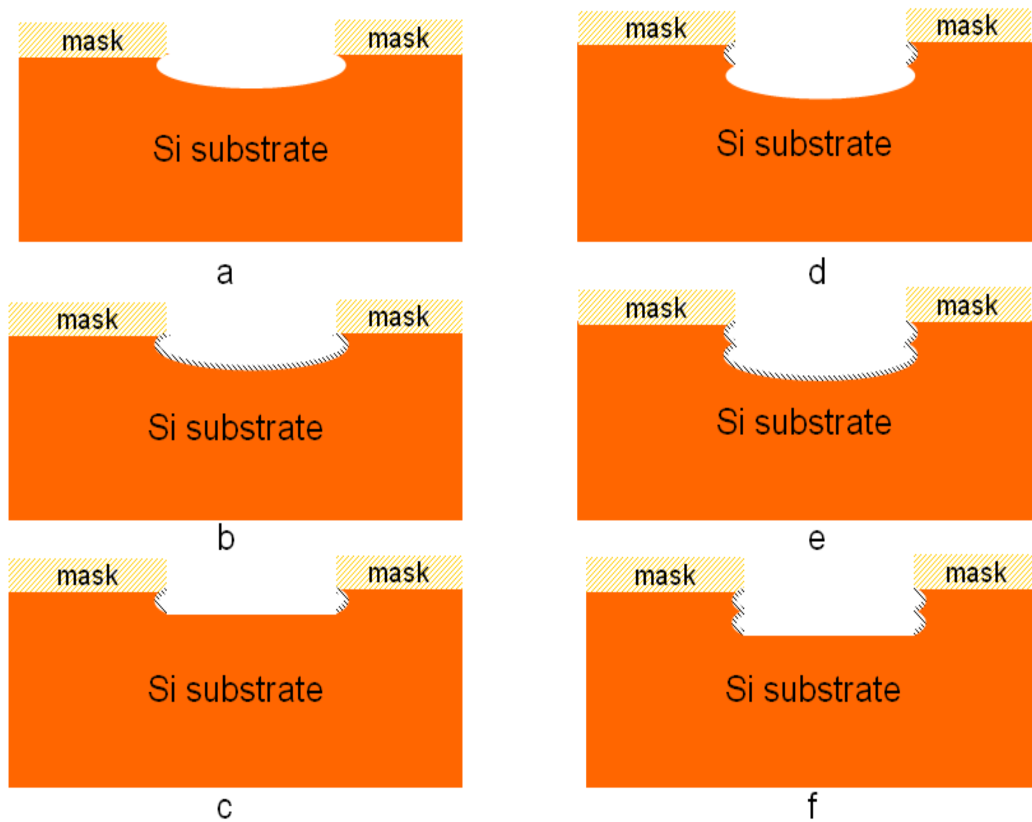

Figure 2.6 illustration of Bosch process

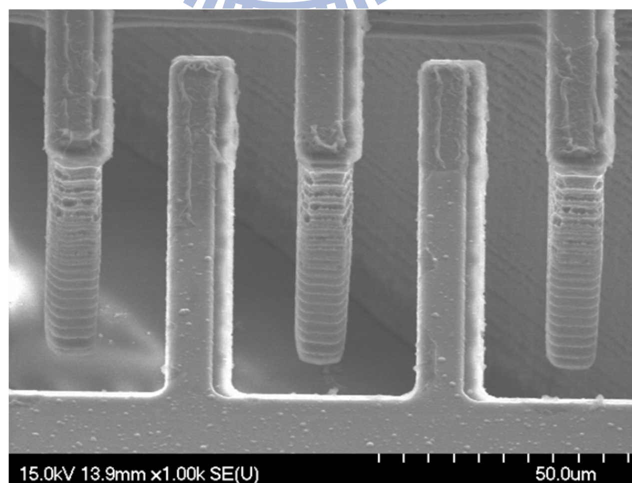

Figure 2.7 high aspect ratio structure shaped by Bosch process

2.4 TSMC 0.35 μm CMOS MEMS

In this dissertation, we utilized the TSMC 0.35 μm CMOS MEMS process to manufacturing phase shifter device in chapter 3. TSMC 0.35 CMOS MEMS is a foundry process developed by TSMC Ltd. Company (Taiwan Semiconductor Manufacturing Company). This foundry process is a two-layer polysilicon and four-layer metal surface micromachining technology. The difference from the standard CMOS process is an additional post ICP etching process is included into the CMOS MEMS process. As shown in Figure 2.8, TSMC 0.35 CMOS MEMS process provides two patterned layers of polysilicon for development of microstructure and four patterned layers of metal for circuit routing. If necessary, the metal layers also can be utilized as the device layers. The manufacturing process is shown as figure 2.9 [46]. After finishing the surface manufacturing step, user can open the desired windows of etching area by the RLS mask. An anisotropic RIE etching process is utilized to etch SiO_2 layer and form the device structure. Finally, the designed device is released by an isotropic Si etching process.

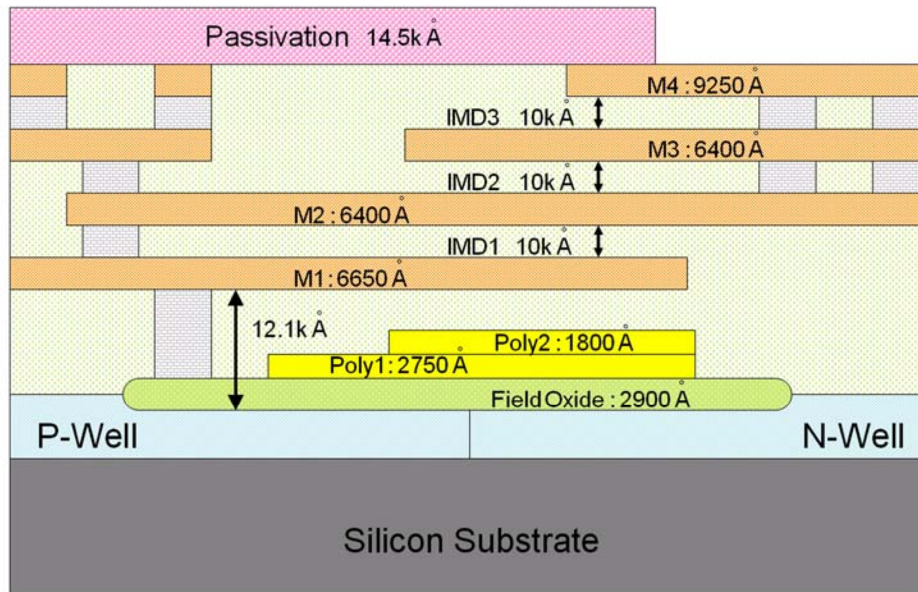

Figure 2.8 Cross-section view of the TSMC CMOS MEMS process [46].

Figure 2.9 Post process of the TSMC CMOS MEMS process[46] .

2.5 HF VAPOR ETCHING PROCESS

In this dissertation, in chapter 3, the HF vapor was utilized to dry-etch SiO_2 to design a phase shifter with a high fill factor. The HF vapor etching process is a dry etching approach for releasing MEMS surface micromachined devices with SiO_2 as a sacrificial layer. In HF wet etching process, drying of released wet etched structures however causes problems of stiction [47]. The normal solution to the problem of stiction is to use a CO_2 dryer to replace the liquid solution with CO_2 gas and to save the device by evaporating CO_2. This replacement process takes much time and money. HF vapor etching is a convenient and cheap method for releasing the device while avoiding stiction. In particular, when the wafer temperature during the release is increased above 40 ˚C, a high yield of surface micro-machined structures can be obtained.

Figure 2.10 presents the experimental setup for HF vapor etching. This process only requires that the HF liquid be heated above 40 ˚C to vaporize it. The processed chip and HF liquid are placed into a sealed space for safety and a light source is employed to heat the HF liquid. The etching rate at 40 ˚C is approximately 220 nm/min [48].

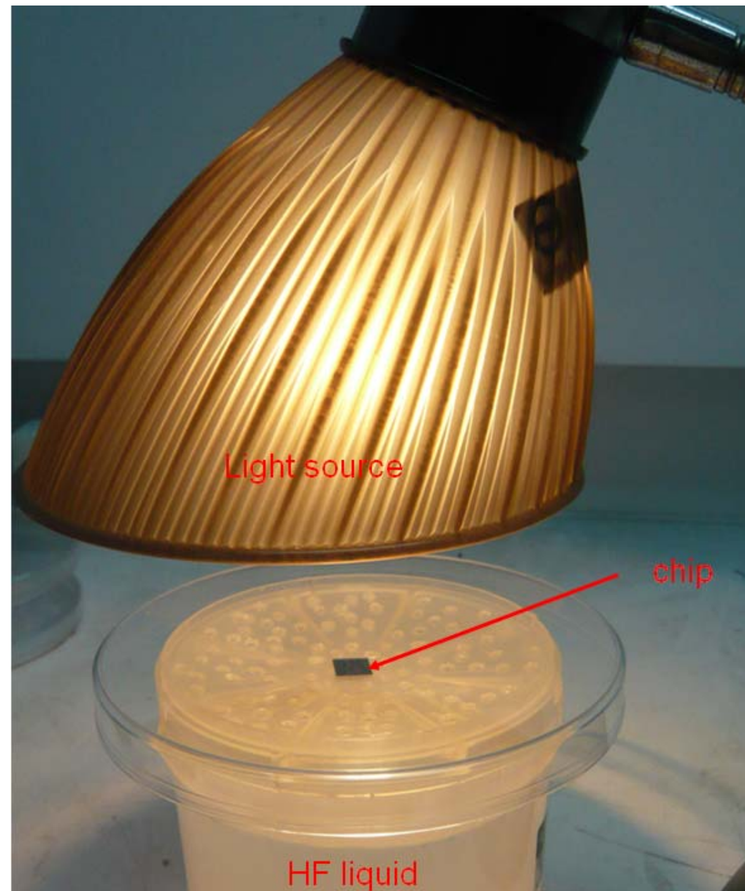

1896

Figure 2.10 HF vapor etching process

2.6 CONCLUSION REMARK

In this chapter, basic discussions of ICP fabrication technologies of are introduced. ICP etching process is the main technique to shape high aspect ratio structure and utilized in our whole devices. Another fabrication process such as TSMC 0.35 μm CMOS MEMS and HF dry etching process are also simple stated in the chapter. These two processes will be applied in the phase shifter manufacturing processes.

CHAPTER Ⅲ

CMOS-MEMS ELECTROSTATIC MICROMIRROR ARRAY PHASE SHIFTER

3.1 INTRODUCTION

In this chapter, we demonstrate the CMOS-MEMS electrostatic phase shifter array with flatness characteristic by high aspect ratio structure design, including design, fabrication, and measurement of two kinds of novel phase shifter. By suitable proof mass design, the flatness of micromirror of phase shifter can be effectively achieved.

Optical MEMS experienced a flourishing development in the past decade by leverage the IC micro-fabrication technology [49]. Its application includes projection displays [50], optical scanners [51] and imaging [52]. Among these devices, optical phase shifter plays an important role in light diffraction interference. As illustration in Figure 3.1, supposing a phase shifter can be operated at in-phase mode (0 degree phase difference) and out-of-phase mode (180 degree phase difference) respectively, the capacity of holographic data storage system will increase to 2 times. Further, the capacity will increase to 2^N times if N phase shifters are placed in the system [53, 54].

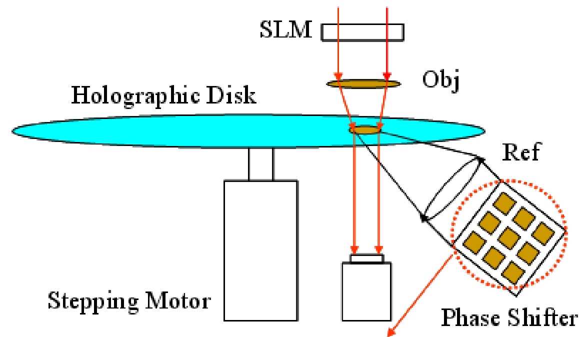

Figure 3.1 Illustration of holographic optical system

Among the existing actuation methods for MEMS mirrors that were previously proposed include thermal, piezoelectric and electrostatic. Thermal actuation is based on the difference between the thermal expansions of different materials in a bimorph actuation structure. This excitation principle is easy to implement, but requires high power consumption [55]. It is usually utilized in large displacement applications [51]. Piezoelectricity is often utilized phenomenon to excite a micromirror. However, piezoelectric material may cause hysteresis and is not compatible with CMOS process [56-57]. Electrostatic actuation is the most widely used in micromachined mirrors [58-61]. The main benefit of the electrostatic actuation is its characteristic in low power consumption and the capability of sub-micrometer displacement in optical device. The interferometry using electrostatic driven microactuator can precisely control displacements in nanometer range and the required actuation force is usually low [62]. Recently, many electrostatic actuation methods have been developed, such as the parallel plate, lateral comb drive and vertical comb drive structures. For vertical out-of-plane motion micromirrors with parallel plate electrostatic actuator exhibit a nonlinear phenomenon, called pull-in, which severely constrains the stable region at one-third the length of the gap [63, 64]. Electrostatic comb drive actuators were developed to avoid pull-in. Numbers of optical applications using electrostatic comb drive

micromirror have been demonstrated, such as optical scanners [65, 66], phase-shifting interferometer [67] and laser display [68].

Besides actuation methods, flatness of micromirror is also an important issue in designing MEMS mirrors. Micromirrors made of thin film materials usually suffer from surface curvature due to residual stress after the structure is released [69, 70]. Stress-induced out-of-plane deformation must be controlled small in comparison to the optical wavelength to avoid compromising device performance. Thus a number of methods have been proposed to eliminate curvature or reduce residual stress of the micromirrors. For example, a thick bulk-silicon micromirror fabricated via DRIE process can overcome the nonplanarity of thin film CMOS microstructures [71]. Moreover, ions bombard the surface of microstructure is also a way to modify the residue stress gradient [72-74].

In this chapter, the investigation develops an optical phase shifting micromirror array that can achieve $\lambda/4$ vertical displacement and make the mirror peak-to-valley deformation within $\lambda/10$. Electrostatic comb actuators are employed to drive each individual mirror pixel. The standard CMOS process and in-house post-CMOS process are utilized to fabricate the device. In the following sections, the design, theoretical analysis and simulation, and fabrication are given. Experimental results indicated that the micromirror demonstrated a vertical displacement of $\lambda/4$ at 38 V and the resonant frequency is 14.5 kHz.

3.2 DESIGN CONCEPT OF MEMS BASE PHASE SHIFTER

The optical phase shifting micromirror array is fabricated through TSMC (Taiwan Semiconductor Manufacturing Company) standard 0.35 μm 2P4M (double polysilicon quadruple metal) CMOS process [27]. The micromirror is designed to achieve $\lambda/4$ vertical displacement of 514 nm wavelength light source. Figure 3.2(a) shows the schematic drawing of individual mirror pixel. It consists of a 200 μm× 200 μm micromirror structure and four sets of comb fingers. The micromirror is supported by four flexures and the comb fingers are designed along the flexure, acted as the movable and fixed comb fingers. One end of the flexures is fixed to the anchor, and the other end is attached to the micromirror. The mirror reflective surface is made of aluminum metal layer with a high optical reflectivity better than 90%. A part of silicon substrate under micromirror is reserved for decreasing the mirror deformation due to residual stress after the structure is released, as shown in figure 3.2(b). Figure 3.2(c) shows cross-section view of the vertical comb drive actuator. The fixed comb fingers comprise M1, M3 and silicon dioxide, and the movable comb fingers comprise M2 and silicon dioxide. When a voltage is applied between the movable comb (M2) and fixed comb (M3), the micromirror can be pulled upward by the electrostatic force induced by the fringe effect. On the other hand, the micromirror can be pulled downward if the driving voltage applied to fixed comb is changed from M3 to M1. The multilayer structure enables the micromirror to have the vertical motion capability.

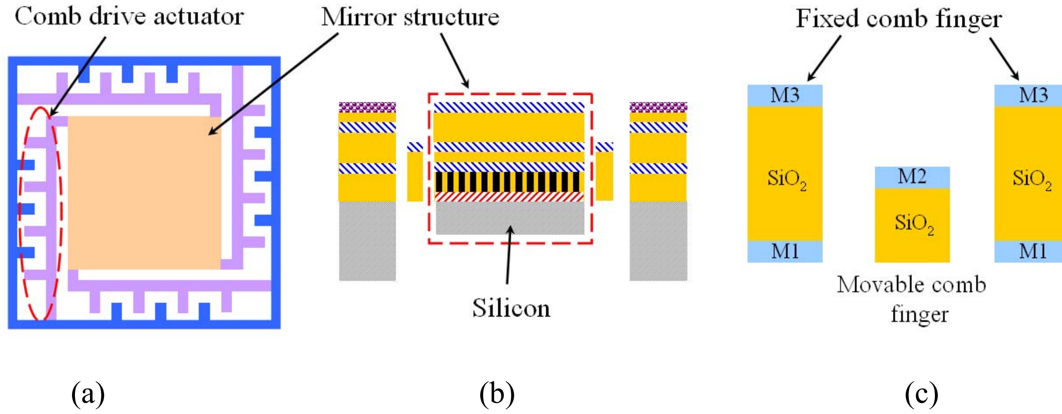

Figure 3.2 The schematic of the individual mirror pixel: (a) top view, (b) cross-section, (c) cross-section of the comb fingers.

A bulk-silicon under the micromirror is reserved for reducing mirror deformation due to residual stress after the structure is released, as illustrated in figure 3.2(c). The thickness of bulk-silicon is estimated according to the design specification that mirror peak-to-valley deformation is within λ/10 (51nm). In order to design the thickness of bulk-silicon, the curvature model is used for calculation. The curvature of a micromirror can be defined as [75].

$$\rho = \frac{\ell^2}{2d} \tag{3.1}$$

where ρ is the radius of curvature, ℓ is the half length of micromirror, and d is the mirror peak-to-valley deformation. Thus, the ρ must be larger than 100 mm to satisfy the d within λ/10. On the other hand, a beam curvature model also can be used in this design. Due to the micromirror deformation after release is bowl-shape, the center point can be regarded as an anchor. It is similar to the case that composite beam is bent by residual stress. Therefore, the curvature of the micromirror also can be expressed as [76].

$$\frac{1}{\rho}=\frac{6\left(m\cdot\sigma_B-\sigma_A\right)}{h\cdot E_B\cdot\left[3\cdot m+\frac{R}{q\cdot\left(1+q\right)^2}\right]} \tag{3.2}$$

where σ_A and σ_B are the residual stresses of materials A and B. E_A and E_B are the Young's modulus of materials A and B. The symbols $m=\frac{E_A}{E_B}$, $q=\frac{t_A}{t_B}$, $h=t_A+t_B$, and K is denoted as

$$R=1+4\cdot m\cdot q+6\cdot m\cdot q^2+4\cdot m\cdot q^3+m^2\cdot q^2 \tag{3.3}$$

where t_A and t_B are the thicknesses of materials A and B. K is a material coefficient of materials A and B. The material A in the micromirror structure denotes silicon substrate and material B is all used layers in CMOS process besides silicon. The material properties are taken from the National Chip Implementation Center [77]. Notably, silicon residual stress (σ_A) is neglected due to the bulk-silicon which reserved for reducing mirror deformation is treated as rigid body. Therefore, using equation (3.1) and (3.2), the thickness of bulk-silicon (t_A) can be calculated. The calculation result indicates that t_A have to be larger than 35 μm for satisfying the mirror peak-to-valley deformation within λ/10. To consider post-CMOS process variations, a 40 μm thick bulk-silicon will be reserved in the design.

3.3 Theoretical Analysis And Fem Simulation Of Mems Base Phase Shifter

3.3.1 Static behavior

The vertical motion of an electrostatic comb drive actuator occurs when a driving voltage is applied between the fixed comb fingers and the movable comb fingers. The electrostatic force is

given by

$$F = \frac{1}{2} N \frac{dC}{dz} V^2 \tag{3.4}$$

where N is the number of comb fingers, C is the capacitance of comb fingers, z is the displacement of movable fingers, and V is the applied dc bias voltage. For a comb finger pair, dC/dz can be expressed as

$$\frac{dC}{dz} = \frac{\varepsilon L}{g} \tag{3.5}$$

where ε is the dielectric constant in air, L is the finger length, and g is the finger gap. Using this in equation (3.4), the electrostatic force can be rewritten as a function of applied voltage.

To understand the static behaviors of the device, a FEM simulator, IntelliSuite®, is utilized to simulate the deformation and displacement of the micromirror. Figure 3.3 shows the simulation result of a simplified model of quarter micromirror with 70 V driving voltage. It is clearly that the displacement of the micromirror is the same with the free end of flexure beams. In other words, the deformation of the flexures induced by electrostatic force can fully pass to the micromirror and lead to a vertical levitation of the micromirror. Figure 3.4 illustrates the displacement of the micromirror versus driving voltage. The result indicates that the micromirror can achieve a 128 nm (λ/4) vertical displacement while applying voltage is about 42 V.

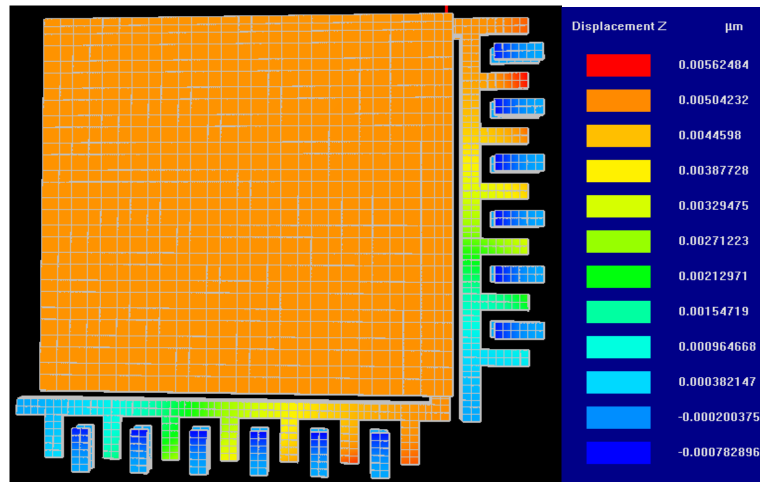

Figure 3.3 The deformation of the simplified micromirror model with 70 V dc bias voltage.

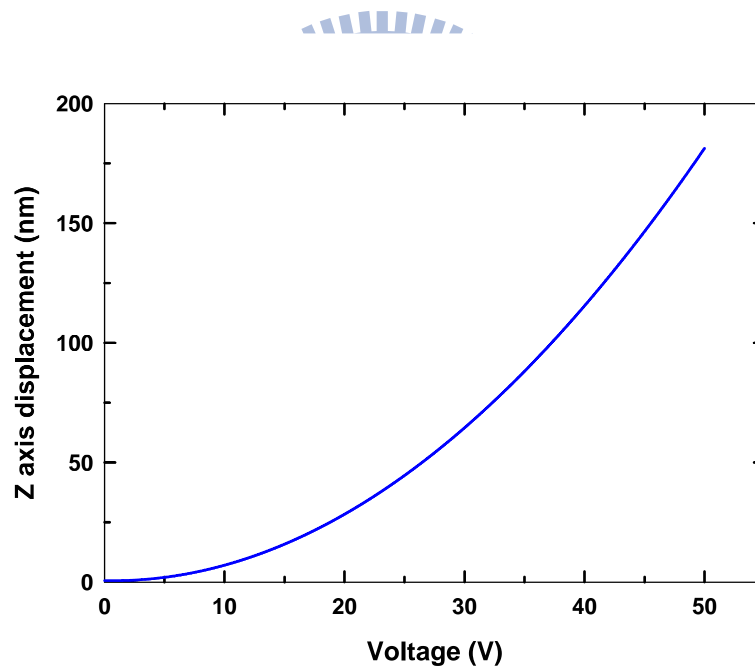

Figure 3.4 The simulation result of Z-axis displacement versus voltage.

3.3.2 Resonant frequency

A simplified theoretical model is used to calculate the resonant frequency of the proposed

micromirror device. The deformation of the flexure beams which induced by electrostatic force lead to a vertical levitation of the micromirror. Thus the device model is similar to the case that a clamped-clamped beam with a center mass, as shown in figure 3.5. Four flexures can be regarded as two sets of equivalent beams which act as a clamped-clamped beam. The fundamental resonant frequency of the equivalent model is expressed as [78]

$$f = \frac{4}{\pi}\sqrt{\frac{3\times\sum_{i=1}^{n} E_i I_i}{L_A^3 (M_A + 0.37 m_A)}} \tag{3.6}$$

where n is the number of layers in the flexure beam, E_i and I_i are the Young's modulus and the moment of inertia of each layer, L_A and m_A are the length and the mass of the equivalent clamped-clamped beam, and M_A is the mass of the micromirror. The theoretical resonant frequency is calculated at 4.08 kHz by using equation (3.6). On the other hand, the resonant frequency is also simulated by using IntelliSuite®. Note that in the present FEM simulations, we solely require movable comb, flexure beams and micromirror to calculate the resonant frequency. The simulation result indicates that the fundamental resonant frequency is about 4.45 kHz and the mode shape is vertical motion. These results can be used as the reference data in the actual experimental measurements.

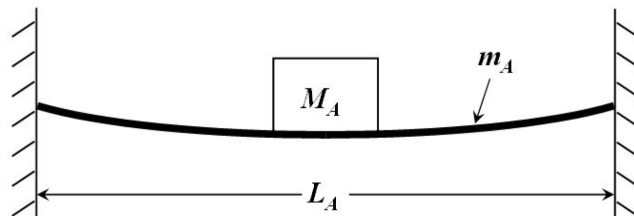

Figure 3.5 The diagram of clamped-clamped beam with a center mass.

3.4 FABRICATION PROCESS OF MEMS BASE PHASE SHIFTER

The proposed phase shifter device was fabricated by TSMC 0.35 μm 2p4m CMOS process which was provided by the National Chip Implementation Center (CIC) and a self-designed post-CMOS process. The CMOS process consists of two polysilicon layers, four metal layers, three via layers, and several dielectric layers. All metal layers are made of aluminum and the contact/via holes are filled with tungsten plugs. The dielectric layers are silicon dioxide and the passivation layer includes silicon dioxide and silicon nitride. The etched holes are filled with silicon dioxide. In order to fabricate a flat plane surface, chemical mechanical polishing (CMP) is employed after each deposition layer was completed.

After CMOS foundry process, all MEMS structures are bonded with the silicon substrate. Notably for device releasing issue, the passivation window of MEMS structure must be opened in advance of post-process. The self-designed post-CMOS process is applied to reserve a bulk silicon mass for reducing micromirror deformation and release the suspended structures. The post-process includes one grinding process, one backside alignment photography, a 2-step backside inductively coupled plasma (ICP) etching process, and a front-side reactive ion etch (RIE) step. Figure 5 illustrates the post-process flow. Figure 3.6(a) shows the device fabricated after the CMOS foundry process with the passivation window already open. A backside grinding process is then utilized to grind down silicon substrate thickness, reversing only 100 μm for economic considerations, as shown in figure 3.6(b). After that, a backside lithography process is applied to define the proof mass area, and then the first anisotropic ICP etching step is utilized to

etch the silicon substrate for proof mass reservation, in which PR is used as the hard mask, as illustrated in Figure 3.6(c) to 3.6(d). Figure 3.6(e) displays the second step in the ICP etching process. The PI tape is applied as the mask instead of PR. Although the ICP process will etch the PI tape, it will extend the etching time to form the proof mass. In this etching step, silicon dioxide is utilized as the etching stop layer due to the etching selectivity of silicon dioxide is significantly higher than that of PI tape. Finally, a front-side anisotropic RIE etching process is used to release the micromirror device, as shown in Figure 3.6(f). Figure 7 displays SEM images of the device fabricated using the CMOS process and post-CMOS processes. The suspended beams are slightly bent due to residual stress, as shown in Figure 7(c). However, this bending does not influence device actuation.

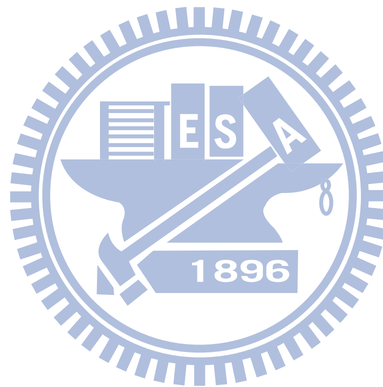

E S A
1896

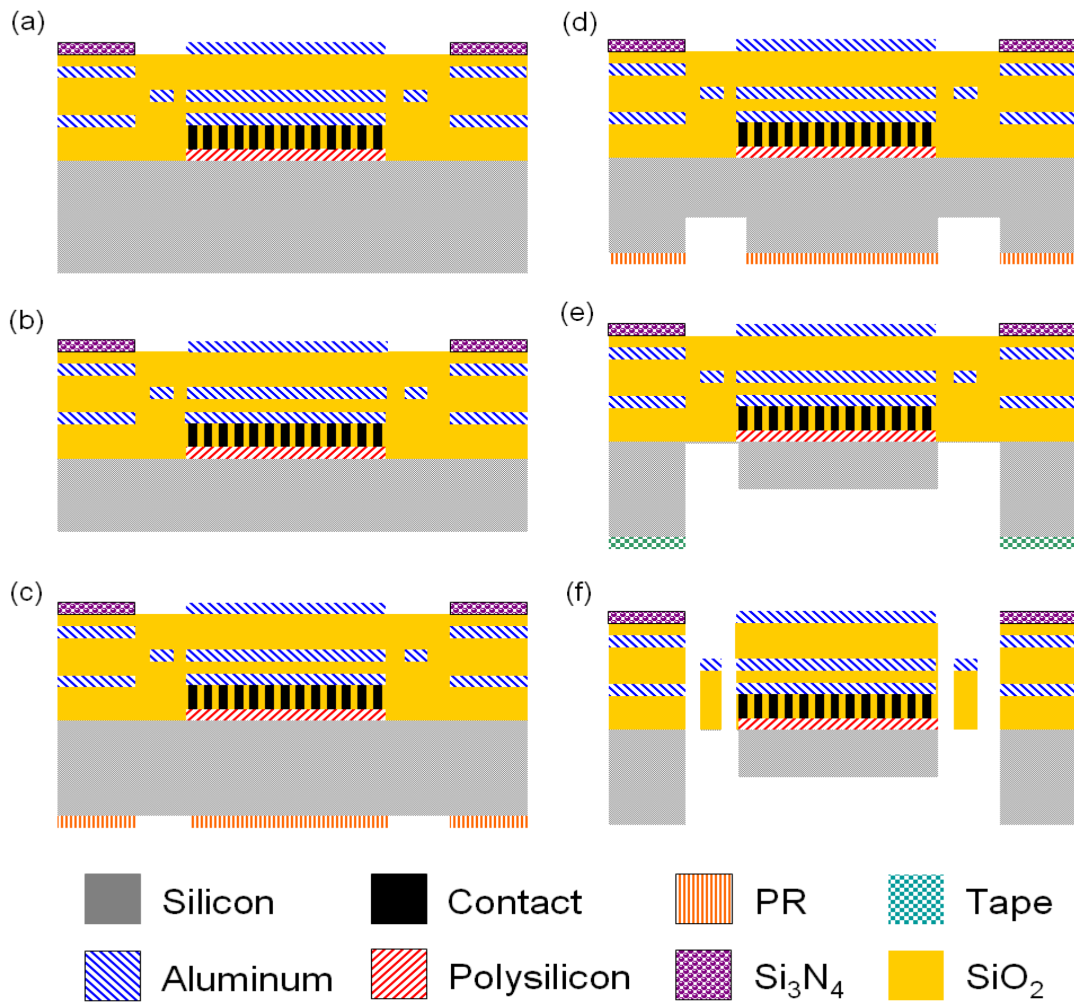

Figure 3.6 Post-CMOS fabrication process flow: (a) completion of CMOS process, (b) reserving only 100μm of silicon by grinding process, (c) defining proof mass area by backside lithography process, (d) first backside ICP etching step, (e) second backside ICP etching step, (f) front-side anisotropic RIE etching process to release suspended microstructures.

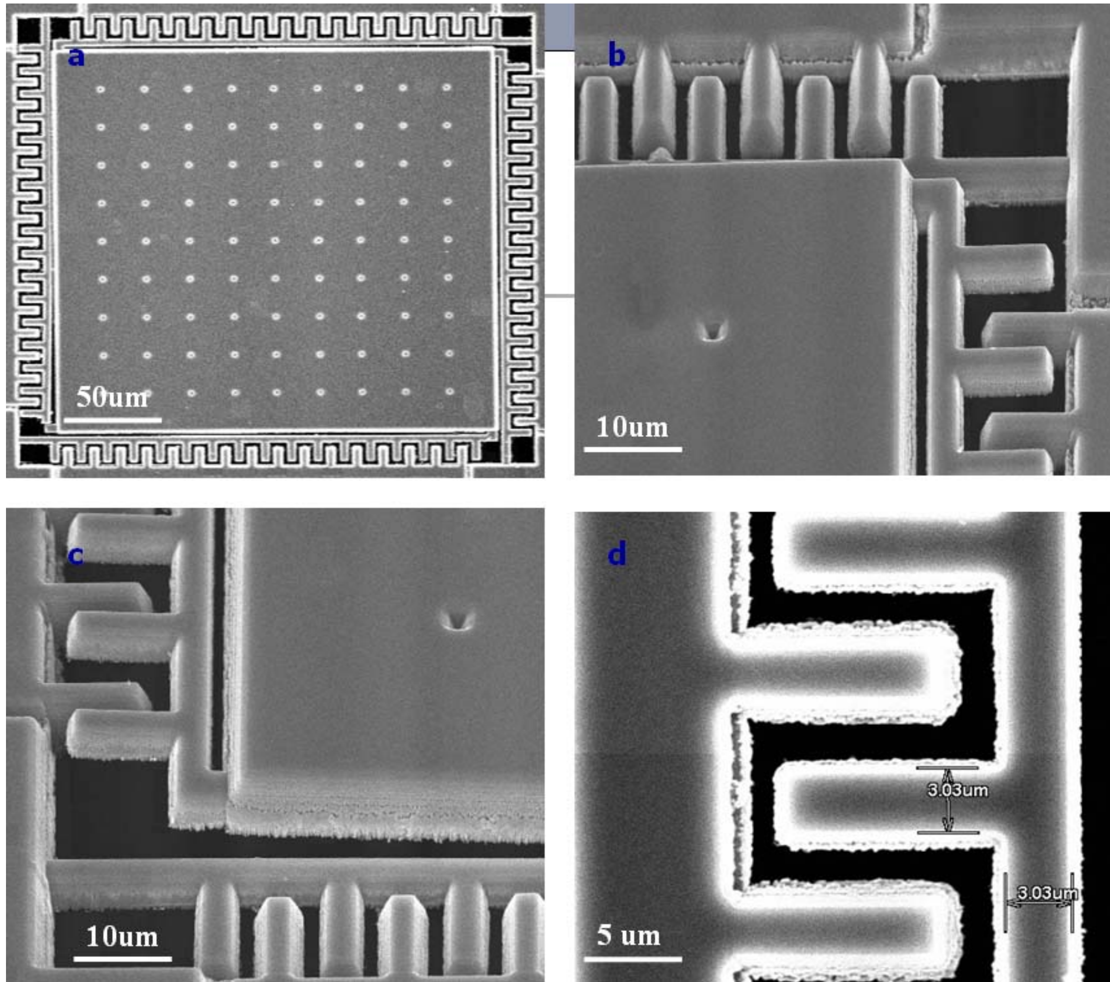

Figure 3.7 SEM picture of phase shifter

3.5 Expermental And Measurement Results Of Mems Base Phase Shifter

3.5.1 Flatness of the micromirror

In order to examine micromirror flatness, WYKO interferometer is used for the preliminary measurement, as shown in figure 3.8. Micromirror flatness is an important issue in phase shifter

applications. The X- and Y-directions of the micromirror surface are scanned. Figure 3.9 shows the X-direction roughness scanned at 200 μm distance from one side, passing through the mirror center to the other side. The measurement result demonstrates that roughness only about 60 nm and no mirror deformation occurred in this device. Deformation induced by residual stress from CMOS process is totally eliminated due to the curve is distributed uniformly and does not gather on any side of the mirror. A similar scanning result is obtained for the Y-direction. Thus, mirror peak-to-valley deformation conforms to the optical specification.

Figure 3.8 WYKO interferometer.

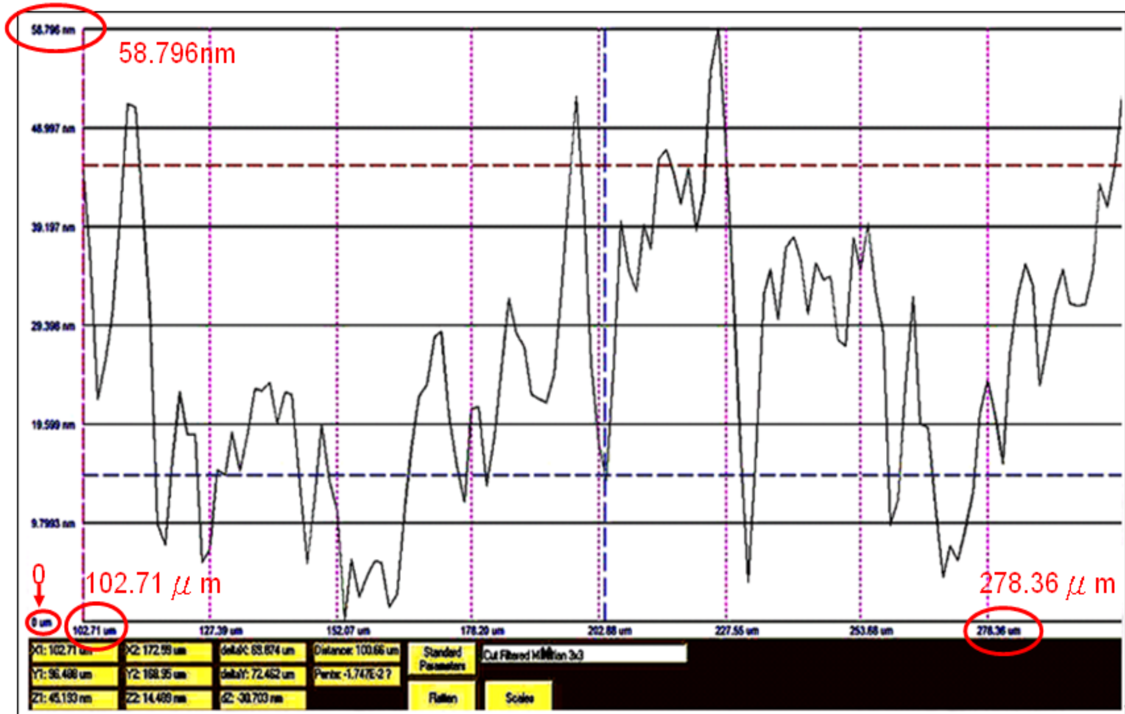

Figure 3.9 Surface flatness of the micromirror device.

3.5.2 Static characteristic measurement

The WYKO interferometer is also used for static characteristic measurement. Figure 3.10 shows the experimental setup. A dc bias voltage provided by the power amplifier is utilized to actuate the phase shifter micromirror. Figure 3.11 compares simulation and measurement results for vertical displacement versus driving voltage. The experimental result demonstrates that vertical motion of the micromirror can achieve a 128 nm displacement (λ/4 of the 514 nm light source) when 38 V are applied to the comb actuator. The vertical displacement of micromirror of 0~128 nm is obtained by increasing the driving voltage from 0 to 38 V; thus, the requirement of λ/4 displacement can easily be reached less than 40 V.

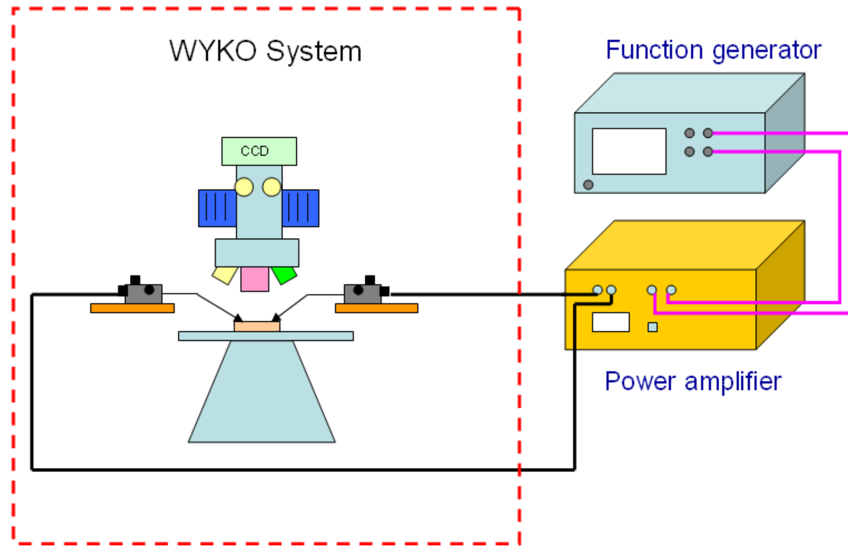

Figure 3.10 The experimental diagram of static characteristic measurement.

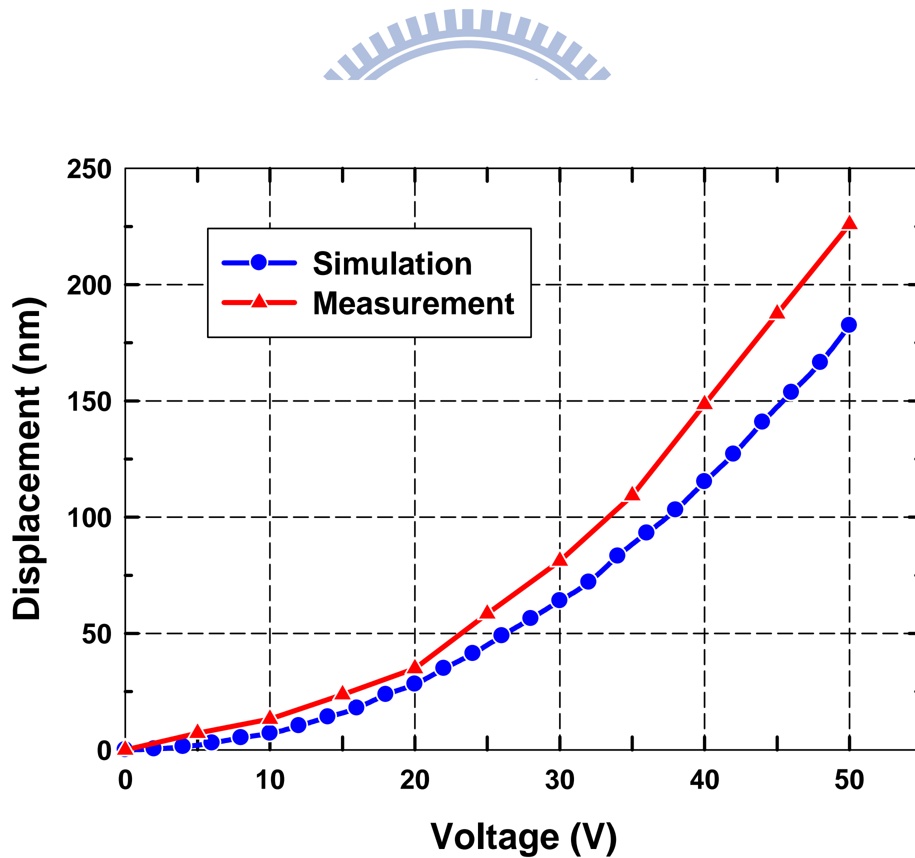

Figure 3.11 The static characteristic of the micromirror.

3.5.3 Frequency response measurement

Figure 3.12 shows the frequency response of the micromirror device that is measured by using an MEMS Motion Analyzer (MMA). The micromirror is biased by a sinusoidal wave with voltages offset of 30 V and amplitude of 5 V, and the frequency ranges between 2 and 5 kHz. The first resonant frequency mode is measured at 3.71 kHz, and it closely matches the calculation (3.98 kHz) and simulation result (4.15 kHz). The error is due to variations of the CMOS fabrication process and post-process. The quality factor is calculated at 41.

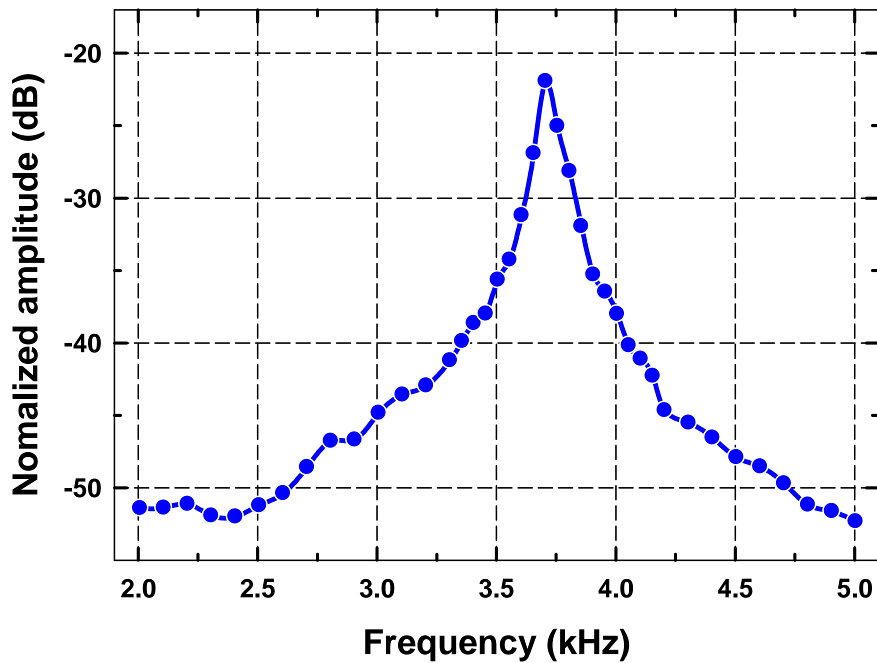

Figure 3.12 The frequency response of the micromirror.

3.6 Summary

This work presents a 3 × 3 electrostatic phase shifter micromirror array fabricated by TSMC 0.35 μm 2p4m CMOS process and the self-designed post-CMOS process. The individual mirror pixel is 200 μm× 200 μm. Mirror deformation resulting from residual stress of the CMOS process is eliminated via proof mass reservation design. The design, modeling, simulation and measurement are presented. Preliminary measurement results demonstrate that the micromirror can achieve a 128 nm (λ/4) vertical displacement with a driving voltage of 38 V and the resonant frequency is 3.71 kHz. This phase-shifting micromirror array has potential as a spatial light modulator (SLM) in holographic data storage systems in the future.

3.7 CONCLUSION REMARK

In this chapter, MEMS based phase shifter are designed, fabricated, and measured. By the design of high aspect ratio proof mass reserved under the micromirror fabricated by surface micromachining, warped phenomenon caused by residual stress can be effectively eliminated. Furthermore, it is very easy to integrate MEMS devices and circuits by utilizing the CMOS MEMS foundry process and easy post process.

CHAPTER Ⅳ

CMOS-MEMS HIGH FILL FACTOR MICROMIRROR PHASESHIFTER

4.1 INTRODUCTION

In chapter 3, we have successfully design and fabricate the phase shifter with flat mirror arrays. In this section, we will introduce another important issue in phase shifter design. In addition to mirror flatness, fill factor also plays an important role in optical applications. Previously reported micromirror arrays with a low fill factor resulted in low optical efficiency [79]–[80]. In order to achieve an effectively high fill factor, driving and suspension mechanisms usually must be placed under the mirror plate. The most famous example is the Texas Instruments Digital Light Processor (TI DLPTM) mirror system we mention in chapter 1 that has a complicated superstructure to obtain a high fill factor in projection display application [8]. Besides, additional assembly process such as flip-chip bonding technique is also utilized to place the mirror plate on top of the actuator stage [81]–[84].

In this chapter, we develop an optical phase shifting micromirror array with the same specification, can achieve a λ/4 vertical displacement and a mirror peak-to-valley deformation within λ/10 that. Furthermore, the fill factor is about 90% without additional flip-chip bonding process. Electrostatic actuators are employed to drive each individual mirror pixel. The standard CMOS process and in-house post-CMOS process are utilized to fabricate the device and offer the probability of the integration of mirror array and driving circuits. The following sections describe

device design, present theoretical analysis and simulation results, and provide fabrication details. Experimental results demonstrate that the micromirror had a vertical displacement of λ/4 at only 3 V and resonant frequency of 3.6 kHz.

4.2 DESIGN CONCEPT

This phase-shifting micromirror array is also fabricated by TSMC standard 0.35 μm 2p4m CMOS MEMS process. The micromirror is designed as the same specification to achieve a λ/4 vertical displacement for a 514 nm wavelength light source. Figure 4.1 illustrates the schematic drawings of an individual electrostatic driven mirror pixel. It consists of a 200 μm× 200 μm micromirror surface structure, suspension beams, net electrode, pillar-shape joiners, and proof mass. The micromirror is supported by two suspension beams and formed by metal 4 (M4), as shown in Figure 4.1(a). The mirror reflective surface is an aluminum metal layer with high optical reflectivity exceeding 90%. The suspended beams are designed to be under the mirror plate. One end of the beam is fixed to an anchor and the other end is attached to the micromirror.

An electrostatic parallel plate actuator drives the mirror. The top electrode is the mirror plate and the bottom electrode is a net electrode. The net electrode is a clamped-clamped suspension structure, which acts as a stator. It is composed of M2, M3, and a tungsten layer between M2 and M3. The gap between mirror plate and net electrode is 1μm, and one-third of the gap is larger than the desired micromirror motion displacement (128 nm). Therefore, the pull-in phenomenon can be avoided by applying a proper driving voltage. The same 40 μm-thick bulk-silicon under the micromirror is reserved for reducing mirror deformation due to residual stress after the

structure is released. In order to connect the mirror plate and silicon proof mass, pillar-shape structures are designed for connectors, as shown in Figure 4.1(b). The pillar-shape structure comprises all metal layers and tungsten via layers besides M4. The mirror and pillars act as a rotor. Figure 4.1(c) shows stereo drawing of the whole micromirror structure. The pillars pass through the net electrode; thus, the rotor does not touch the stator. When voltage is applied between the stator and rotor, the electrostatic force pulls the micromirror downward. Thus, the multilayer structure provides vertical motion capability. The micromirror array achieves a high fill factor of more than 90% without an additional flip-chip bonding process because of the parallel plate actuator and the hidden suspension beams.

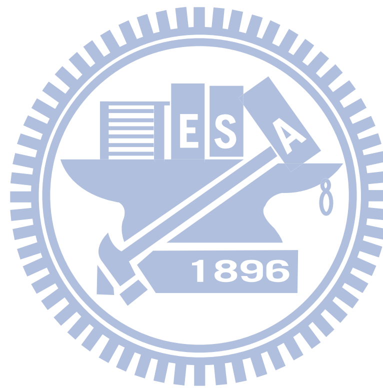

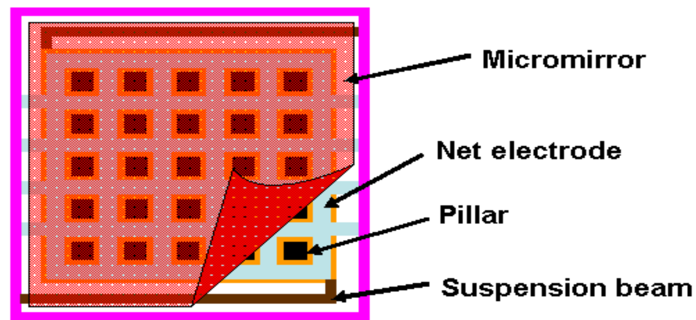

(a)

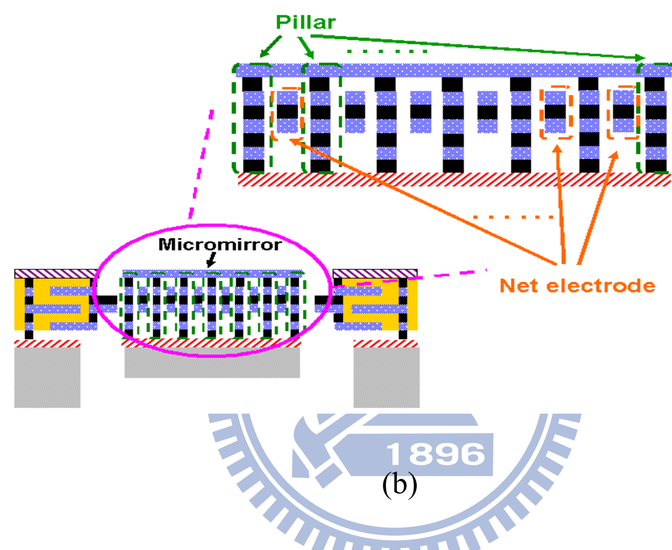

1896

(b)

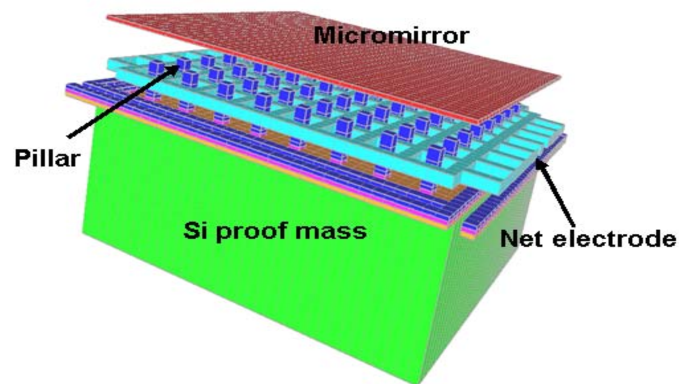

(c)

Figure 4.1 The schematic of an individual mirror pixel: (a) top view, (b) cross-section view, (c) stereopicture of the micromirror.

4.3 THEORETICAL ANALYSIS AND FEM SIMULATION

4.3.1 Static Behavior

Vertical motion of an electrostatic parallel plate actuator occurs when a driving voltage is applied between the top and bottom electrodes. The electrostatic force is given by

$$F = \frac{1}{2}\frac{dC}{dz}V^2 \tag{4.1}$$

where C is the capacitance between the electrodes, z is the vertical displacement along the actuation direction, and V is the applied DC bias voltage. For a parallel plate actuator, the capacitance varies with vertical displacement. Thus C can be expressed as

$$C = \frac{\varepsilon A}{(d-z)} \tag{4.2}$$

where ε is the dielectric constant in the air, A is the overlap area of top and bottom electrodes, and d is the gap between electrodes. By summarizing equation (4.1) and equation (4.2), electrostatic force can be rewritten as a function of applied voltage and shown in equation (4.3).

$$F = \frac{1}{2}\frac{dC}{dz}V^2 = \frac{1}{2}\varepsilon A\left(\frac{V}{d-z}\right)^2 \tag{4.3}$$

According to spring design of the proposed device, the micromirror is considered to follow Hooke's law. While assuming the micromorror is driven by an electrostatic force F along the

driving direction, the relationship between displacement and the reaction force F in the driving direction x can be expressed as

$$F = kx \tag{4.4}$$

where k represents the equivalent spring stiffness of the micromirror in the driving direction and x represents the displacement caused by the electrostatic force. In our case, the displacement x is equal to z, and the equivalent stiffness k is the summary of stiffness of two cantilever springs. Since equation (4.3) equals to equation (4.4) which yields equation (4.5) that specifies the relationship between moved displacement z and driving voltage V in the z direction.

$$V = (d - z)\sqrt{\frac{2zk}{\varepsilon A}} \tag{4.5}$$

In the present case, d is a constant value of 1 μm (distance between M3 and M4), A is square measure of net electrodes, k is spring constant of cantilever springs, and ε is the dielectric constant in the air. Based on equation (4.5), when the displacement is achieved 128 nm (λ/4), the relative driving voltage is about 2.6 V.

To understand the static behaviors of the device, a FEM simulator, IntelliSuite, is utilized to simulate micromirror deformation and displacement. Figure 4.2 displays the simulation result of the actual dimension micromirror model with a driving voltage of 3 V. Micromirror displacement is clearly of the same with the free end of the suspension beams. That is, deformation of the suspension beams induced by the electrostatic force can fully pass to the micromirror and lead to a vertical levitation of the micromirror. Figure 4.3 plots micromirror displacement versus driving

voltage. The simulation result demonstrates that the micromirror can achieve a 128 nm (λ/4) vertical displacement when applied voltage is about 2.7 V. Moreover, the pull-in voltage is about 4.5 V according to the simulation result.

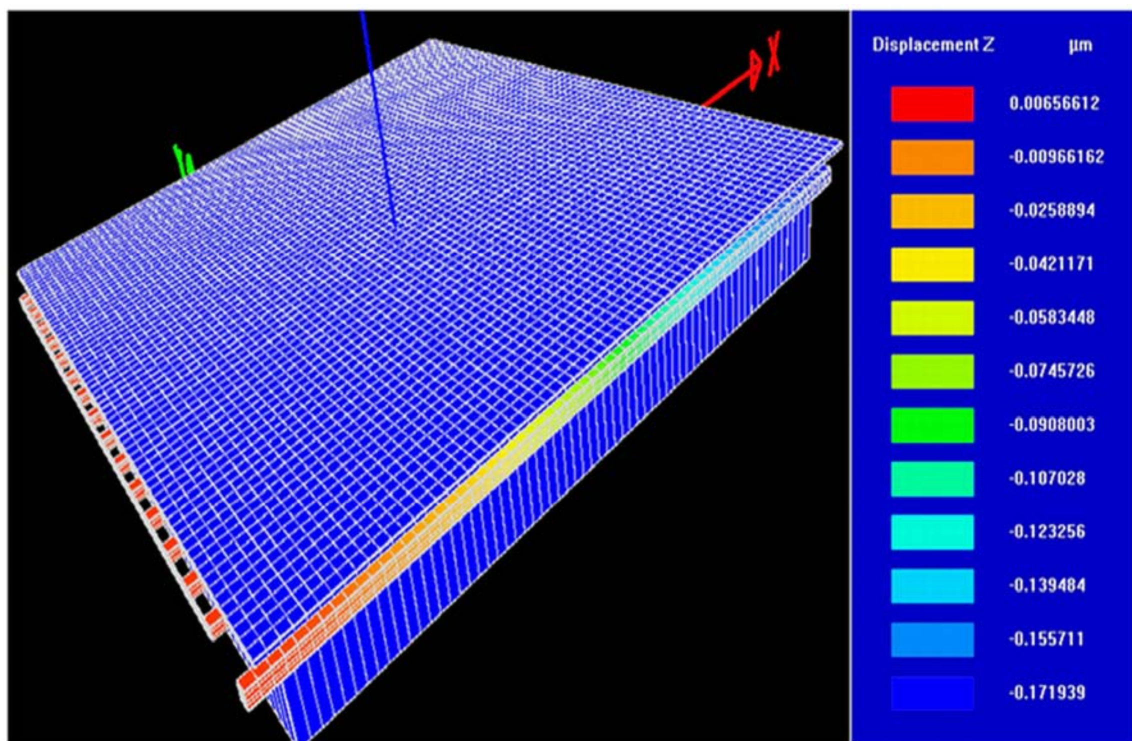

Figure 4.2 The deformation of the actual micromirror model with 3 V DC bias voltage.

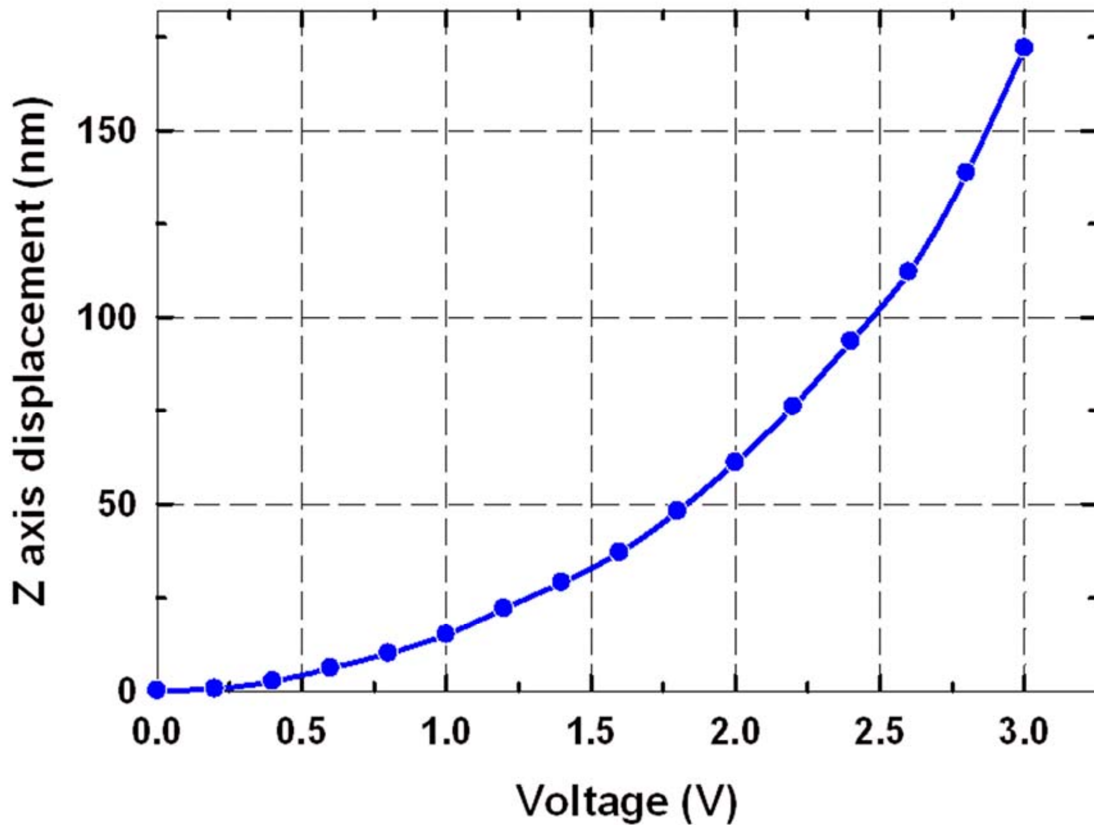

Figure 4.3 The simulation result of Z-axis displacement versus driving voltage.

1896

4.3.2 Resonant Frequency

A simplified theoretical model is utilized to calculate the resonant frequency of the proposed micromirror device. Deformation of the suspension beams which induced by an electrostatic force lead to a vertical levitation of the micromirror. Thus, the device model is similar to that of a clamped-clamped beam with a center mass, as illustrated in Figure 3.5. The fundamental resonant frequency of the equivalent model is also expressed as

$$f = \frac{4}{\pi}\sqrt{\frac{3\times\sum_{i=1}^{n} E_i I_i}{L_B^3 (M_B + 0.37 m_B)}} \tag{4.6}$$

where n is the number of layers in the suspension beam; E_i and I_i are the Young's modulus and the moment of inertia of each layer, respectively; L_B and m_B are the length and the mass of the equivalent clamped-clamped beam, respectively; and M_B is micromirror mass. The theoretical resonant frequency derived by equation (3.12) is 3.94 kHz. Moreover, resonant frequency is also simulated using IntelliSuite. Notably the FEM simulations only require suspension beams and micromirror to calculate the resonant frequency. The simulation result indicates that the fundamental resonant frequency is about 4.14 kHz and the mode shape is vertical motion. These results can be used as the reference data in actual experimental measurements.

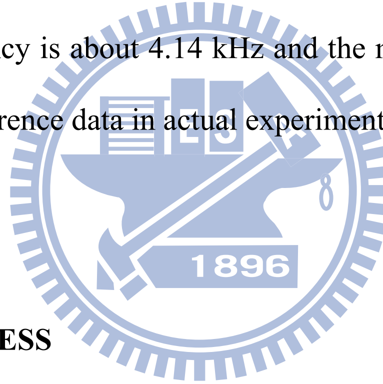

4.4 FABRICATION PROCESS

The designed phase shifter device was also manufactured using the TSMC 0.35 μm 2p4m CMOS process and a self-designed post-CMOS process. The CMOS process consists of two polysilicon layers, four metal layers, three via layers, and several dielectric layers. All metal layers are made of aluminum and the contact/via holes are filled with tungsten plugs. The dielectric layers are silicon dioxide and the passivation layer includes silicon dioxide and silicon nitride. The etched holes are filled with silicon dioxide. In order to fabricate a flat plane surface, chemical mechanical polishing (CMP) is employed after each deposition layer is completed.

A notable device releasing issue is that the passivation window of the MEMS structure must be

opened in advance of the post-process. The self-designed post-CMOS process is applied to reserve a bulk silicon mass for reducing micromirror deformation and release the suspended structures. The post-process includes one grinding process, one backside alignment lithography process, a 2-step backside inductively coupled plasma (ICP) etching process, and an HF vapor releasing process. Figure 4.4 illustrates the post-process flow. The post-process is implemented using the following steps:

(a) The post-process starts with the device fabricated after the CMOS foundry process with the passivation window already open as shown in Figure 4.4(a). The open-window step is implemented during the foundry process.

(b) A backside grinding process is utilized to grind down the silicon substrate thickness, reserving only 100 μm for economic considerations to save expense and time for the ICP etching process, as shown in Figure 4.4(b).

(c) After that, a backside lithography process is applied to define the proof mass area, and then PI tape is used to protect the peripheral area of the chip from ICP etching, as illustrated in Figure 4.4(c).

(d) Then the first anisotropic ICP etching step is conducted to etch the silicon substrate for proof mass reservation, in which PR and PI tape are used as the hard mask, as illustrated in Figure 4.4(d).

(e) Figure 4.4(e) depicts the second step of the ICP etching process. In this step, PR is removed

by PR stripper but the PI tape is reserved for the second mask instead of PR. Although the ICP process etches the PI tape, the tape extends the etching time to form the proof mass. In this etching step, silicon dioxide is utilized as the etching stop layer since the etching selectivity of silicon dioxide is significantly higher than that of PI tape.

(f) To prevent the micromirror from sticking problem during wet etching release process, as shown in Figure 4.4(f), an HF vapor etching process is used to release the micromirror structure in the final step. The dry etching process is performed by heating 49 % HF liquid to produce HF vapor which is utilized to etch SiO_2. Since the device was fabricated by CMOS process, the compositions of the four metal layers are not pure Al, but the alloy of Al, Cu, and Si. The etching selectivity between SiO_2 and Al is very large that we can use HF vapor process to release our device. At first, the device chip is placed in a sealed limpid space. In the space there is a vessel with 49 % HF liquid. A tungsten lamp is placed upon the sealed limpid space with 10 cm height. When the HF liquid is heated to 45 ℃ by tungsten lamp irradiation, the sealed space is full of HF vapor. Finally, the silicon dioxide is etched by HF vapor and device structures are released. The experimental release time in this case is about 12 minutes.

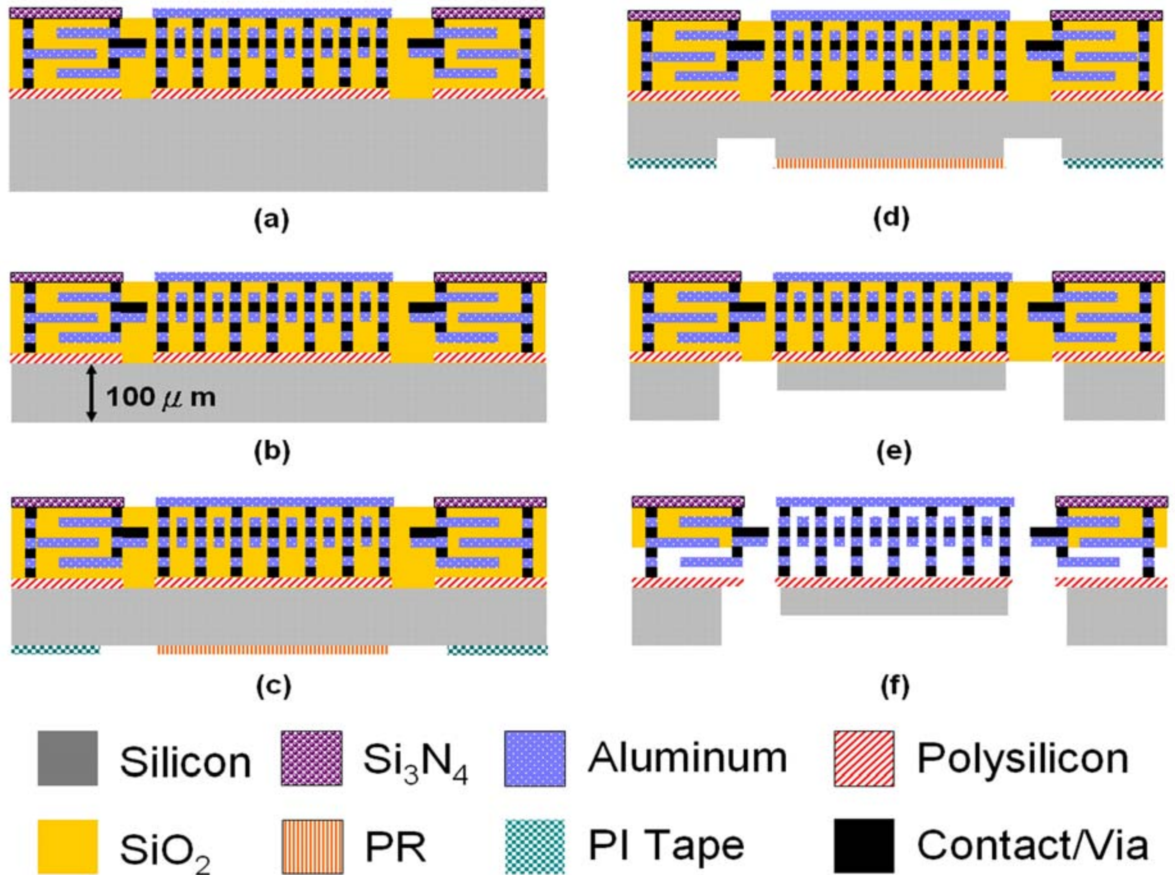

1896

Figure 4.4. Post-CMOS fabrication process flow: (a) completion of the CMOS process, (b) reserving only 100μm of silicon by grinding process, (c) defining proof mass area by backside lithography process, (d) first backside ICP etching step, (e) second backside ICP etching step, (f) HF vapor etching process to release suspended microstructures.

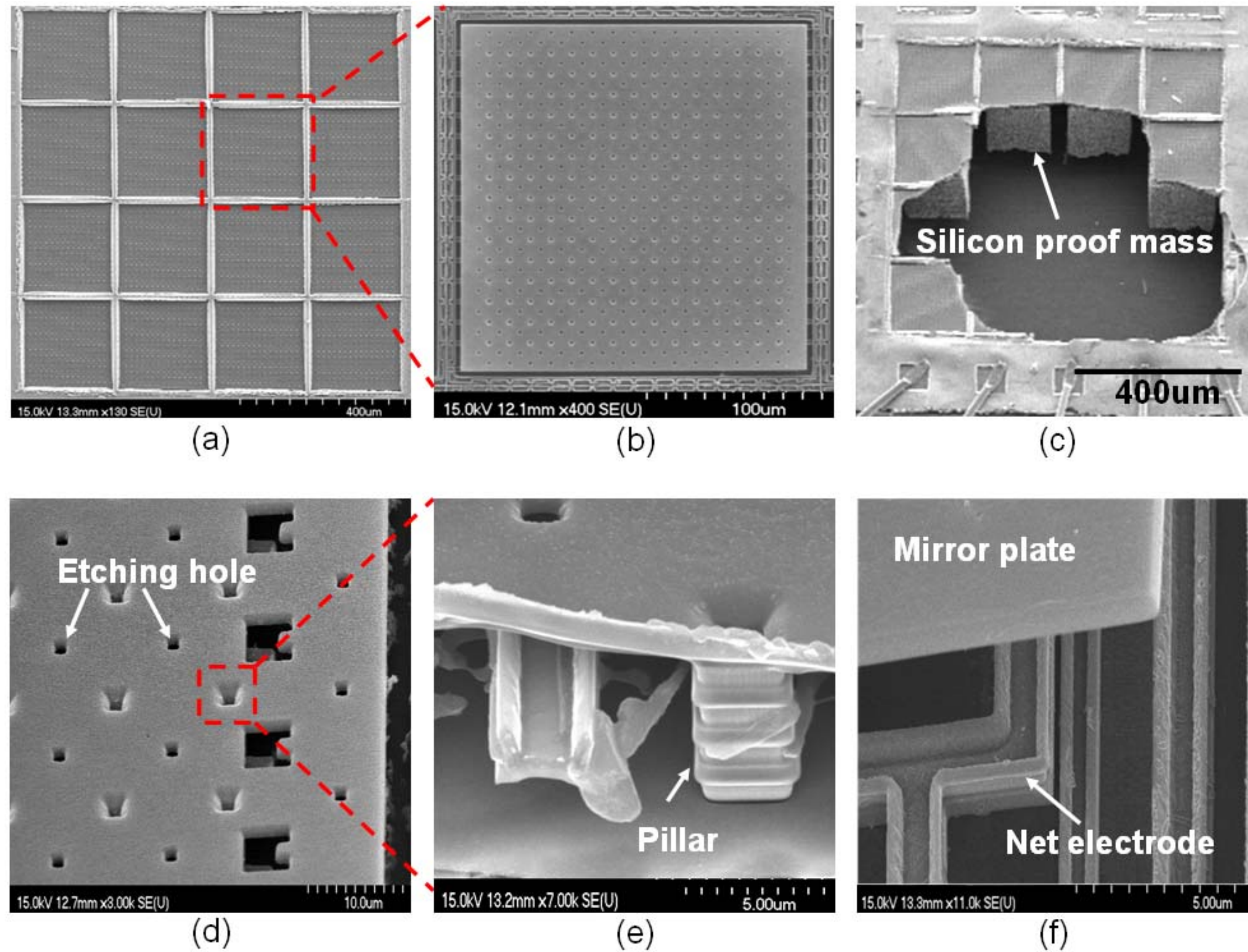

Figure 4.5 SEM pictures of the proposed micromirror phase shifter: (a) 4×4 mirror array, (b) an individual mirror pixel, (c) the silicon proof mass under the mirror plate, (d) the etching holes and hollows on the mirror, (e) the pillar structure, (f) the net electrode under the mirror plate.

Figure 4.5 displays SEM images of the device fabricated using the CMOS process and post-CMOS processes. Figure 4.5(a) shows the 4×4 mirror array combined phase shifter device and an individual pixel is shown in Figure 4.5(b). The proof mass design is clearly displayed in Figure 4.5(c) and it can effectively reduce the residual stress from the CMOS surface process. The etching holes, pillars and net electrode of the micromirror are shown in Figure 4.5(d) to 4.5(f), respectively. The hollows in Figure 4.5(d) are due to violations of the CMOS design rule.

4.5 EXPERMENTAL RESULTS

4.5.1 Flatness of the micromirror

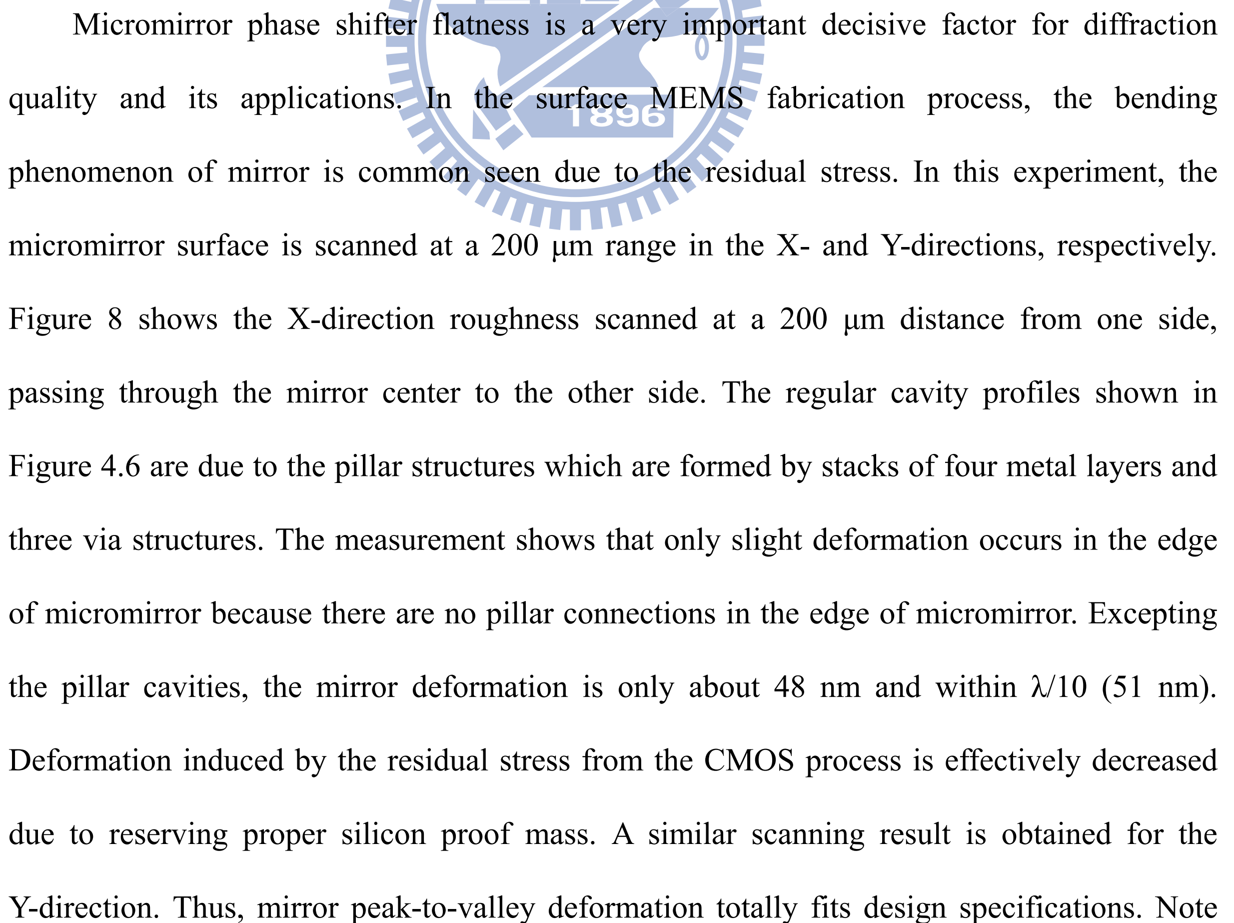

Micromirror phase shifter flatness is a very important decisive factor for diffraction quality and its applications. In the surface MEMS fabrication process, the bending phenomenon of mirror is common seen due to the residual stress. In this experiment, the micromirror surface is scanned at a 200 μm range in the X- and Y-directions, respectively. Figure 8 shows the X-direction roughness scanned at a 200 μm distance from one side, passing through the mirror center to the other side. The regular cavity profiles shown in Figure 4.6 are due to the pillar structures which are formed by stacks of four metal layers and three via structures. The measurement shows that only slight deformation occurs in the edge of micromirror because there are no pillar connections in the edge of micromirror. Excepting the pillar cavities, the mirror deformation is only about 48 nm and within $\lambda/10$ (51 nm). Deformation induced by the residual stress from the CMOS process is effectively decreased due to reserving proper silicon proof mass. A similar scanning result is obtained for the Y-direction. Thus, mirror peak-to-valley deformation totally fits design specifications. Note

that after completed the released process, each mirror pixel is positioned at different elevation due to the different stiffness of the suspension beams. Considering with whole flatness of the micromirror array, each micromirror is designed to be driven by individual driving voltage so that we can balance each mirror elevation to achieve flatness purpose by individual offset voltage.

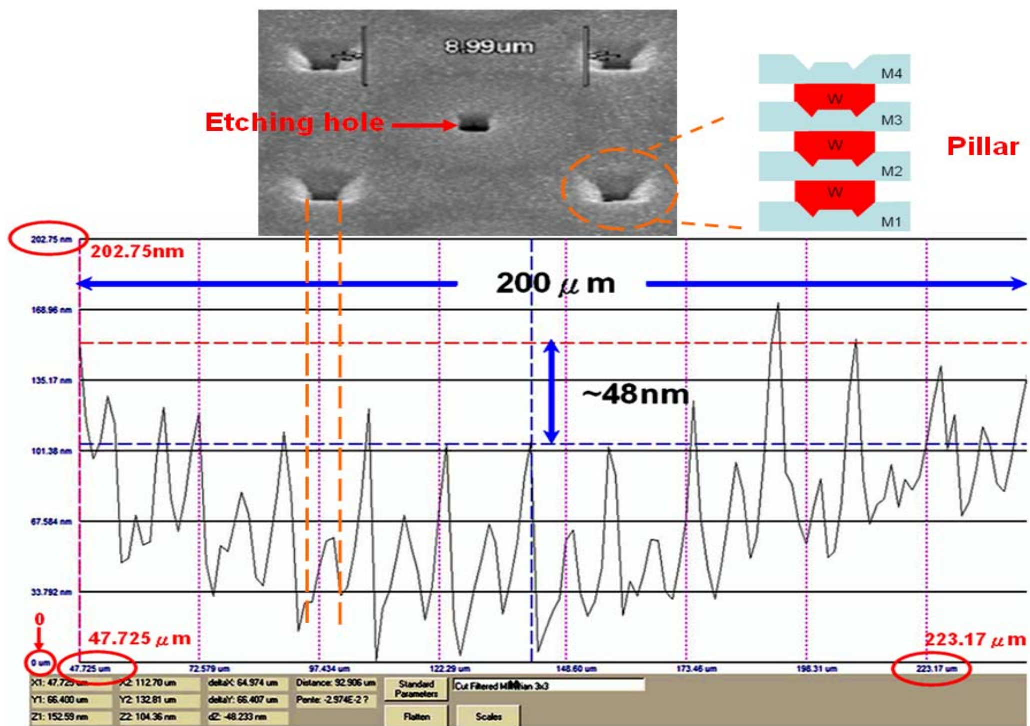

Figure 4.6. X-direction surface flatness of the micromirror device

4.5.2 Static characteristic measurement

The experiment setup for static characteristic measurements is the same as Figure 4.7. In this experiment, the WYKO interferometer is used again to measure the vertical distance moved by corresponding driving voltage. A DC bias voltage provided by the power amplifier is utilized to actuate the micromirror. Figure 4.7 compares simulation and measurement results of a single mirror for vertical displacement versus driving voltage. The experimental results demonstrate that vertical motion of the micromirror can achieve a 128 nm displacement (λ/4 of the 514 nm light source) when a 3 V driving voltage is applied to the actuator. The vertical displacement of the micromirror of 0~128 nm is obtained by increasing the driving voltage from 0 to 3V. Thus, the requirement of λ/4 displacement can be easily reached with less than 5 V driving voltage. The low driving voltage characteristic gives the device potential to integrate with a CMOS circuit on one chip.

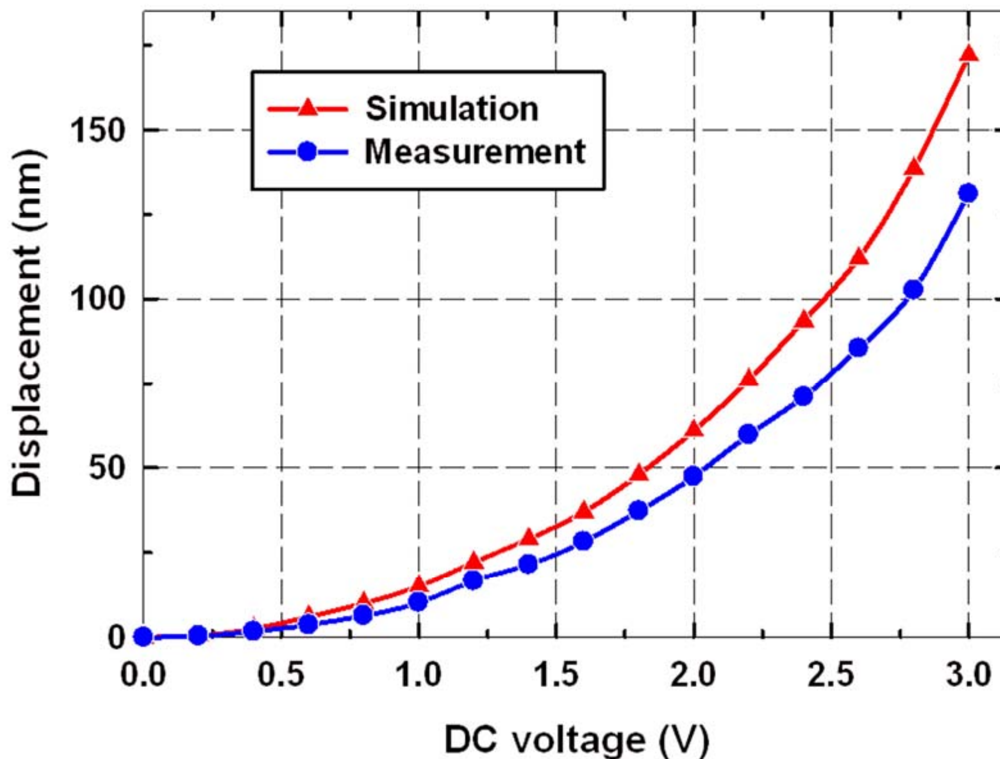

Figure 4.7. The static characteristic of the micromirror.

4.5.3 Frequency response measurement

Figure 4.8 shows the frequency response of the micromirror device measured using a MEMS Motion Analyzer (MMA). The micromirror is biased by a sinusoidal wave with voltage amplitude of 0.5 V, and the frequency ranges between 1.5 and 5.5 kHz. The first resonant frequency mode is measured at 3.60 kHz, which closely matches the calculation (3.94 kHz) and simulation (4.14 kHz) results. The error is due to variations in the CMOS fabrication process and post-process. The quality factor of the mirrors is calculated at 24 in air.

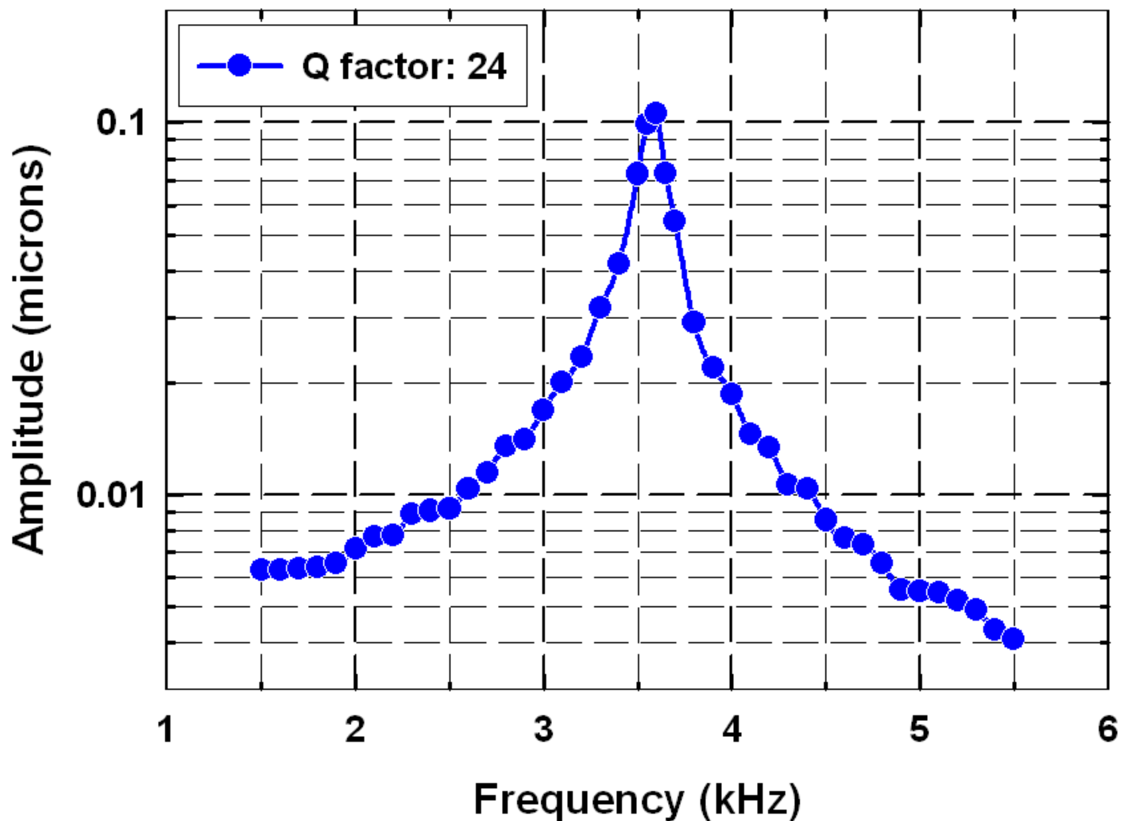

Figure 4.8. The frequency response of the micromirror.

4.6 SUMMARY

This study presents a 4×4 electrostatic phase shifter micromirror array fabricated by TSMC 0.35 μm 2p4m CMOS process and the self-designed post-CMOS process. By means of the special net electrode design under the mirror, the micromirror array has a fill factor of more than 90%. Individual mirror pixels are 200 μm× 200 μm. Mirror deformation resulting from residual stress of the CMOS process is effectively decreased via a proof mass reservation design. To prevent the device from the side sticking phenomenon in a wet etching release process, this device is released by HF vapor etching technique. The design, modeling, simulation and measurements are presented. Preliminary measurement results demonstrate that the micromirror can achieve a 128 nm (λ/4) vertical displacement with a driving voltage of 3 V and the resonant frequency is 3.6 kHz. With the advantages of a high fill factor and low driving voltage, the phase-shifting micromirror array has potential as a spatial light modulator (SLM) in holographic data storage systems in the future.

4.7 CONCLUSION REMARK

In this chapter, MEMS based phase shifter are designed, fabricated, and measured. By the design of high aspect ratio proof mass reserved under the micromirror fabricated by surface micromachining, warped phenomenon caused by residual stress can be effectively eliminated. Furthermore, by utilizing the HF dry etching process, we can design micromirror array with high fill factor and low driving voltage without additional flip-chip bonding technology. Besides, it is very easy to integrate MEMS devices and circuits by utilizing the CMOS MEMS foundry process and easy post process.

CHAPTER V

DECOUPLING XY STAGE APPLICED IN CELLPHONE CAMERA IMAGE STABILIZER

5.1 INTRODUCTION

In this chapter, we introduce the high aspect ratio structure in MEMS device integration. Due to the characteristic of high structure stiffness, high aspect ratio structure is with the capability of large output and high device loading. Therefore, it offers the probability that integrate the MEMS devices and the other sensing devices by flip chip bonding. We demonstrate those characteristics by designing, fabricating, and measuring of MEMS based image stabilizer.

5.1.1 Introduction of MEMS image stabilizer

As the photographic cell phone in all instances is gaining popularity all over the world, new digital single lens reflex (DSLR) photography functions for mobile phones are being developed. Anti-shake technology is one of the most important new technologies. Since the number of pixels in a camera has been continuously increasing, undesirable image blurring, caused by hand shake is becoming increasingly serious. The image stabilization function is one of the most popular solutions to this problem [85]. The familiar elements of image stabilization are lens shifting [86], CCD shifting [87], and signal processing [88] among others. Up to now, the most common anti shaking technique used in mobile phones has been signal processing. It requires no additional hardware and does not disrupt the miniaturization of the system module. However, its performance depends strongly on the algorithm used.

Because of the need for miniaturization, the lens shifting anti-shaking approach is not suitable, since adding a movable lens causes nonlinearity in control that needs to be compensated for using a complex control algorithm. Image sensor shifting also requires an actuating system associated with the image sensor, but is less disrupting of miniaturization and enable better slimming of the system than the lens shifting method [85]. In this investigation, a MEMS-based two dimensional (2D) decoupling actuator is designed to act as an image stabilizer.

Micro-electro-mechanical systems (MEMS) enable suspended microstructures to be precisely moved and integrated with microelectronic circuits monolithically on a chip [89]. Various actuation mechanisms, such as thermal/bimetallic bimorph[90-91], electromagnetic [92] piezoelectric [93,94] and electrostatic actuations[95,96] have been proposed and adopted in MEMS-based devices in which mechanical actuation is required[97]. To summarize all of the driving functions applied in MEMS-based devices, the electrostatic actuator has numerous advantages, such as low power consumption, ease of control, and suitability for use as an image stabilizer designed for a cell phone.

In this investigation, we propose a two-dimensional decoupling comb-driving actuator, which is manufactured by a special SOG process. This actuator is designed as an image stabilizer that bears the weight of a $6.36 \times 6.24\ mm^2$ image sensor with 3 megapixels.

5.2 DESIGN CONCEPT OF MEMS IMAGE STABILIZER

5.2.1 Principles of operation of electrostatic comb-drive actuator

The XY stage designed herein is driven by an electrostatic force [98]. Figure 5.1 shows a simple schematic diagram of the comb-driven model. When a potential difference is applied between fixed and movable comb fingers, an electrostatic force is generated, causing the relative displacement of the movable comb fingers (Figure 5.1). The driving force *F*; can be expressed as

$$F = \frac{\partial U}{\partial L} = \frac{1}{2}\frac{\partial C}{\partial L}V^2 = \frac{Nt\varepsilon_o\varepsilon_r V^2}{d}, \tag{5.1}$$

where *U* is the energy associated with the applied electric potential *V*, *d* is the gap between the fixed and movable comb fingers, t is the thickness of the electrodes, *N* is the number of pairs of comb fingers, ε_r is the relative permittivity of the dielectric material between the comb fingers, and ε_o is the permittivity in air. For simplicity, the XY stage is considered to follow Hooke's law. The relationship between displacement and the reaction force F_s in the x-direction can be expressed as,

$$Fs = k_{x-system}x, \tag{5.2}$$

where $k_{x\text{-}system}$ is the equivalent spring stiffness of the system in the X direction and *x* is the displacement caused by the electrostatic force. Equation (5.3) is the sum of equation (5.1) and (5.2) and specifies the relationship between the displacement *x* and the driving voltage *V*:

$$x = \frac{1}{2}\frac{Nt\varepsilon_o\varepsilon_r V^2}{dk_{x-system}} \quad . \tag{5.3}$$

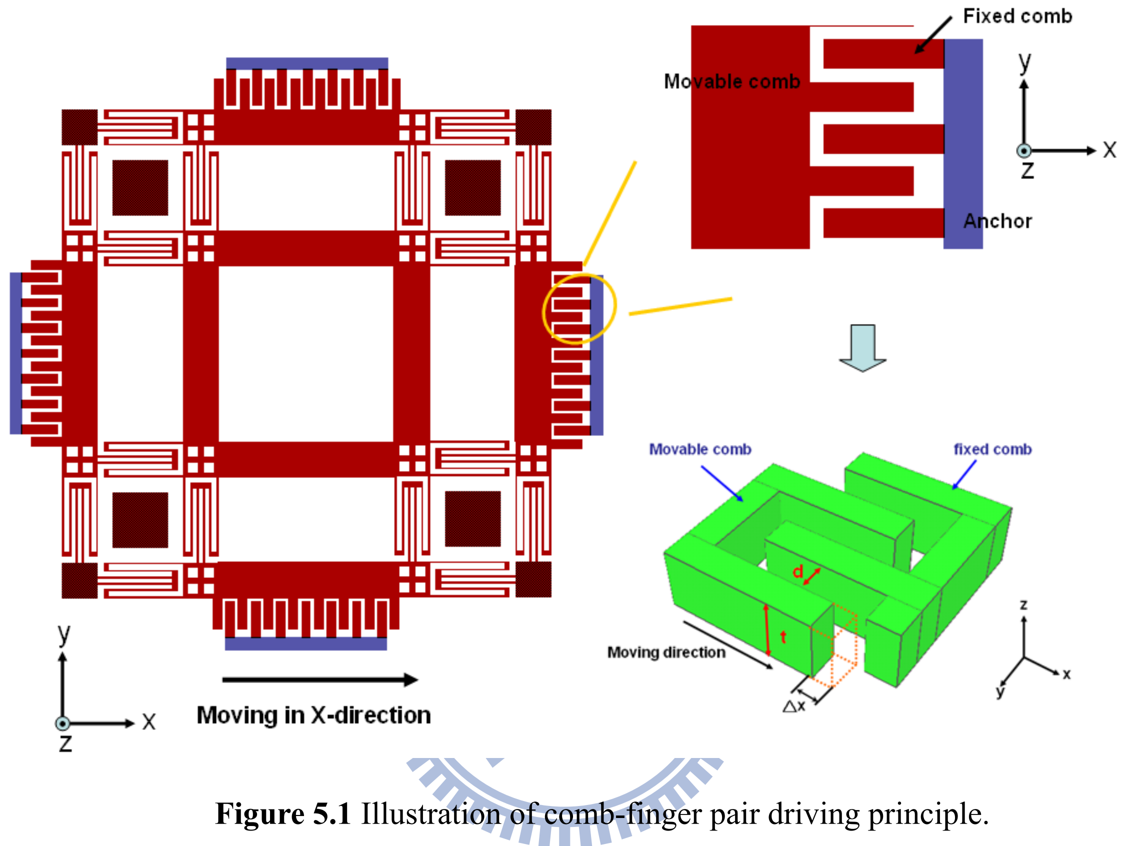

Figure 5.1 Illustration of comb-finger pair driving principle.

5.2.2 Design of decoupling structure

Figure 5.2 schematically depicts the decoupling XY stage. It includes the decoupling and driving parts of the device. The main decoupling structure is similar to the SYMDC micro gyroscope structure [99]. Given the instability caused by the lateral force, perfect mechanical isolation between the two orthogonal driving directions is important. To achieve this purpose, fixed and movable folded-beam springs are installed in each direction of the XY stage. The driving pair is attached around the decoupling part. Comb-driver finger pairs are chosen as the

driving sources to ensure low power consumption and ease of control.

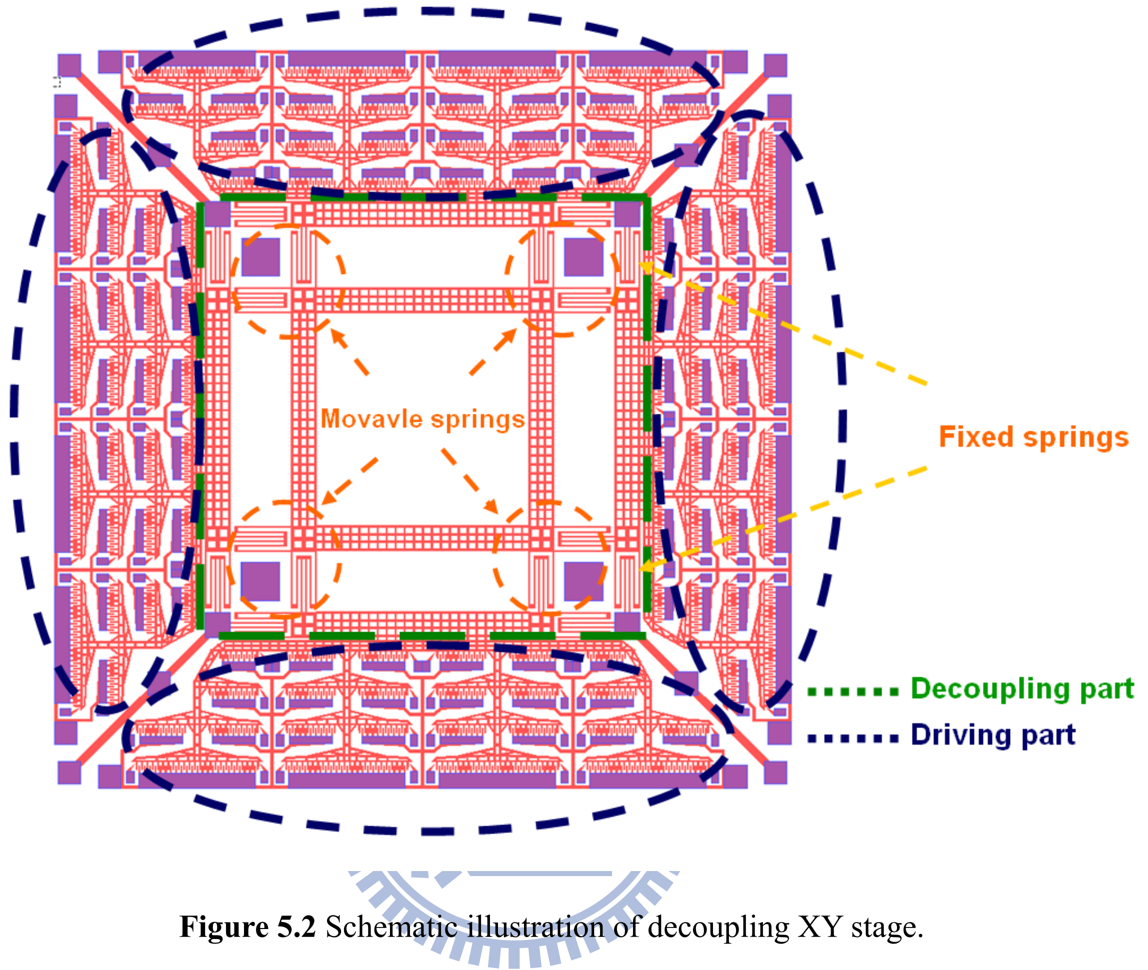

Figure 5.2 Schematic illustration of decoupling XY stage.

When a force is applied in the X-direction only, the XY stage motion and spring flexible situation are as shown in Figure 5.3(a). Figure 5.3(b) shows a simplified mechanism of the operation of the proposed decoupling XY stage when different forces are applied in the X- and Y-directions. On the basic of the assumption that the stiffness of the fixed folded-beam spring is k_{fixed} and the stiffness of the movable folded-beam spring is $k_{movable}$, the stiffness of the system in the X-direction, $k_{x\text{-}system}$, and that in the Y-direction, $k_{y\text{-}system}$, can be represented respectively; as

$$k_{x-system} = 2k_{x-fixed} + 2k_{x-movable} \;;$$
$$k_{y-system} = 2k_{y-fixed} + 2k_{y-movable} \;. \tag{5.4}$$

In this case, the sizes of the folded beam spring and movable beam springs are equal; thus the stiffness components; $k_{x\text{-}system}$ and $k_{y\text{-}system}$; can be expressed as;

$$k_{x-system} = 4k_{x-fixed} \;;$$
$$k_{y-system} = 4k_{y-fixed} \;. \tag{5.5}$$

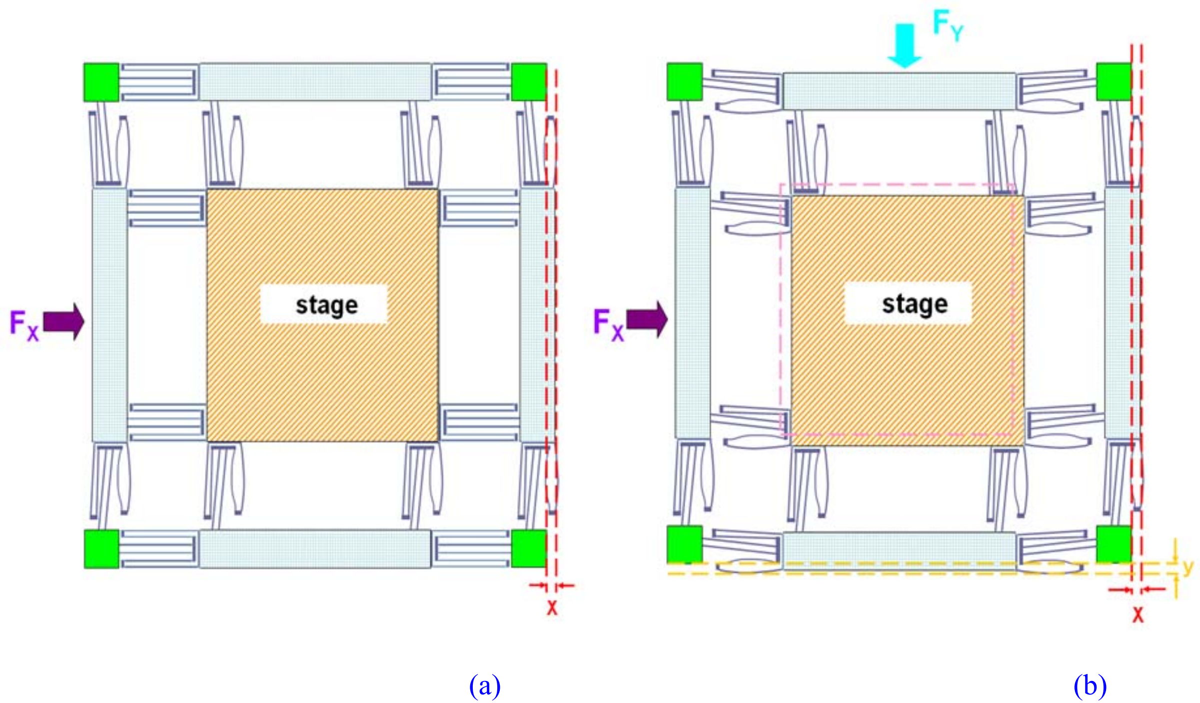

Figure 5.3 Illustration of driving modes of decoupling XY stage: (a) in only X-direction, and (b) in both X- and Y-directions.

Figure 5.4 shows the spring design of the structure, based on the energy method [100]. E is Young's modulus, I_a and I_b are the moments of inertia of the different beams, and L_a and L_b are the lengths of the different beams. When the driven force is parallel to the x-direction, the stiffness of a single folded-flexure spring under elastic deformation in the x-direction and the

coupled stiffness in the y-direction are calculated as;

$$K_{xx} = \frac{48EI_aI_b(3I_bL_{a1} + I_aL_b)}{K_d}, \tag{5.6}$$

$$K_{xy} = \frac{18EI_aI_b\left[2I_bL_{a1}\left(L_{a1} - L_{a2}\right) - I_aL_bL_{a2}\right]}{L_bK_d}, \tag{5.7}$$

Where;

$$K_d = 3I_a^2L_b^2L_{a2}^2 + 6I_b^2L_{a1}\left(2L_{a1}^3 + L_{a2}^3\right) + 2I_aI_bL_b\left(8L_{a1}^3 + 6L_{a1}^2L_{a2} + 6L_{a1}L_{a2}^2 + L_{a2}^3\right).$$

In this case, the stiffnesses of all decoupling structures in the x- and y-directions are given by

$$k_{x-system} = 4k_{x-fixed} = 4(2K_{xx}) = 8K_{xx} = \frac{384EI_aI_b(3I_bL_{a1} + I_aL_b)}{K_d}, \tag{5.8}$$

$$k_{y-system} = 4k_{y-fixed} = 4(2K_{xy}) = 8K_{xy} = \frac{48EI_aI_b\left[6I_aL_bL_{a2}^{\ 2} + I_b\left(8L_{a1}^{\ 3} - 12L_{a1}^{\ 2}L_{a2} + 6L_{a1}L_{a2}^{\ 2} + L_{a2}^{\ 3}\right)\right]}{L_b^{\ 2}K_d} \tag{5.9}$$

Where;

$$K_d = 3I_a^2L_b^2L_{a2}^2 + 6I_b^2L_{a1}\left(2L_{a1}^3 + L_{a2}^3\right) + 2I_aI_bL_b\left(8L_{a1}^3 + 6L_{a1}^2L_{a2} + 6L_{a1}L_{a2}^2 + L_{a2}^3\right).$$

Therefore, when a single direction force is driven parallel to the x-direction, the decoupling ratio of x displacement to y displacement in the spring system is defined as

$$\left|\frac{x}{y}\right| = \left|\frac{K_{y-system}}{K_{x-system}}\right| = \frac{3\left[2I_bL_{a1}\left(L_{a1} - L_{a2}\right) - I_aL_bL_{a2}\right]}{4L_b\left(3I_bL_{a1} + I_aL_b\right)}. \tag{5.10}$$

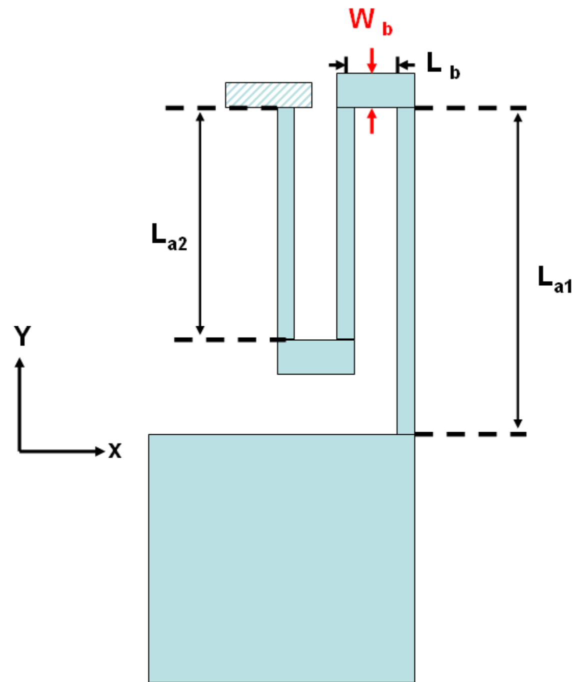

Figure 5. 4. Illustration of folded-flexure spring.

Based on the formula calculations, the decoupling ratio of mechanical stiffness must conform to the system requirement of being larger than 11.1. Table 5.1. shows the design specifications of the decoupling XY stage and the image sensor size.

Table 5.1 Specifications of the image stabilizer

Specification	value
Device size(mm^2)	8 × 8
Image sensor size(mm^2)	6.36 × 6.64
Structure layer thickness(μm)	150
Gap between pair of fingers(μm)	15
Number of comb finger pair	1020
Width of the floded spring(μm)	15
Length of the floded spring L_{a1}(μm)	710
Length of the floded spring L_b(μm)	40
Length of the floded spring L_{a2}(μm)	610
Depth of pre-etching layer(μm)	50

5.2.3 Design and calculation of range of motion of decoupling XY stage

Most commercial cell phones have a camera with 2 or 3 megapixels but no anti-shaking function. People are always moving and are unable to take a picture without moving at all. Any vibration during taking picture causes blurring. Figure 5.5 shows the relationship between the number of blurring pixel and the angle of hand shaking. When the camera moves through an angle $d\theta$ in the horizontal plane, the blur pixel number can be represented as;

$$BP = \frac{d\theta}{\theta_L} P_H \tag{5.11}$$

Where θ_L is the horizontal angle, and P_H denotes the total numbers of horizontal blur pixel. Typical low-cost camera systems have an angular field of view within 35º to 45º. For a 3 megapixel image sensor with a field of view of 45º, experimental data [101] indicate that a 0.08º horizontal drift occurs in 2 second recording time of hand shaking, as recorded by an IDG-1000, a dual-axis gyroscope from InvenSense [108].

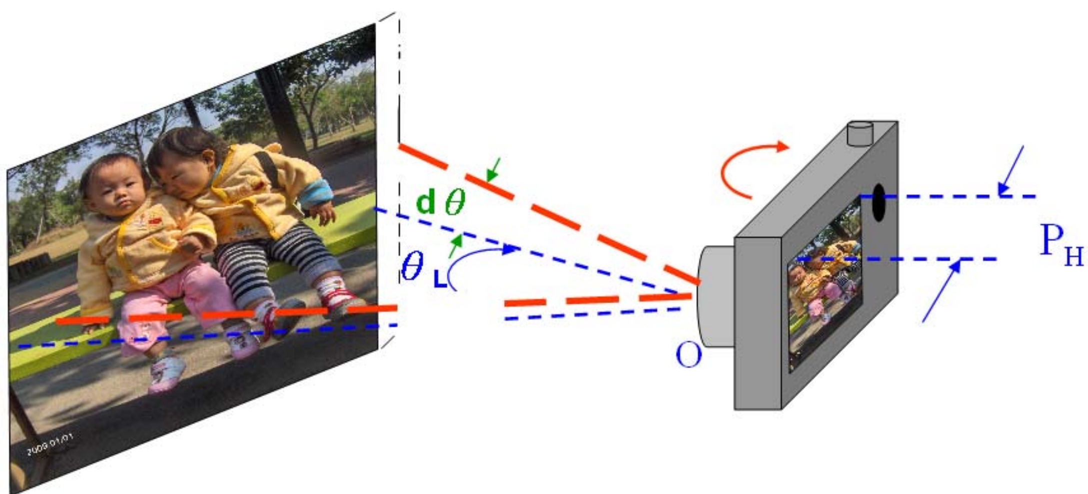

Figure 5.5 Illustration of relationship between number of blur pixels and hand shake angle.

In this study, an image sensor Micron MT9T012 with 3 megapixels (2056 ×1544 pixels) is employed as the image sensor that is bonded to the designed device. From equation (5.11), each pixel corresponds to a horizontal angle of 0.022º. Therefore, the number of horizontal blur pixels is approximately 3.7. Since each pixel of MT9T012 is 2.2 × 2.2 μm^2, the XY stage must have a range of motion of at least 8.14 μm for adjustment of the blur image. Given that many commercial cameras have × 3 zoom-in and zoom-out functions, the range of motion must be three times this value; or 24.42 μm. In order to achieve the anti-shaking purpose, the moving range in the vertical direction of driven force must be less than 2.2 μm (1 pixel size). This means that the decoupling ratio of x- displacement to y-displacement should be designed to be larger than 11.1.

5.3 FEA MODELING STRUCTURE

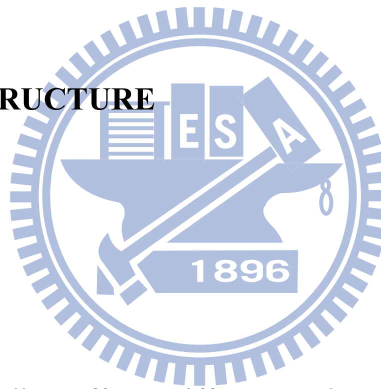

ESA
1896

5.3.1 Static simulation

To elucidate the decoupling effect, stiffness, and natural frequency of the designed XY stage, the proposed decoupling actuator is developed using IntelliSuite 8.2. This software is utilized to simulate displacements in plane and the coupled mechanical interference of the XY-stage in each orthogonal direction. The actual boundary conditions are as follows. 1. The anchors and stators are not displaced because these are in contact with the substrate. 2. The shuttle, rotors, and flexure beams are suspended above the substrate, making the parts free. For simplicity, the shapes of the spring and anchor structures are kept and the other structures are calculated of the mass, being equal to the cube of the same weight as the real device: When simple moldings of the designed moving spring and a frame-loaded spring as the same size as the image stabilizer are fabricated, distinct decoupling occurs, as presented in Figure

5.6(a) and 5.6(b) respectively. In this simulation, a 0.02 MPa pressure in the X-direction results in a 1.33 μm displacement in that direction, but only a 0.01 μm displacement in the Y-direction. The simulation decoupling ratio of x-displacement to y-displacement is 133 and shows excellent decoupling effect in the design of movable springs.

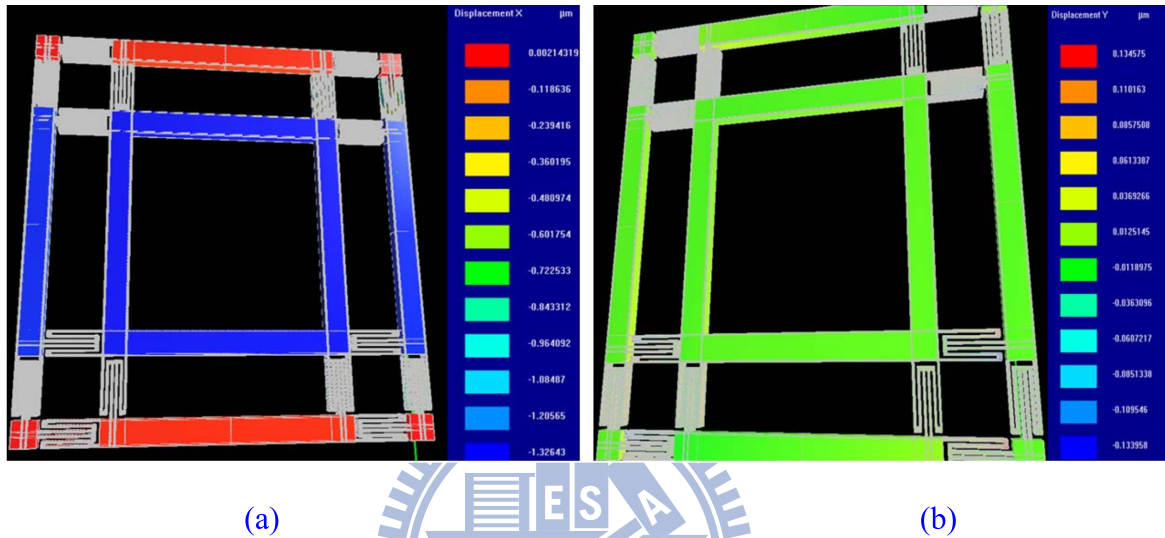

Figure 5.6 Decoupling simulation of the XY stage in: (a) X-direction, and (b) Y-direction when driving force in X-direction only.

To estimate the above stiffness of this designed structure, a simple simulation is performed: a force in a single direction is applied to one side of the XY stage. The resulting displacement of the XY stage in the static simulation demonstrates that when the force is 1000 μN in both the X- and the Y-directions, the displacement in the x-direction is 4.86 μm and the simulated system stiffness of simulation in the X- direction is 205.42 μN/μm, as calculated by using Equation (5.2).

5.3.2 Dynamic simulation

To verify the vibration characteristics when the XY stage is under dynamic loading, an instantaneous analysis using the FEM software; Intellisuite 8.2; is performed to determine the resonant frequency and modal shape of the designed structure. In this simulation, the weights of the XY stage and image sensor are calculated and found to be equivalent to a proof mass shown in Figure 5. 7. The simulated resonant frequency of the first mode is 1280.1 Hz, that of the second mode is 1280.2 Hz, and that of the third mode is 1353.52 Hz. Since the stabilizer is a symmetrical device, the resonant frequencies of the first and second modes are almost the same but they operate in the X- and Y- directions, respectively. The third mode involves rotation in the XY plane, and its resonant frequency is given by

$$F_{resonant} = \frac{1}{2\pi}\sqrt{\frac{k}{M}}, \qquad (5.12)$$

where $F_{resonant}$ is the resonant frequency, stiffness of the device structure in X direction and Y direction k = 205.42 μN/μm, obtained by simulation, and M is the mass of the XY stage. These parameters yield a calculated $F_{resonant}$ of 1.248 kHz.

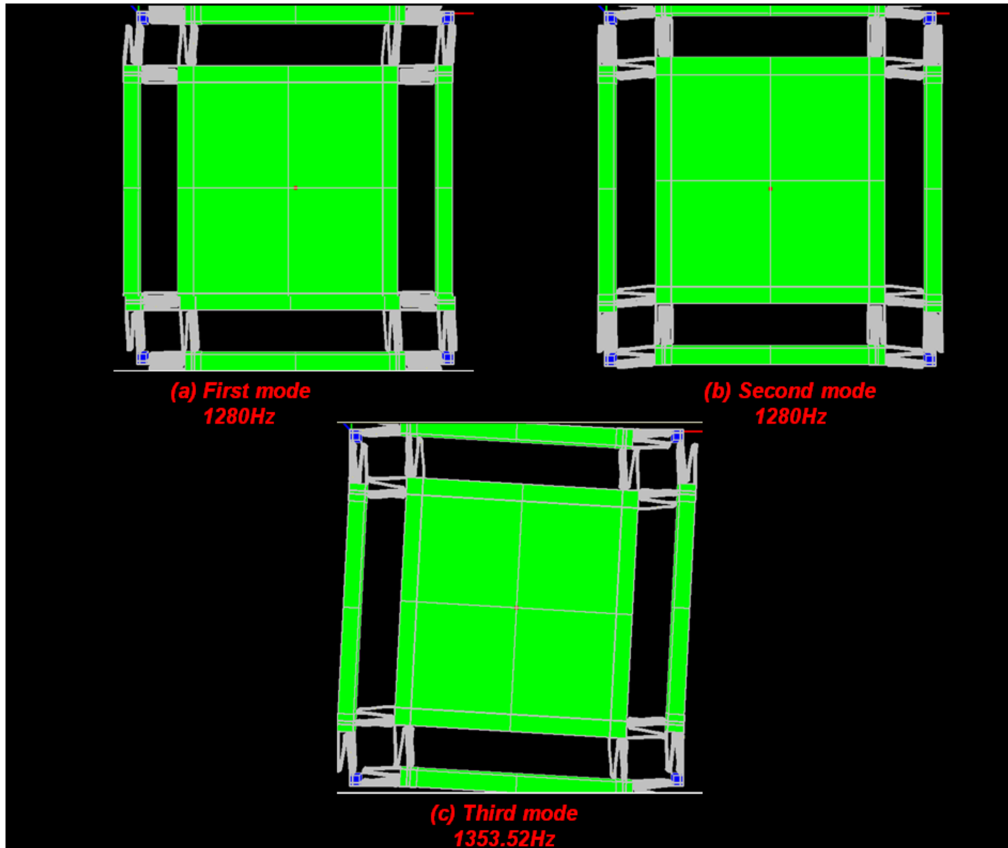

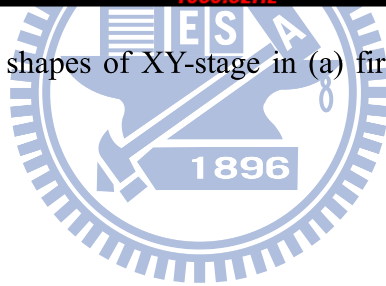

Figure 5.7 Dynamic model shapes of XY-stage in (a) first mode, (b) second mode, and (c) third mode.

5.4 FABRICATION PROCESS

5.4.1 Fabrication of image stabilizer

The decoupling XY actuator has an area of 8 × 8 mm^2, exploits anodic bonding, and is produced by double-side alignment photography and ICP etching. Figure 5.8 shows the fabrication process, which begins with a 200 μm-thick 100 silicon wafer. In basic RCA cleaning, a thin 8000 Å-thick layer of Al is deposited by DC sputtering [Figure 5. 8(a)] as the first hard mask for the anchor structure during the second ICP etching process [Figure 5.8(b)]. Then, the pre-etching layer (for the uniformity of etching rate of ICP process

consideration) is patterned using the photoresister AZ4620 as the second hard mask in the second lithographic process [Figure 5.8(b)]. Notably, the pre-etching layer (in the second lithographic process) is required to balance the Si etching rate in the ICP process. Because the etching rate over a large area exceeds that over a smaller area, that at the edges of the Si wafer exceeds that in its center. The design of the pre-etching layer can ensure etching uniformity and prevent the notching effect from happening. The photoresist AZ4620 was removed [Figure 5. 8(c)] after the first ICP etching process to define the pre-etching area with a depth of 50 μm [Figure 5.8(d)]. The second ICP process used Al as the hard mask to form the anchor structure with a depth of 100 μm [Figure 5.8(e) – 8(f)]. After these processes had been completed and Al had been removed, RCA cleaning was necessary because the Si and glass surface must be very clean. Anodic bonding was then employed to combine the Si wafer with pyrex ＃7740 glass [Figure 5.8(g)]. An 8000 Å –thick layer of Al was deposited on Si as the conductive layer and a hard mask was used to define the device structures in the third lithographic process [Figure 5.8(h)]. A double-sided aligner was used to define layer of the structure before Al was etched and the photoresister was restricted. Then, a 1um-thick layer of SiO_2 was deposited as the isolation layer by plasma enhance chemical vapor deposition (PECVD) [Figure 5.8(i)]. The fourth lithographic process was used to pattern the same mask as that the third lithographic process to cover the Al layer completely and prevent shorting between the structure layer and the ball-bond layer that is designed to bond image sensor. Finally, a third Al deposition process and the fifth photolithographic process are applied to define the ball-bond area of the image sensor. Finally, a third ICP etching process is utilized to etch Si to a depth of 150 μm until the structure is released [Figure 5.8(j)]. Notably, the ICP etching parameters had to be controlled very strictly to ensure that all of the device structures were released simultaneously.

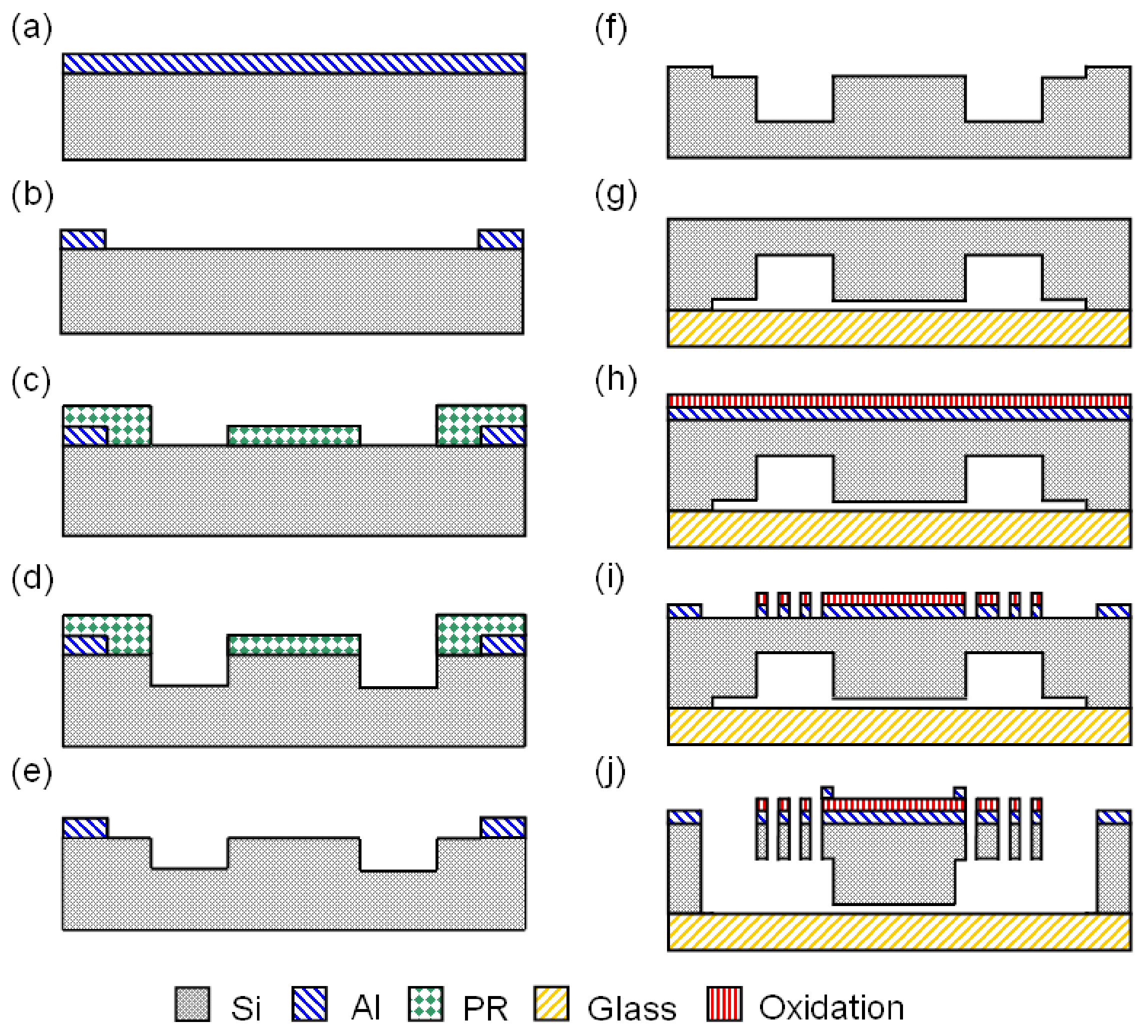

Figure 5.8 Fabrication process flow of image stabilizer:

5.4.1 ICP Etching uniformity

In general, there exists the problem of less etching uniformity in plasma etching system because of the unbalanced ion and neutral transport [102]. The design of gas transport and the location of the coil in the etching chamber strongly affect the uniformity of the etching speed. In real experiments, the etching rate close to the fringe of a wafer always exceeds that (close to the center of a wafer. As well as the design of the equipment, the mask design seriously influences the etching uniformity. This problem of gas transport makes the etching rate in the: small etching window area is much lower than in the large etching window area. Figure 5.9

presents a way of testing the etching rates in different etching areas. Clearly, the etching rate varies with the etching window. This problem arose in the experiment herein. Figure 5.10 shows that when the large area has been completely etched, the small etching areas still retain Si residue.

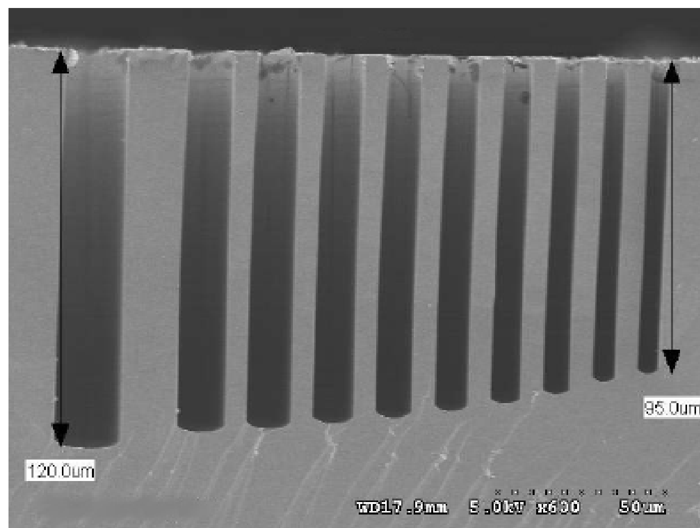

Figure 5.9 Etching testing in different etching areas [102]

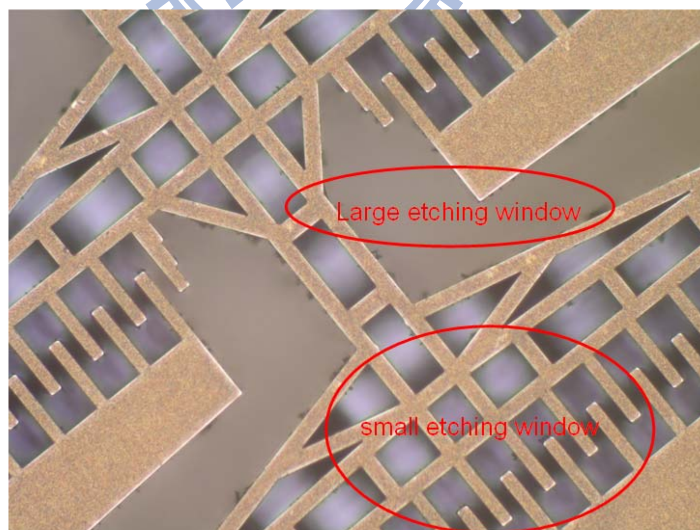

Figure 5.10 Illustration of bad etching uniform

5.4.2 Design of ICP uniformity improvement by mask layout design

The deviation of the etching profile shape is a very important consideration in the design of the proposed device. A change in the shape of the etching profile will significantly affect driving voltage, system stiffness, and loading capability. In ICP etching, as the aspect ratio of the etched trench increases, the effective removal of the passivation layer becomes more important, mainly because of ion flux decays toward the bottom of the trench, producing variations in the etching rate between the narrow and the wide etching areas. Since the developed structures are released by the ICP process, the variation in the etching rate results in different releasing times in different areas. Figure 5.11 shows a plot of the etching results of the ICP releasing process without mask design compensation. Overetching occurs in spacious etching areas when all device structures have been released. To solve this problem, a pre-etching layer and a dummy anchor are designed on the basis of the experimental results and adopted to fill spacious etching areas and ensure that the release process is completed in the entire structure simultaneously. The pre-etching layer in narrow spaces in the device, such as the space between comb fingers, is designed to reduce the etching time in the final releasing process. Dummy anchors are designed to extend the etching time in large etching areas. Figure 5.12 shows the optical microscopic image and SEM images of the device. This indicates that dummy anchors fill the large etching area to balance the release time.

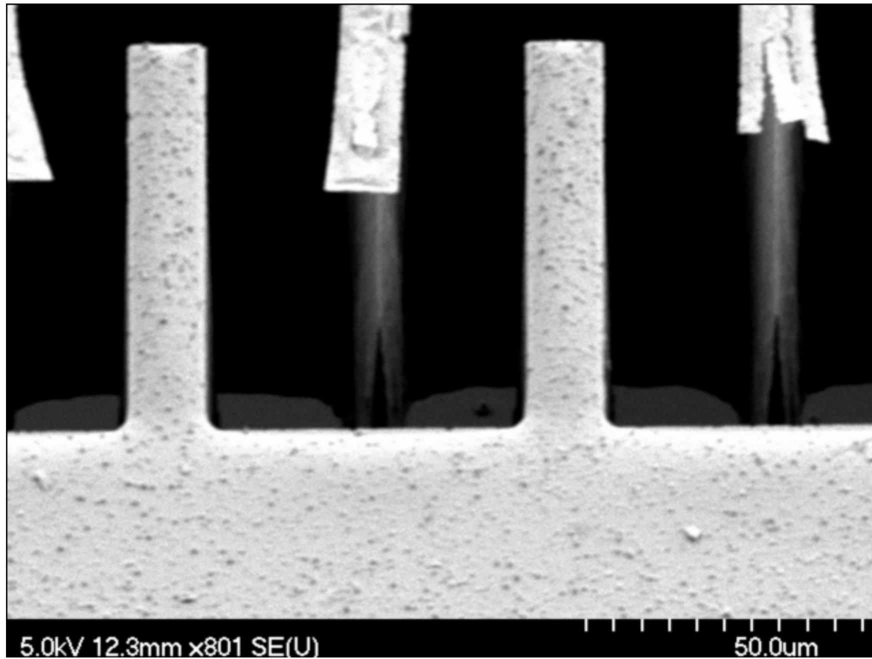

Figure 5.11 Phenomenon of overetching in ICP releasing process without compensation design.

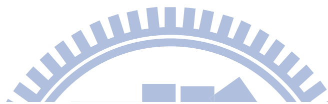

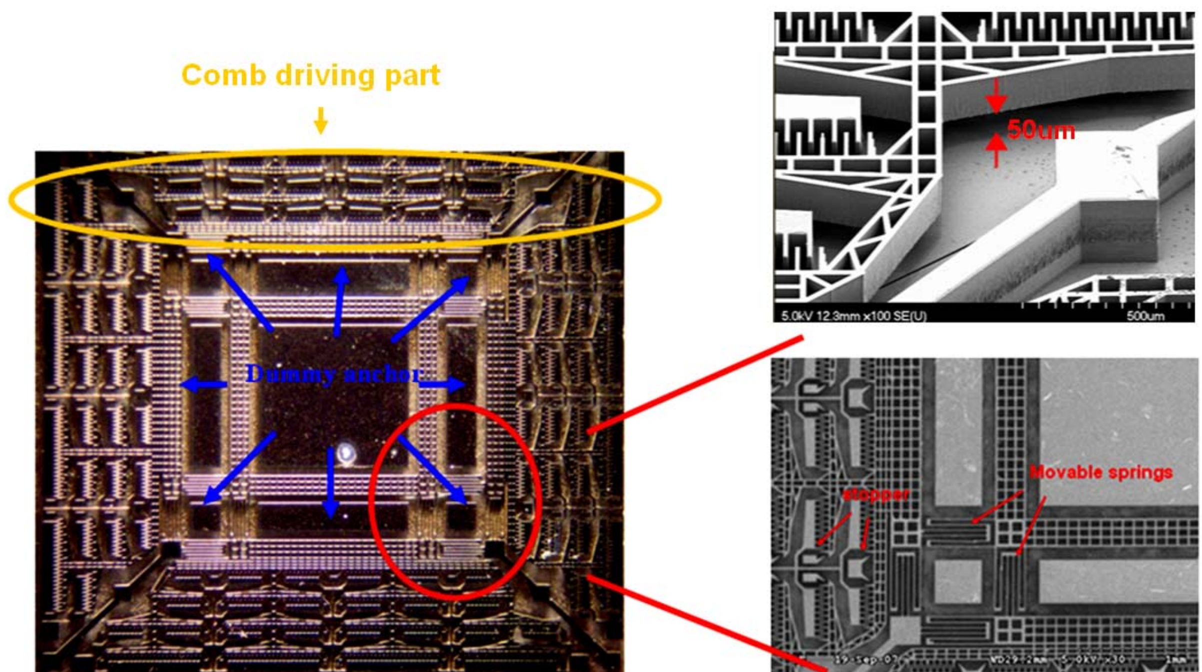

Figure 5.12. Optical image and SEM images of MEMS-based XY decoupling stage.

5.5 PACKAGING OF IMAGE STABILIZER

In this section, the flip-chip technique is used to combine an image sensor and an image stabilizer in a wire bonding task. Since the image stabilizer is entirely suspended in midair, bonding the sensor directly to the actuator is very difficult. Suspended springs of the decoupling XY stage may break. To solve this problem, dummy anchors are designed to carry the weight of the device and resist pressure during the flip-chip bonding process and wire bonding processes. Figure 5.13 shows the design of the dummy anchor and the flip-chip bonding process. A flip-chip bonder is applied to bond the image sensor onto the image stabilizer. Firstly, a 2 μm-thick layer of Al is sputtered onto the back of an image sensor to ensure the adhesion between the solder balls and the image sensor. Then, four solder balls of 100 μm radius are positioned in the bonding area and heated to 236 ℃ to soften them. The connection positions are designed to form a grid of structure for tracking the solder balls.

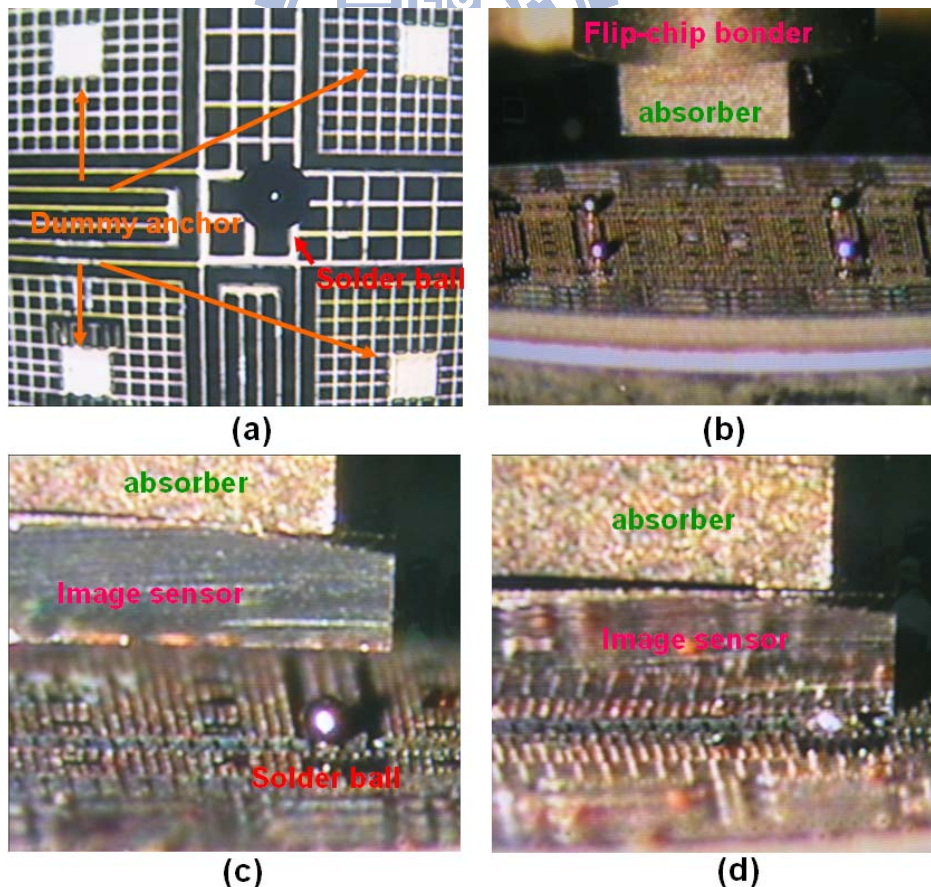

Figure 5.13 Flip-chip bonding process

Finally, the image sensor is pressed onto the solders such that they form contact with the image stabilizer. Since the dummy anchors and image stabilizer are in the same plane before bonding, the dummy anchors support the image sensor and prevent the suspended beam from snapping. Even though a small gap exists between the flattened solder balls during bonding, 150 μm-thick suspended springs are sufficiently strong to tolerate this defect. Figure 5.14 shows the actuator bonded on an image sensor. Consequently, dummy anchors also support the image sensor during wire bonding. In fact, the design of a dummy anchor not only solves the problem of the breaking of a spring when the sensor is connected to the actuator in the wire bonding process, but also ensures the uniformity of etching in the ICP process.

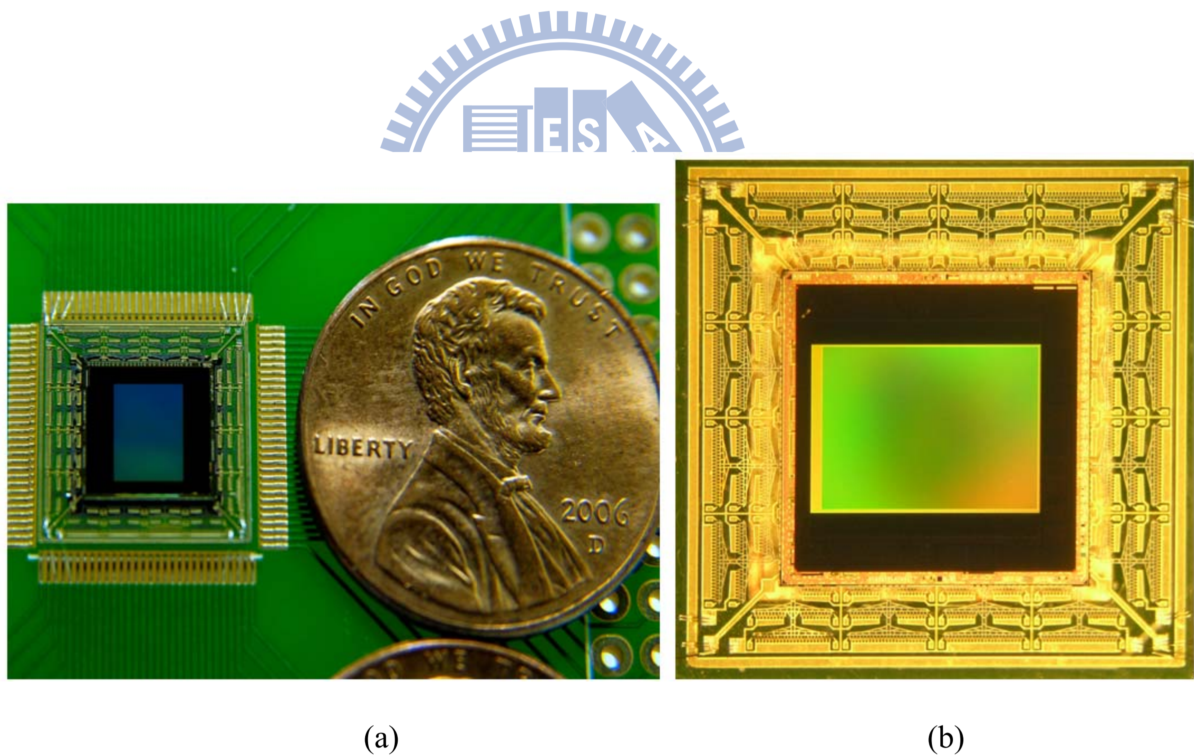

(a) (b)

Figure 5.14 Pictures of XY stage bonded to image sensor.

5.6 EXPERMENTAL RESULTS AND DISCUSSION

To demonstrate the performance of the fabricated device, a 2D decouple image stabilizer

was statically characterized. During the static driving test, the actuator was driven by a DC voltage. The displacement of the actuator was measured by using the WYKO measurement system. In the experiments, the displacement was 25 μm when a 84 V driving voltage was applied and with only a 0.2 μm displacement along the vertical axis. The experimental decoupling ratio of x-displacement to y-displacement is 125 and conforms to the system requirement (larger than 11.1). Figure 5.15 shows the variation in the displacement with corresponding driving voltage. Notably, when the driving voltage exceeds 84 V, the displacement of the image stabilizer is limited to 25 μm because stoppers prevents pull-in. The difference between the simulation and experimental results in static measurement which is mainly caused by the undercutting of comb fingers during the fabrication process. An undercutting phenomenon of comb fingers causes a larger gap between a pairs of fingers and reduced the electrostatic force when the device is driven at a specific voltage.

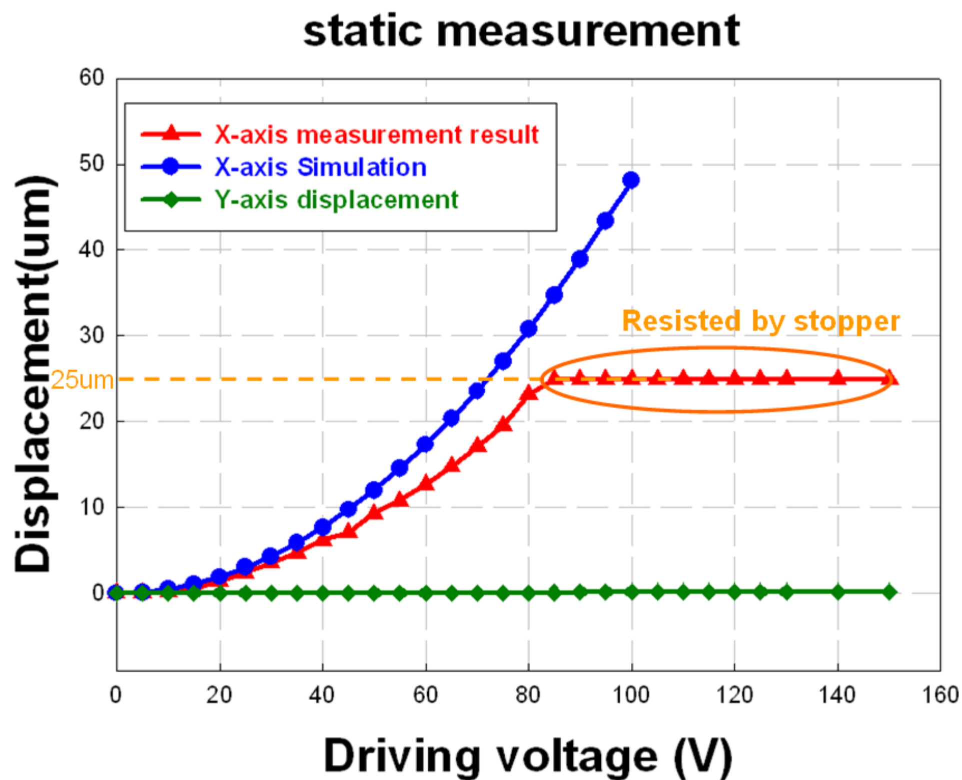

Figure 5.15 Static measurement of XY stage in X- and Y-directions when driven in X-direction only.

In dynamic characterization, an MMA(MEMS motion analyzer) system is set up to measure the resonant frequency of this image stabilizer. Figure 5.16 shows the measurements and the resonance frequency that reached 1.01 kHz. The experimental results were 21.1% lower than the simulated first natural frequency, 1280 Hz. The discrepancy is caused by the inaccuracy of the fabrication process. Further, the simulation model does not take into account the weight of solder balls; this factor may cause some diversity in the purposed desired.

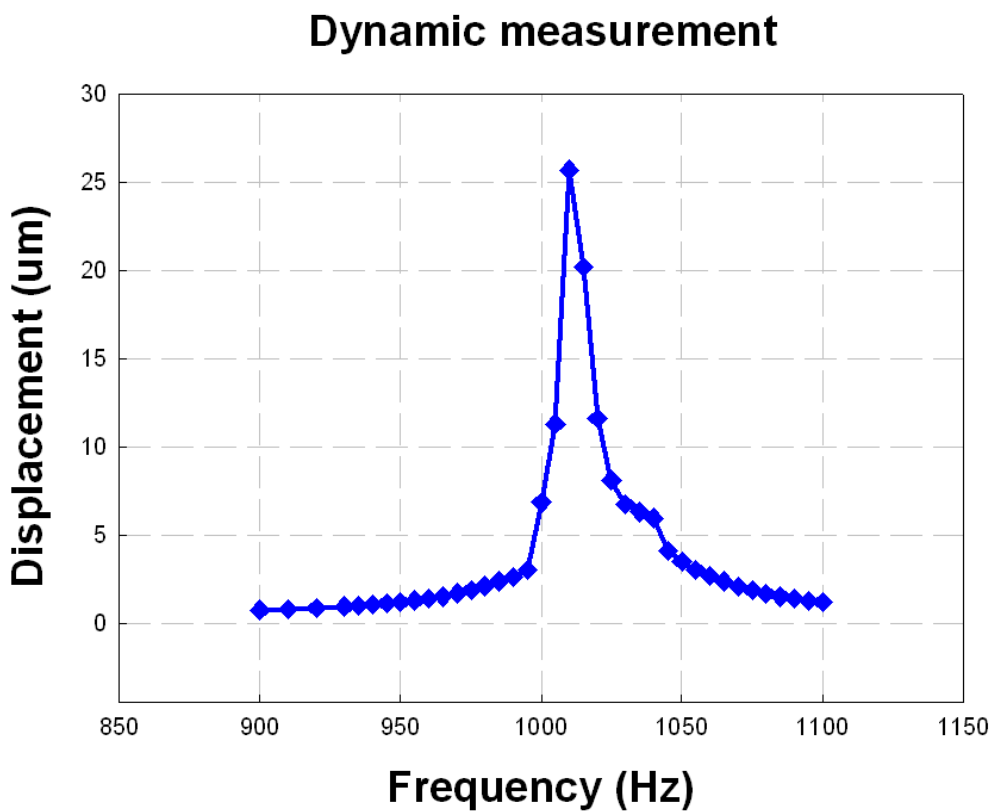

Figure 5.16 Measurement result of dynamic nature frequency.

5.7 SUMMARY

An integrated micro-decoupling XY-stage is designed, simulated, and fabricated. The integrated XY stage is designed to load a 3 megapixel image sensor fabricated by a through-silicon via technique. It can be applied in commercial cell phone cameras as an anti-shaking system. This proposed device is mainly composed of a silicon-based XY-stage, and a comb actuator, which is fabricated by a silicon-on-glass procedure with three ICP etching processes, and the flip-chip bonding technique. Precise calculation of ICP etching rate and a favorable pre-etching layer design can increased the yield of the fabrication process. Experimental results indicate that a driving voltage of 84 V can cause a displacement of 25 μm in the driving direction and a displacement of 0.2 μm in the vertical direction, consistent with the anti-shaking purpose. The variation between the simulation and the experimental results is caused by the undercutting of comb fingers resulted during the ICP etching process. A stopper effectively prevents the pull-in phenomenon. In dynamic characterization, the natural frequency of the designed XY stage is measured using an MMA system and found to be 1.01k Hz.

CHAPTER Ⅵ

DESIGN, FABRICATION, AND PACKAGING OF MEMS IMAGE STABILIZER

6.1 INTRODUCTION

In the previous chapter, we have designed, fabricated and demonstrated the decoupling XY stage applied in cell phone camera anti-shaking function. But it still exists some drawbacks in real application, such as signal transmitting, device packaging, and higher driving voltage. in this section, we will improve the above problems by utilizing the same decoupling concept but different fabrication and packaging process.

6.2 CONCEPT AND STRUCTURE DESIGN

The proposed MEMS-based image stabilizer has the same design specification with device introduced in the previous section. It focuses on designing a 2D decoupling actuator which can carry an image stabilizer with three mega pixels that can compensate for the blur image caused by human hand shaking when taking a photograph. The design concept is as follows:

6.2.1 Structure design of XY stage

Design of the proposed image stabilizer focuses on an excellent decoupling effect, suitable device size for suspending the image sensor and considering the signal output. To

achieve the anti-shaking function, this device must be designed as a decoupling structure to compensate for blur pixels distance caused by hand shaking motion without an additional moving deviation in another direction. Figure 6.1(a) shows a simple schematic diagram of the proposed decoupling main structure. When a single direction force F_x is added to the decoupling structure, only a displacement $\triangle x$ parallel to the driving force occurs and is almost without an additional displacement in another direction. Figure 6.1(b) illustrates a simplified mechanism of the operation of the proposed decoupling XY stage when different forces are applied in x- and y-directions. According to the decoupling design, displacements in x-and y-directions are $\triangle x$ and $\triangle y$, respectively, and with perfect mechanical isolation between the two orthogonal driving directions. The proposed design differs from the familiar SYMDC micro gyroscope structure in terms of anchor location. Inner anchor design can conceal the device driving part under the image sensor and effectively save the device size to be appropriate for packing into cell phones.

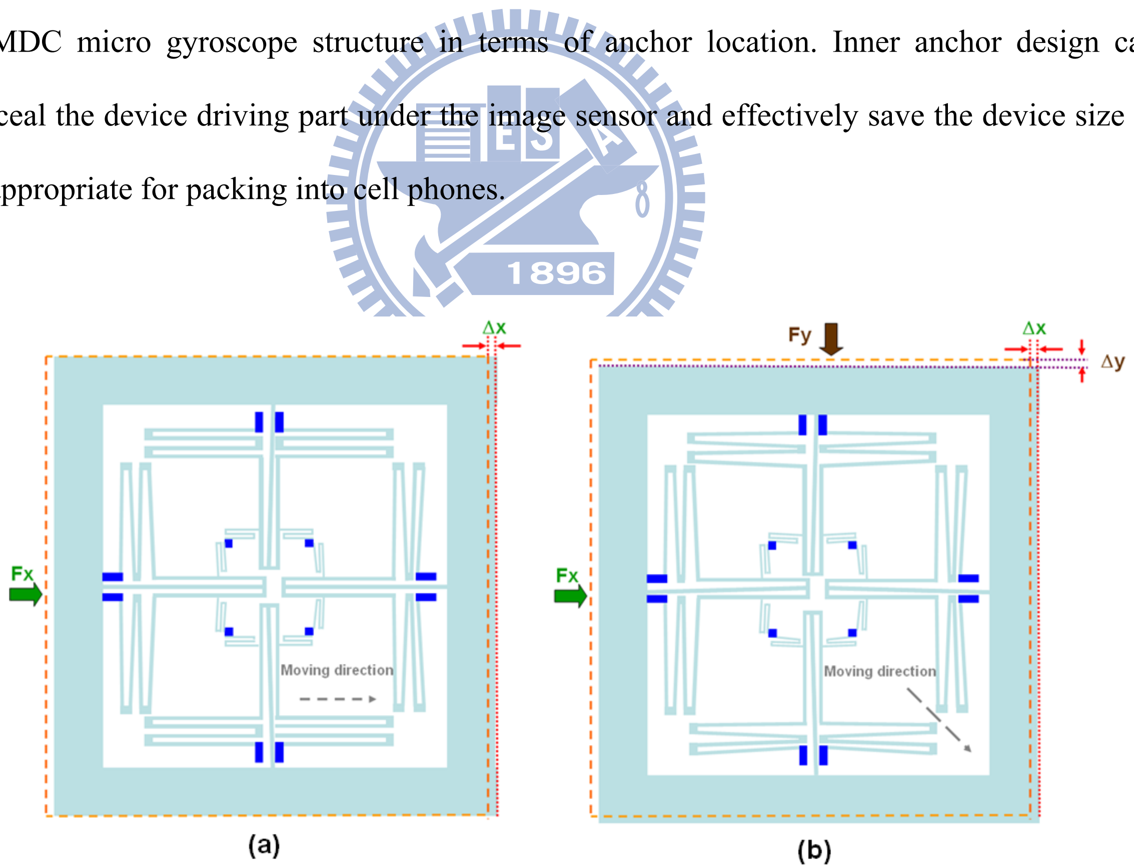

Figure 6.1 Illustration of driving modes of decoupling XY stage: (a) in only X-direction, and (b) in both X- and Y-directions.

To suspend a 6.36 × 6.24 × 0.1 mm^3 image sensor, this actuator is designed and fabricated with a device thickness of 100 μm, accompanied with a large stiffness effect between the z-direction and x or y direction separately. For the signal outputs of an image sensor, circuit routing must be patterned upon the device layer. The design of signal routing springs and pads ensures that the electrical connection is working. The routing springs and intermediary pad design can make an electrical connection with cell phone circuits by two times of wire bonding, from the image sensor pad to the electrical routing pad in the device structure and from the electrical routing pad in the device structure to the output PCB pad. Figure 6.2 schematically depicts the entire device design. According to this kinematic design shown in Figure 6.1, one main decoupling beam and three pairs of folded springs of various sizes are designed separately in each direction to satisfy decoupling requirements. Designs of inner comb-finger pairs and anchors can miniaturize the device size to comply with requirements for embedding in a photographic cell phone. Outer comb-driven finger pairs are designed as assisted-driving components to reduce the driving voltage for circuit integration in a cell phone module. The outer comb-driven assisted finger pairs are connected with the main structure by four folded springs. All of the comb-driven actuators are designed in a pull-only driving manner and are located in X+, X-, Y+, and Y- directions individually. For the symmetrical spring constants design, the electrical routings have a balanced layout as well as eight signal output springs and pads in each direction. The signal output springs are designed as thin as possible to ensure its small stiffness value with slight impact on the entire spring constant system. Because of the isolation layers and contact windows design, the electric potentials between the structure and the signal output are separated.

ES A 1896

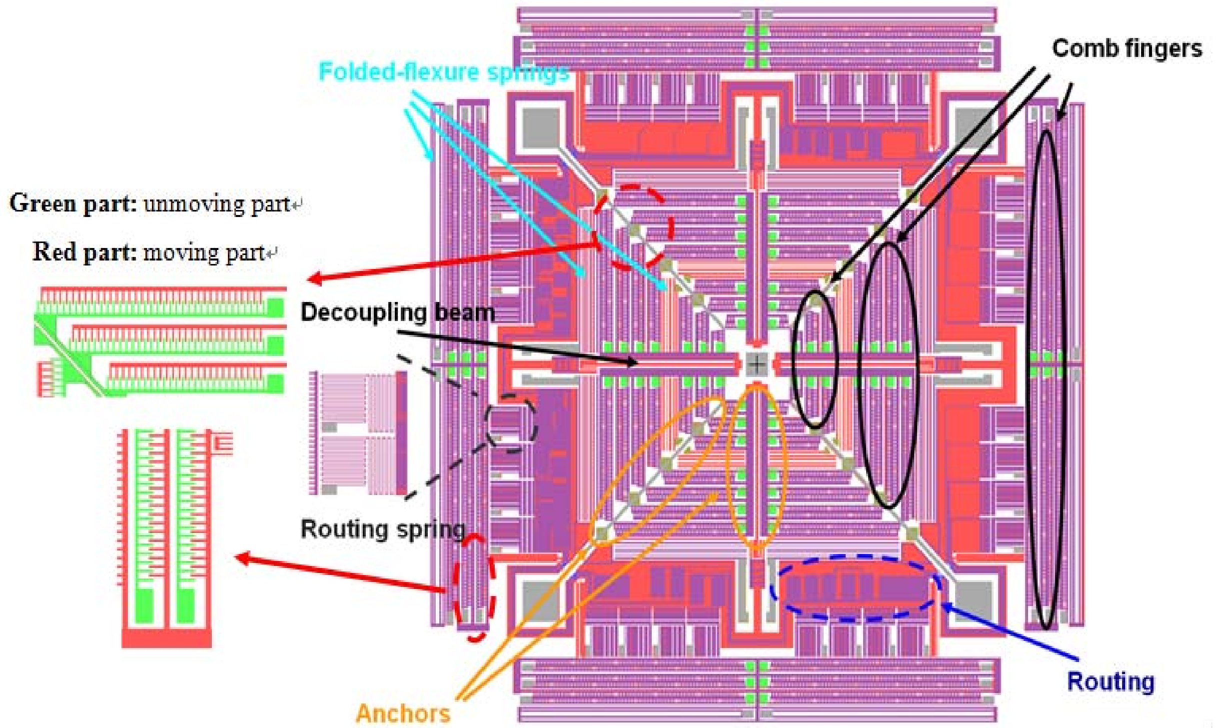

Figure 6.2 Structure design of XY stage.

6.2.2 Design and estimation of spring stiffness

Several suspension beams are designed in the proposed XY stage (Figure 6.3(a)). Based on consideration of the main actuating device, the decoupling beams and the suspension beams are designed as flexure beams and folded beams. Figure 6.3(a) schematically depicts the decoupling and suspended structures. The suspension beams are composed of outside folded beams, inside folded beams, and inside assisted folded beams. Figure 6.3 schematically depicts the suspended structures. By considering the decoupling flexure beams (figure 6.3(b)), the stiffness in the lateral and axis direction can be expressed as

$$k_{x\,decoupling\ beam} = \frac{E_d h_d b_d^{\ 3}}{L^3_{\ d}} \qquad k_{y\,decoupling\ beam} = \frac{E_d h_d b_d}{L_d} \tag{6.1}$$

Where $k_{x\ decoupling\ beam}$ and $k_{y\ decoupling\ beam}$ are the stiffness of the decoupling beam in the lateral direction and axis direction, respectively. E_d denotes the young' modulus of the decoupling flexure beam, L_d, b_d, and h_d denote the length, width, and thickness of the decoupling flexure beam, respectively. The stiffness ratio of the decoupling beams can be expressed as

$$K_D = \left| \frac{k_{y\ decoupling\ beam}}{k_{x\ decoupling\ beam}} \right| = \left(\frac{L_d}{b_d} \right)^2 \tag{6.2}$$

Figure 6.3(c) schematically depicts the folded flexure beam. The stiffness of a folded beam in the lateral direction, $k_{x\text{-}folded\ beam}$ and its axial direction $k_{y\text{-}folded\ beam}$ can be obtained by Legtenberg et al [107].

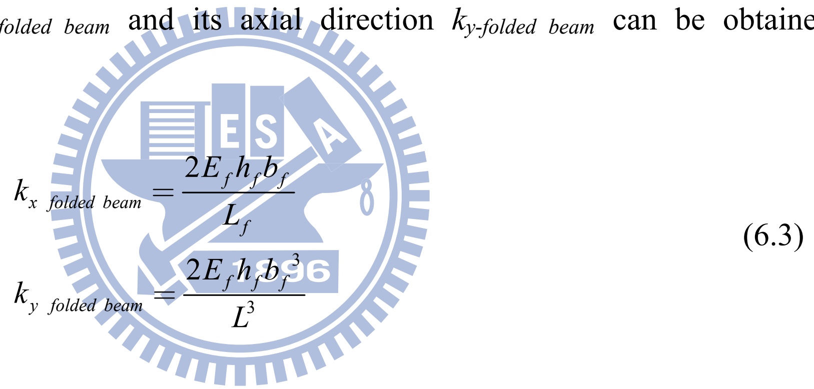

$$k_{x\ folded\ beam} = \frac{2E_f h_f b_f}{L_f}$$
$$k_{y\ folded\ beam} = \frac{2E_f h_f b_f^3}{L^3} \tag{6.3}$$

Where $k_{x\ folded\ beam}$ and $k_{y\ folded\ beam}$ denote the stiffness of the folded flexure beam in the lateral direction and axis direction, respectively. E_f denotes the young' modulus of the decoupling flexure beam, L_f, b_f, and h_f are the length, width, and thickness of the decoupling flexure beam, respectively. The stiffness ratio of the folded beams can be expressed as

$$K_F = \left| \frac{k_{y\ floded\ beam}}{k_{x\ floded\ beam}} \right| = \left(\frac{L_f}{b_f} \right)^2 \tag{6.4}$$

The total stiffness of the main suspension beam of XY stage in x- and y- direction can be expressed as

$$k_{x\,system} = 2k_{x\text{-decoupling beam}} + 2k_{x\text{-outside folded beam}} + 2k_{x\text{ inside folded beam}} + 2k_{x\text{-inside assisted folded beam}}$$
$$k_{y\,system} = 2k_{y\text{-decoupling beam}} + 2k_{y\text{-outside folded beam}} + 2k_{y\text{ inside folded beam}} + 2k_{y\text{-inside assisted folded beam}} \qquad (6.5)$$

Additionally, the stiffness ratio of the proposed image stabilizer k_{system} can be expressed as

$$K_{system} = \left|\frac{k_{x\,system}}{k_{y\,system}}\right| = \left|\frac{2k_{x\text{-decoupling beam}} + 2k_{x\text{-outside folded beam}} + 2k_{x\text{ inside folded beam}} + 2k_{x\text{-inside assisted folded beam}}}{2k_{y\text{-decoupling beam}} + 2k_{y\text{-outside folded beam}} + 2k_{y\text{ inside folded beam}} + 2k_{y\text{-inside assisted folded beam}}}\right| \qquad (6.6)$$

According to the specifications of the proposed image stabilizer, as shown in Table 6.1, the system stiffness ratio of the proposed image stabilizer can be evaluated and simulated as 2.12 x 10^6.

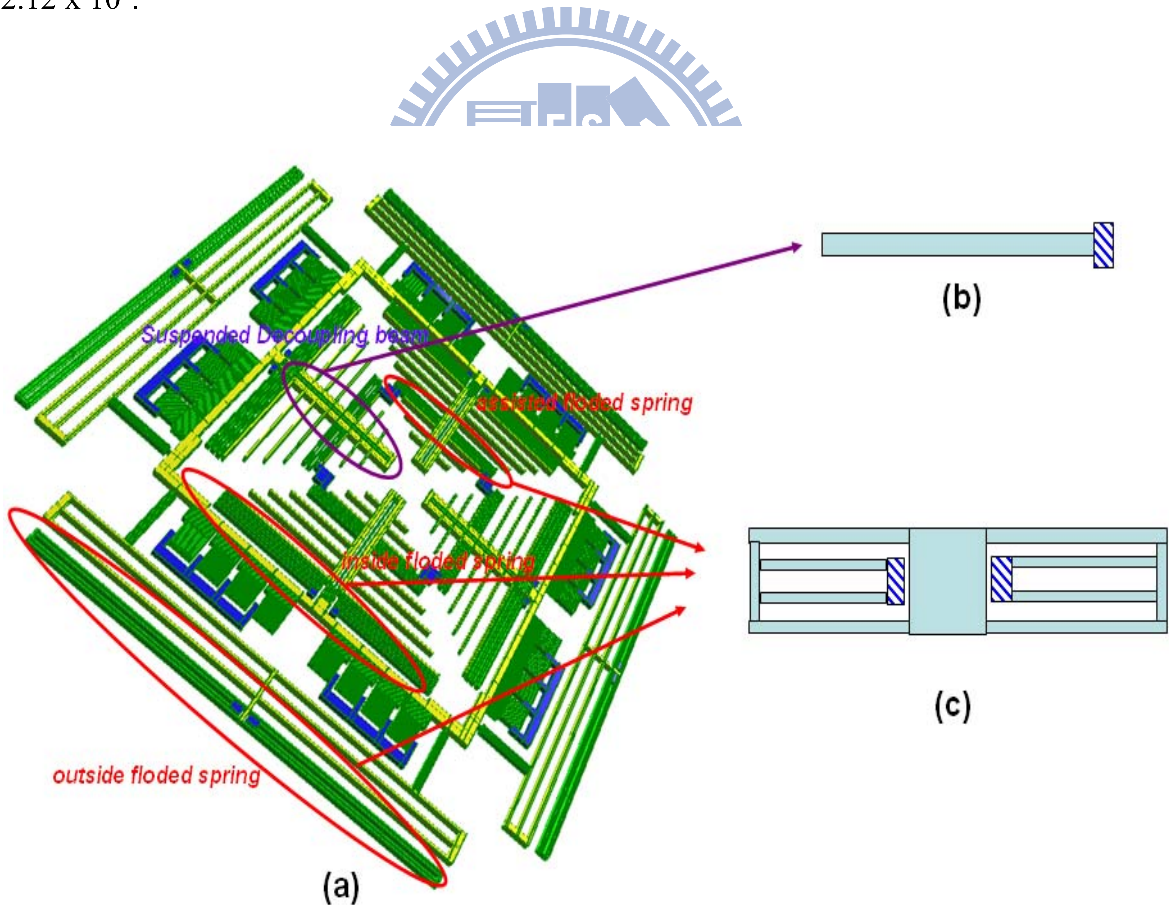

Figure 6.3 Illustrations of (a) decoupling structures, (b) decoupling flexure beams and (c) folded flexure beams.

Table 6.1 Specifications of the image stabilizer.

Specification	value
Device size(mm^2)	14 × 14
Image sensor size(mm^2)	6.36 × 6.64
Structure layer thickness(μm)	120
Gap of finger pair(μm)	10
Number of comb finger pair	1020
Width of the floded spring(μm)	15
Length of the outside floded spring (μm)	4000
width of the outside floded spring (μm)	20
Length of the inside floded spring (μm)	2280
width of the inside floded spring (μm)	12
Length of the inside assisted floded spring (μm)	1200
width of the inside assisted floded spring (μm)	14
Length of suspended decoupling beams(μm)	2700
width of suspended decoupling beams(μm)	26

6.3 SYSTEM MODELING AND FEA SIMULATION

This work elucidates and models the decoupling effect, stiffness and the natural frequency of the designed image stabilizer by developing and simulating a decoupling actuator based on use of IntelliSuite 8.2. During static simulation, this software simulates the moving distance in plane and the coupled mechanical interference of the image stabilizer in each orthogonal direction. In dynamic simulation, this software simulates the resonant frequency.

6.3.1 Simulation of the main structure decoupling of the proposed image stabilizer

This section describes the design and simulation of the decoupling structure. Owing to the complexity of simulating the entire device, the decoupling effect is simulated using the simplified decoupling composition, we do mechanical mesh (the mesh size is 10 μm) at each decoupling and folded beams in XY plane, but not meshing in z-axis because the ratio of thickness and width is high and our major concern is the decoupling effect in XY plane, and the totally element node number is 225032, the simulation results are shown in Figure 6. 4.

Notably, non-decoupling relative structures are excluded. Four major decoupling springs are designed inside the main structure to combine with the hidden driving comb finger pairs. The decoupling effect of the main structure is simulated based on the following actual boundary conditions: 1. The anchors and stators are ignored since those two parts are bonded with a substrate and do not influence the simulation results. 2. The shuttle, decoupling and flexure beams are suspended above the substrate, subsequently making the parts free. When simple modeling of the designed moving spring and a frame-loaded spring as the same size as the image stabilizer are made, an obvious decoupling effect occurs in x and y directions (Figure 6.4(a) and (b)), individually. During the simulation, a specific force F_y is set up in the Y-direction, resulting in a 30 μm displacement in the Y-direction. Simulation results indicate that only 0.55 μm moving displacement occurs in the X-direction. The simulation decoupling ratio of y displacement to x displacement displays an excellent decoupling effect in the design of the movable springs, which is significantly greater than the decoupling requirement.

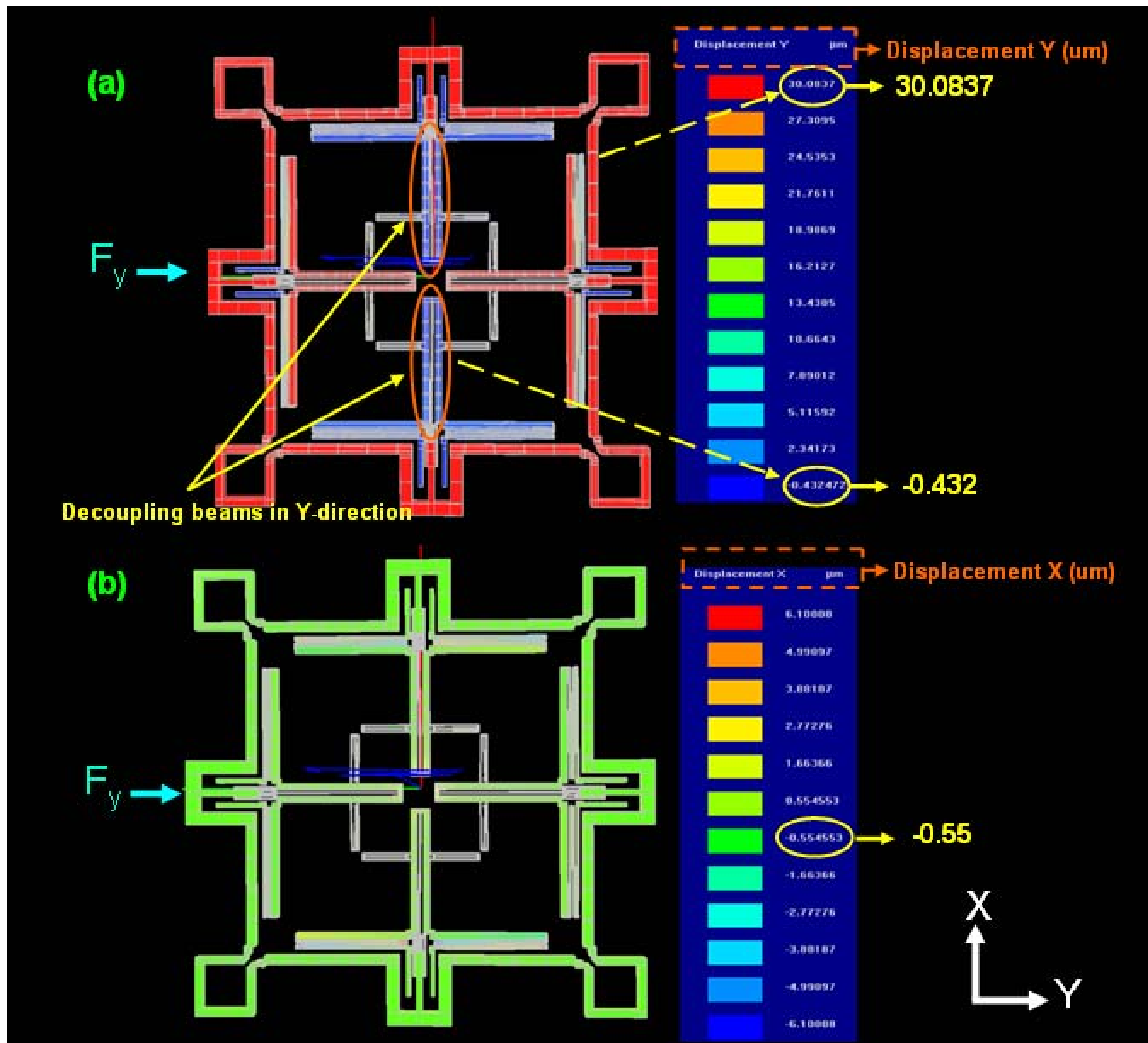

Figure 6.4 Schematic of decoupling simulation in (a) the Y-direction and (b) the X-direction when the main structure of image stabilizer is driven with outside force in the Y- direction.

6.3.2 Simulation of the resonant frequency for the proposed image stabilizer

The vibration characteristics are verified when the XY-stage is under dynamic loading by performing instantaneous analysis using the FEM software, Intellisuite 8.2, in order to determine the resonant frequency and modal shapes of the designed structure. In this simulation, the spring structures are completely reserved, and the weights of the XY stage and

the image sensor are calculated and equivalent to the other structures. Equation (6.7) shows the resonant frequency.

$$F_{resonant} = \frac{1}{2\pi}\sqrt{\frac{k}{M}} \tag{6.7}$$

Where k is the system stiffness of the image stabilizer, M is the overall weight of the image stabilizer, and $F_{resonant}$ refers to the resonant frequency of the image stabilizer.

The simulated resonant frequency of the first mode is 1130.1 Hz and with movement in X-direction; that of the second mode is 1213.1 Hz moving and with movement in Y-direction, while that of the third mode is 1353.52 Hz, which rotates in the XY plane. Although the device structure is symmetrical, the first model and second model resonant frequencies are not the same since the share of the image sensor attached on the image stabilizer is not symmetrical. The commonly frequency of human hand jitter is in range of 10~20 Hz, and it is necessary to avoid operating frequency close to resonant frequency for stability.

6.4 Fabrication Process

6.4.1 Fabrication processes of structure layer and substrate holder

Fabrication consists of structure formation, substrate holder formation, and the final combination of the said previous parts. Figure 6.5 depicts the structure formation fabrication process. In the part of structure formation, the structure definition, contact window opening, circuit routing and electric characterization isolation are completed in this segment. Fabrication begins with a 250 μm-thick 100 silicon wafer. The following step illustrates all of the fabrication processes:

a. In basic RCA cleaning, a thin 1μm-thick layer of Al is deposited on the front side and back side of Si wafer by DC sputtering (Figure 6.5(a));
b. During photolithography, the device structure and anchor shape are patterned in the front side and back side of the Si wafer. In the front side of Si wafer, photoresister layer as the device structure layer in Al etching process. In the back side of Si wafer, photoresister is patterned as the anchor shape layer for the anchor hard mask formation during Al etching process (Figure 6.5(b));
c. By Al wet etching, Al in the front side of Si wafer is patterned as the hard mask for device structure formation during the second ICP etching process. Al in the backside of Si wafer functions as the ICP hard mask during the first ICP etching process (Figure 6.5(c)). Notably, this Al layer in the front side is reserved to be the conductive layer after ICP etching process;
d. 1μm SiO_2 is deposited in the front side of Si wafer to identify the isolation layer between the structure layer and circuit routing layer (Figure 6.5(d));
e. After opening the contact windows by RIE etching, Al sputtering is executed again to be patterned as the circuit routing layer (Figure 6.5(e)~(f));
f. The first ICP etching process is performed to form the anchor shape in the backside of Si wafer with a depth of 130 μm (Figure 6.5(g));
g. 1μm SiO2 is finally deposited again upon the back side of Si wafer as the etching stop layer (Figure 6.5(h)).

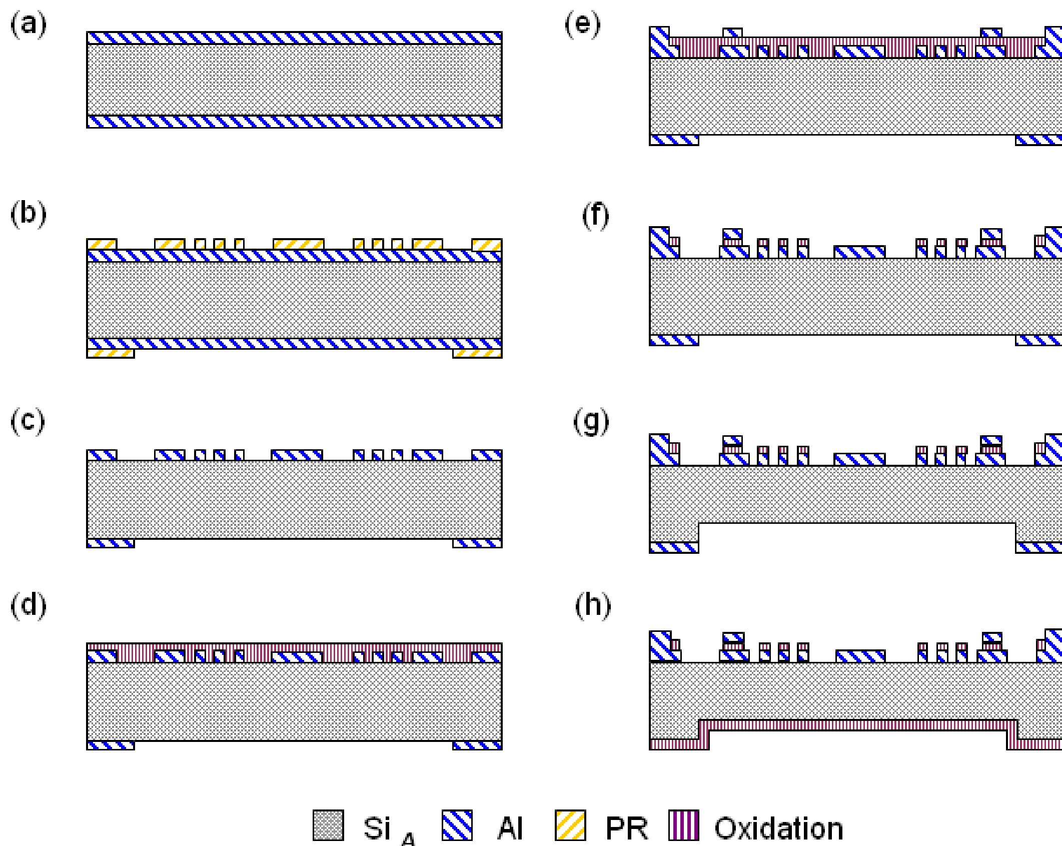

Figure 6.5 Fabrication process of device layer of the image stabilizer.

In substrate holder formation, based on consideration of wire bonding, the substrate holder is designed to be hollow under the device structure except for the anchor bonding area. The hollow shapes are utilized to be passed through by a wire bonding holder and support the suspended device during wire bonding process. Figure 6.6 shows the substrate holder formation and bonding process. Initially, Si_B is prepared for substrate holder formation and starts with the same RCA cleaning (Figure 6.6(a)). A thin 8000 Å-thick layer of Al is then deposited by DC sputtering (Figure 4.20(b)), and is patterned by a lithographic process as the hard mask for the substrate structure formation during ICP etching (Figure 6.6 (c)). Next, this Si wafer is treated with ICP etching until it is completely punched through (Figure 6.6 (d)) and Al is stripped by wet etching. Based on consideration of the etching uniformity of ICP

etching, 1 μm Cu is sputtered on the front and back sides of Si_B to benefit heat release during ICP etching process) (Figure 6.6 (e)).

The final step is combining of the device structure and substrate holder. This step is performed by flip- chip bonding, third ICP etching and HF vapor methods. Figure 6.6 (f)~(i) illustrates the process of the final task. Initially, 20 μm thick PDMS is spanned upon Si_B by a spinning coater (Figure 6.6 (f)). Next, Si_A and Si_B are combined by the flip-chip bonder and heated with 120 ℃ for 2 minutes (Figure 6.6 (g)). After completing the bonding process, the third ICP etching process is operated to form the device structure, and is completed at the etching stop layer (Figure 6.6 (h)). HF vapor etching is finally performed to release the device structure without any solution treatment. Device structures are released when the SiO_2 layer is etched by the HF vapor method; in addition, the sticking problem in the device is prevented during wet etching (Figure 6.6 (i)). Figure 6.7 and 6.8 show the photographs and SEM pictures of the fabricated image stabilizer, respectively. Figure 6.7 shows the proposed image stabilizer attached with a image sensor (without the wire bonding process), while Figure 6.7 (b) displays the entire image stabilizer. Figure 6.8 shows the SEM pictures of the proposed suspended devices.

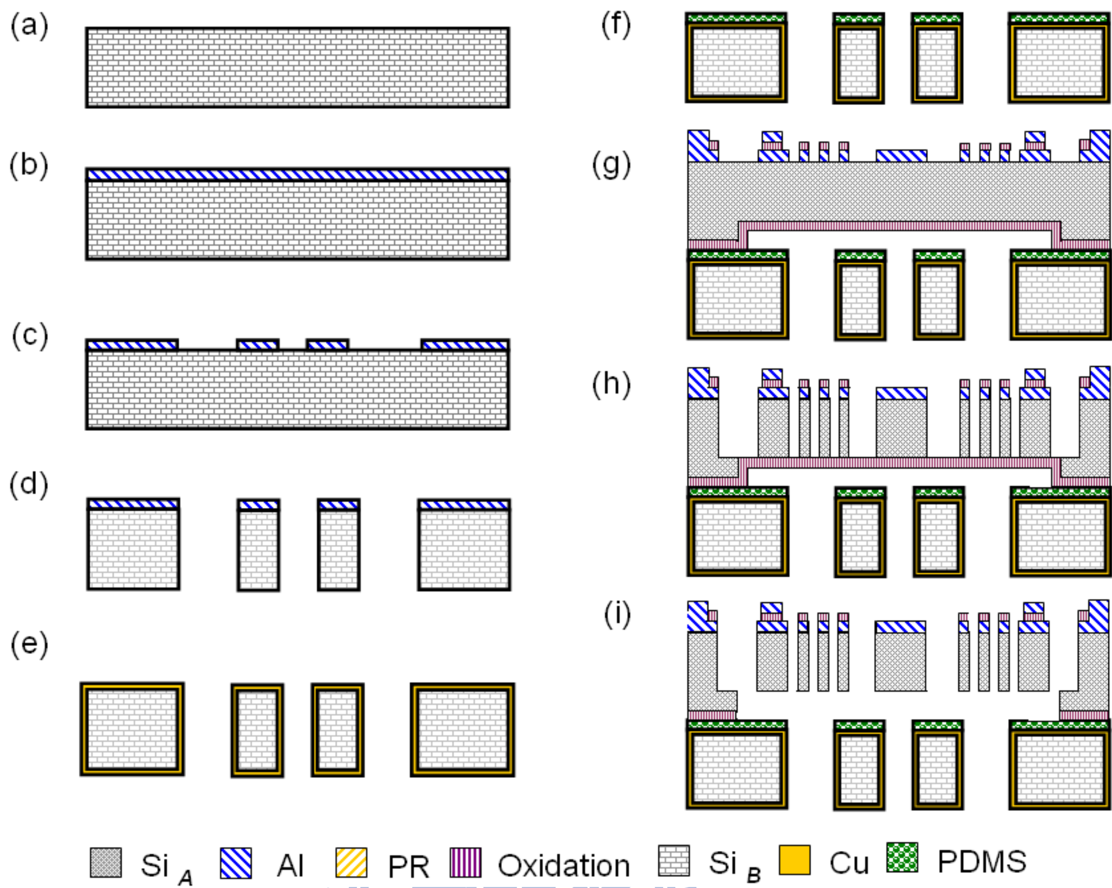

Figure 6.6 Fabrication process of image stabilizer

1896

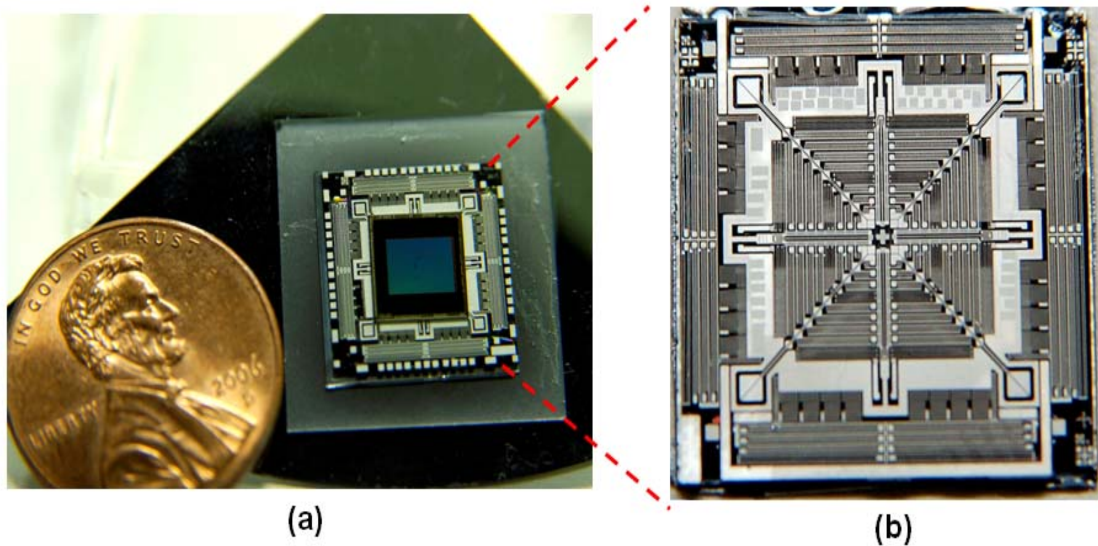

Figure 6.7 Photographs of image stabilizer

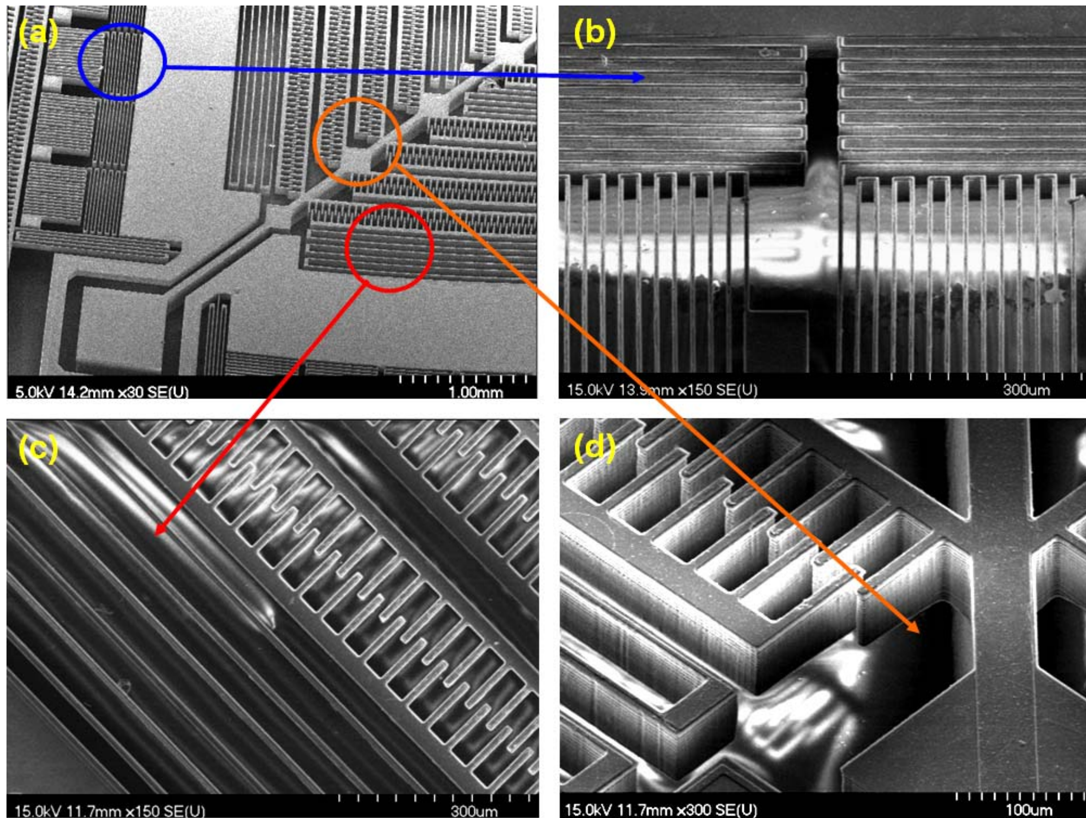

Figure 6.8 SEM pictures of part of image stabilizer: (a) suspended structure (b) signal springs (c) folded beams, and (d) comb flingers and anchors.

6.4.2 Wire bonding and device packaging

An image sensor is combined with the proposed image stabilizer in a wire bonding task by using the flip-chip approach. Since the proposed image stabilizer is entirely suspended in midair, attaching the image sensor directly to the actuator is extremely difficult. Suspension springs of the decoupling XY stage are extremely fragile, possibly breaking during wire bonding. To resolve this problem, wire bonding assisted holder (WBAH) is designed to carry the weight of the device and resist the bonding pressure during flip-chip bonding and wire bonding. Figure 4.23 displays the flip chip process of image sensor bonding and wire bonding packaging. The image sensor is bonded onto the proposed image stabilizer using a flip-chip

bonder. First, WBAH is attached under the proposed image stabilizer by a flip-chip bonder. Owing to the hollow design of the handle layer of the proposed image stabilizer, the suspended structures are fully propped up by WBAH (Figure 6.9(a)~(b)). Next, PDMS is utilized as an adhesive and dropped upon the special place of image stabilizer. By using the flip-chip bonder, the image sensor is attached upon the image stabilizer and treated with heat to 120 ℃ for 10 minutes to ensure that the sensor and stabilizer are fully bonded together (Figure 6.9 (c)). Following the wire bonding process and removal of WBAH, the electric connection between the image sensor and suspended device are completed by the special package. Figure 6.10 depicts the package process captured from the flip-chip bonder monitor. Figure 6.10(a)~(c) show the combination of the image stabilizer and WNAH, while Figure 6.10 (d)~(f) show the combination and wire bonding processes of the image stabilizer and image sensor. Figure 13 shows the photographs and SEM pictures of the packaged image stabilizer. The image stabilizer carries the image sensor (Figure 6.11 (a) and (b)); in addition, wire bonding is performed to achieve electrical connection of image sensor (Figure 4.11(c) and(d)).

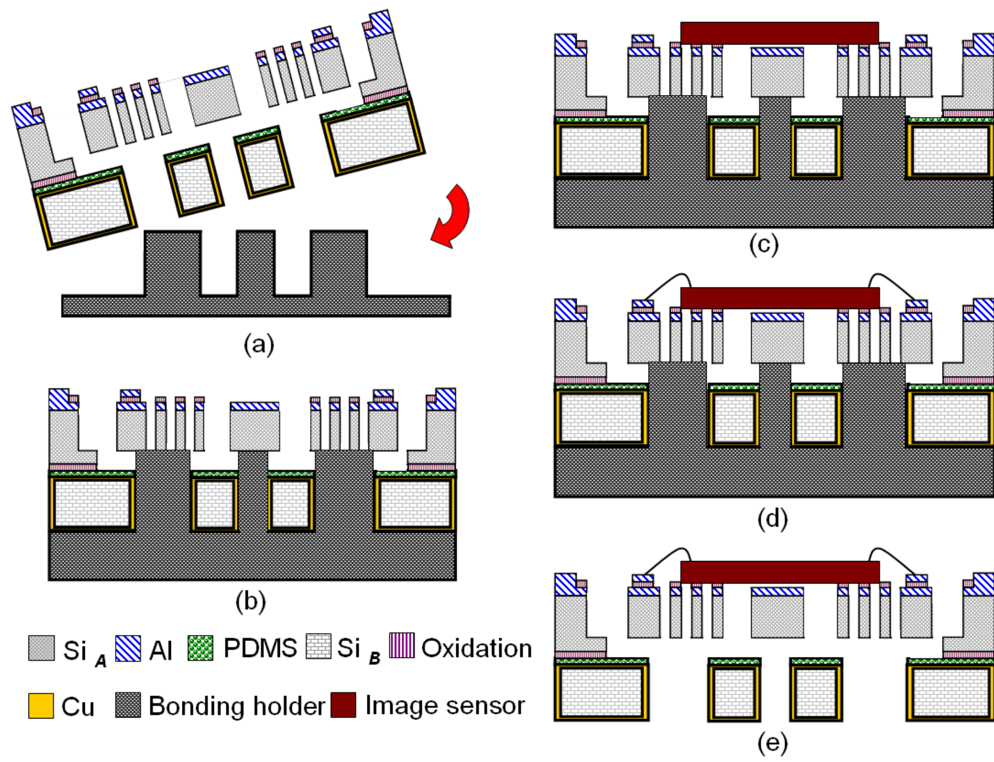

Figure 6.9 Package and wire bonding process of the image stabilizer.

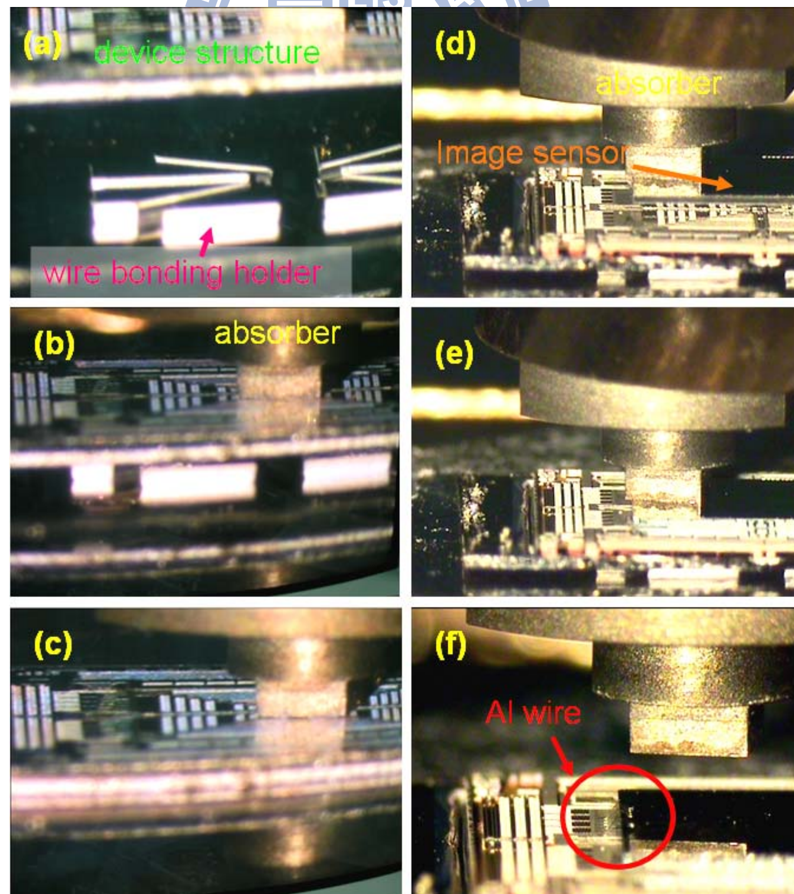

Figure 6.10 Photographs of package and wire bonding process of the image stabilizer.

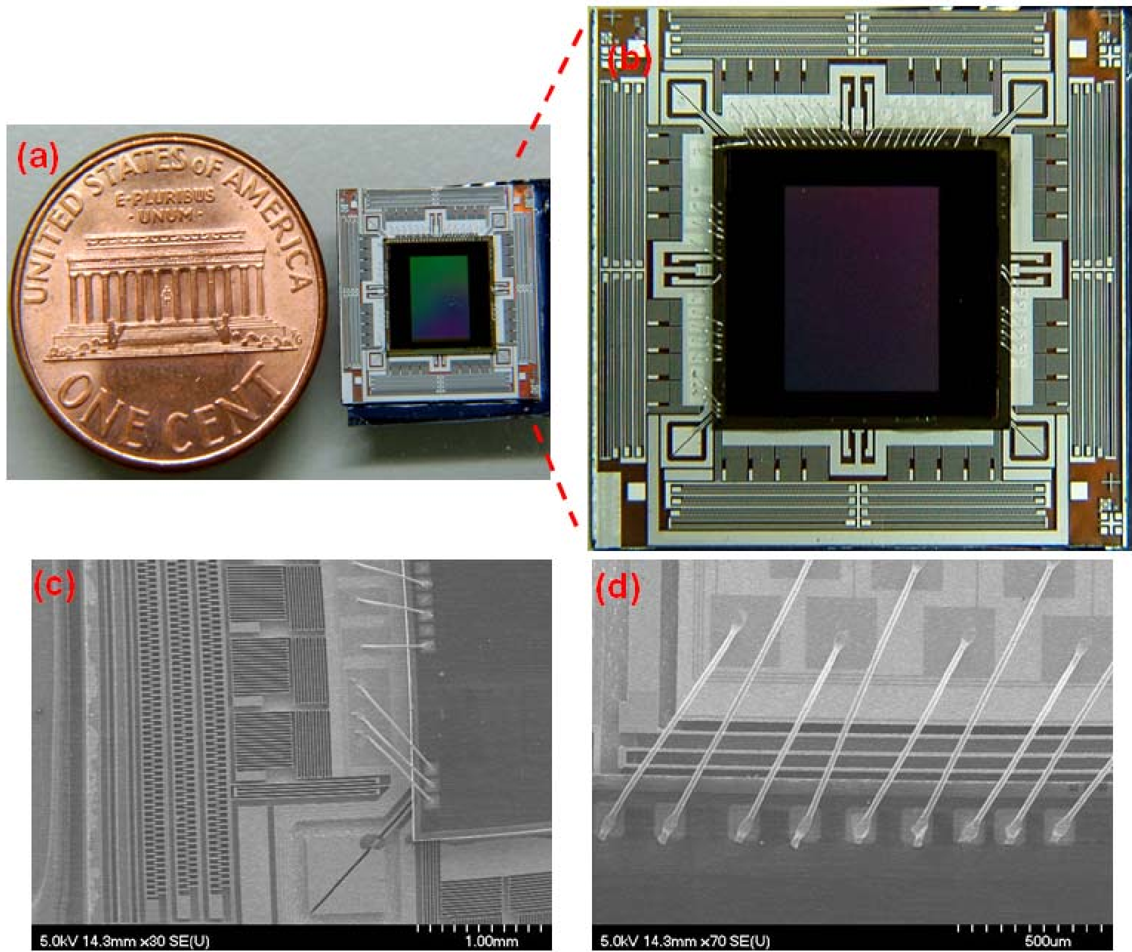

Figure 6.11 Photographs of image stabilizer with wire bonding package.

6.5 RESULTS AND DISCUSSIONS

Effectiveness of the 2-D decouple image stabilizer was examined to evaluate the performance of the fabricated device,. During the static driving test, the actuator was driven by a DC voltage. Displacement of the actuator was measured by White Light Interferometer WYKO measurement system. When a 51 V driving voltage was applied on the proposed device in the x-direction, moving displacement in the x-direction was 25 μm and with only 0.42 μm displacement along vertical axis y. When a 54 V driving voltage was applied on the purposed device in the y-direction, the moving displacement in the y direction was 25 μm and

with only 0.34 μm displacement along the vertical axis x. In the x-direction, experimental decoupling ratio of x displacement to y displacement is 59.52, which conforms to the system requirement that is larger than or exceeds 11.1. In the y-direction, experimental decoupling ratio of y displacement to x displacement is approximately 73.53 and conforms to the system requirement that is larger than 11.1 as well. Figure 6.12 presents the variation of the displacement with the driving voltage.

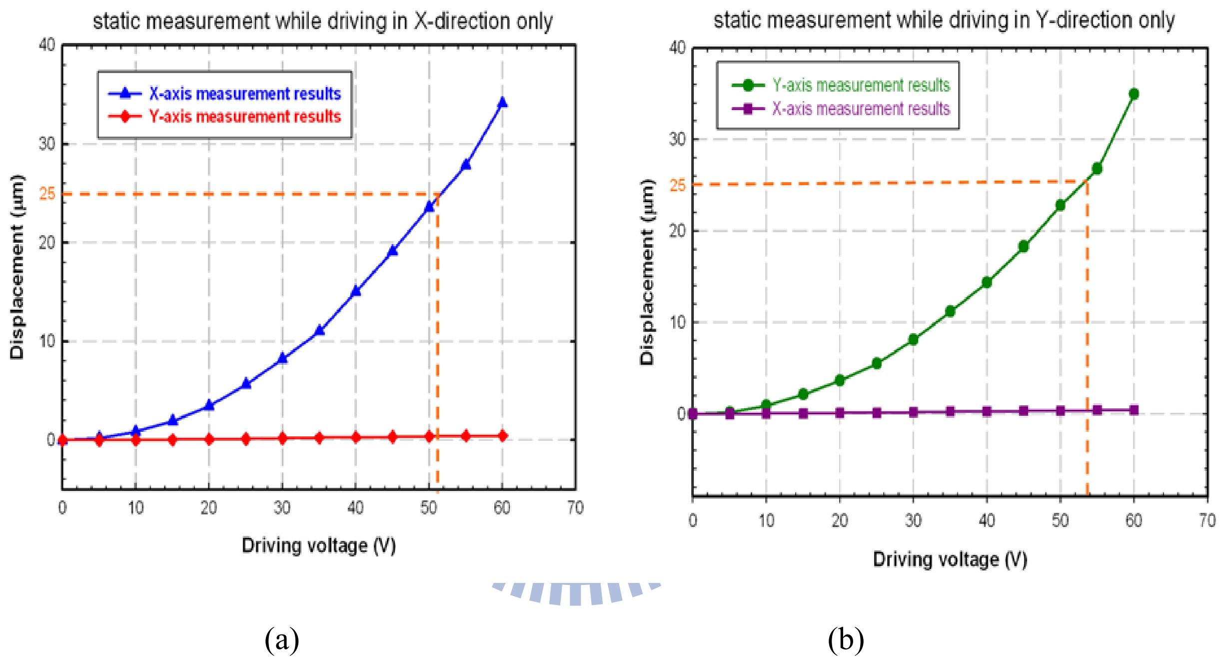

(a) (b)

Figure 6.12 Static measurement of XY stage in X- and Y-directions when driven in (a) X-direction only and (b) Y-direction.

In the dynamic characterization, an MMA system is set up to evaluate the resonant frequency of the proposed image stabilizer. Figure 6.13 plots the measurements, while the resonance frequency reaches 1.123 kHz. Experimental results indicate is 2.1% lower than the simulated first natural frequency, 1.123 kHz. The discrepancy is caused by the inaccuracy of the fabrication process and the weight variation of the image sensor. Furthermore, the simulation model does not consider the weight of PDMS, possibly causing some diversity in

the proposed subject.

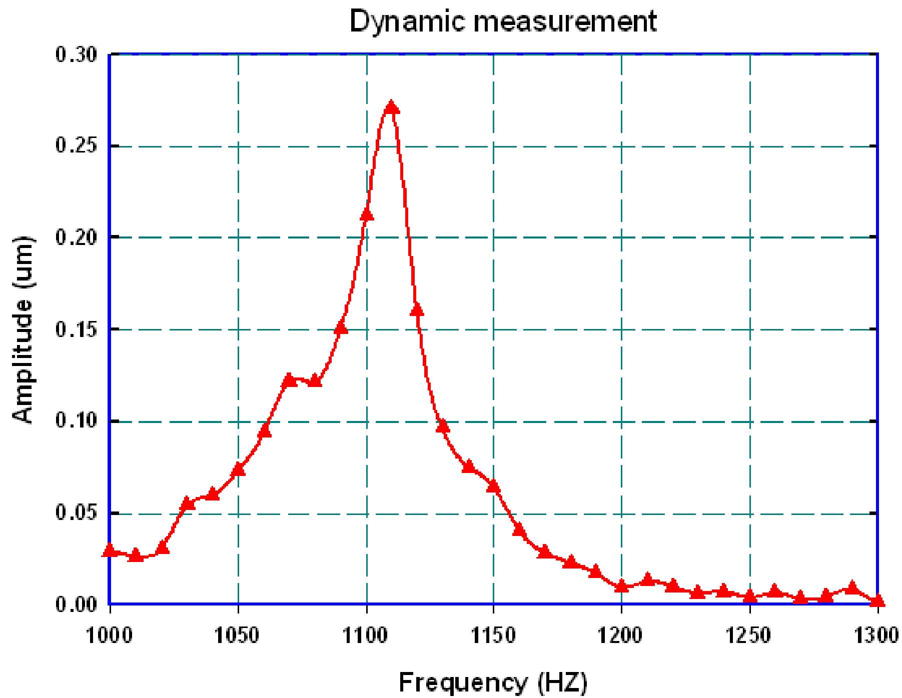

Figure 6.13 Measurement result of resonant frequency.

1896

6.6 SUMMARY

This work describes the feasibility of designing, simulating and fabricating an integrated micro decoupling XY-stage. The integrated XY-stage is designed to load a three megapixel image sensor. Based on the design of a wire bonding holder, the image sensor can be successfully bonded upon the image sensor. Additionally, the electrical signals of the image sensor can be connected and integrated with the output circuits according to the signal spring design. It can be applied in commercially available cell phone cameras owing to its anti-shaking function. The proposed device is mainly composed of a silicon-based XY-stage, a comb actuator, which is fabricated and packaged with three ICP etching processes, flip-chip bonding technique and a unique wire bonding method. Experimental results indicate that a

driving voltage of 51 V can cause a displacement of 25μm in the driving direction and a displacement of 0.42 μm in the vertical direction, which are consistent with the anti-shaking purpose. Similar results are measured and shown in the perpendicular direction because of the symmetry structure design. The variation between the simulation and the experimental results is caused by the undercutting of comb fingers that occur during ICP etching process and the disregard of the weight of a slight amount of PDMS., The natural frequency of the designed XY stage is measured using an MMA system and is 1.123k Hz.

6.7 CONCLUSION REMARK

In this chapter, the MEMS based image stabilizer are designed, fabricated, and measured. By the design of high aspect ratio structure, this image stabilizer is strong enough to load a $8 \times 8 \times 0.75\ mm^3$ image sensor, and with large output force to move with 25 μm. This image stabilizer is demonstrated that is suitable for anti-shaking function in cell phone camera application. Furthermore, by utilizing the flip-chip bonding process, we can design and package image stabilizer with small size and easy to package device into cell phone with thinner size.

CHAPTER Ⅶ

CONCLUSIONS

7.1 INTRODUCTION

In this dissertation, design, implementation and integration of Novel Micro Actuators for optical MEMS Applications have been explored. In the characteristic of CMOS MEMS phase shifter, by utilizing the high aspect ratio proof mass design, MEMS based phase shifter mirror are designed and fabricated with flatness mirror surface. Furthermore, vapor HF etching process offers the feasibility to manufacture phase shifter device with high fill factor and low driving voltage. In the characteristic of MEMS base image stabilizer, anti-shaking image stabilizers have been designed and actuated. As the measurement results, it offers the feasibility of new type anti-shaking function applied in cellphone camera. The contributions of this dissertation are summarized in the following section.

7.2 CONTRIBUTIONS

7.2.1 Post process was developed to improve CMOS MEMS structure flatness and reach high fill factor of micromirror.

In this dissertation, a self-design design post process was presented. By backside mask definition and backside ICP etching, suitable proof mass reservation can be kept under thin film structure. This proof mass reservation is multipurpose not only in flatness control in surface micromachining device but also in the frequency control of resonator.

7.2.2 MEMS Phase shifter and Image stabilizer were designed, fabricated and verified

In this dissertation, a novel type image stabilizer has been prevented. By utilizing the HF vapor etching process, high fill factor micromirror can be easy manufactured with additional packaging process, such as flip chip bonding. Furthermore, this device is fabricated in CMOS MEMS foundry process. It is simple to integrate the device part and circuit part in the same platform.

7.2.3 Novel type image stabilizer applied in cellphone camera for anti-shaking function

A novel type image stabilizer has been prevented in this dissertation. This image stabilizer is different from other anti-shaking function that is fabricated by MEMS fabrication process and with much smaller device size then others. Duce to the 0.5 mm thin device size, it is very suitable for packaging upon cell hone camera for physical anti-shaking compensation.

7.2.4 Novel packaging and wire bonding function assembled by flip-chip bonding technology.

In this dissertation, a novel packaging function was presented to combine image sensor and image stabilizer. By utilizing the backside wire bonding holder, we can package image sensor upon the suspension structures and without any structure damaging. Two successful samples were shown in this dissertation with sensor bonding and signal wire routing. The concept of the packaging holder can be applied in any suspension structure packaging such as proof mass change in resonator or accelerometer.

7.3 SUGGESSTIONS AND FUTURE WORKS

In this dissertation, the feasibility of MEMS devices integration applied in optical relative system had been demonstrated preliminarily. Two phase shifters and two MEMS based image stabilizer had been designed, fabricated. The relative actuation and measurement had been done for demonstration of excellent characteristics in the integration of optical MEMS devices. There are some suggestions for the future research.

In the part of micro phase shifter array:

a. More accurately ICP etching recipe control for accurate proof mass reserved

b. Mirror metal protection in HF vapor etching process for easy wire bonding.

c. Mirror device, driving, and control circuit integration in CMOS MEMS process for commercial application

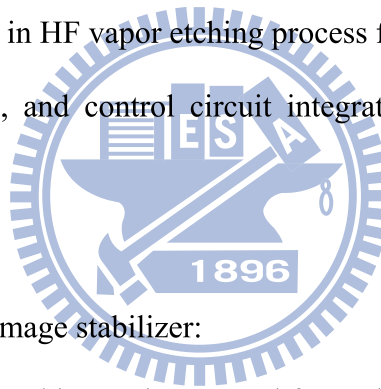

In the part of MEMS based image stabilizer:

a. More accurately ICP etching recipe control for undercutting prevention.

b. Real testing for anti-shaking function

c. Yield arising in ICP etching and wire bonding packaging.

REFERENCES

[1] R. P. Fenyman, "Infinitesimal Machinery," IEEE *Journal of Microelectromechanical Systems*, vol. 1, pp. 4-14, 1993.

[2] H. Baltes, O. Brand, G. K. Fedder, C. Hierold, J. G. Korvink, and O. Tabata, "Enabling Technology for MEMS and Nanodevices," pp. 4, 2002.

[3] T. J. Brosnihan, S. A. Brown, A. Brogan, C. S. Gormley, D. J. Collins, S. J. Sherman, M. Lemkin, N. A. Police, and M. S. Davis, "Optical IMEMS-A Fabrication Process for MEMS Optical Switches with Integrated On-Chip Electronics," *Transducers'03*, Bostin, MA, pp.1638-1642, June 2003.

[4] T. Juneau, K. Unterkofler, T. Seliverstov, S. Zhang, and M. Judy, "Dual-Axis Optical Mirror Positioning Using A Nonlinear Closed-Loop Controller," *Transducers'03*, Bostin, MA , pp. 560-563, June 2003.

[5] T. A Core, W. K. Tsang, and S. J. Sherman, "Fabrication Technology for an Integrated Surface-Micromachined Sensor," *Solid State Technology*, pp. 39-47, October, 1993.

[6] C. C. Beatty, " A Chronology of Thermal Ink-Jet Structures," T*ech. Digest Solid-State Sensor and Actuator Workshop*, Hilton Head Island, SC, pp.489-493, 1995.

[7] Dudaicevs, M. Kandler, Y. Manoli, W. Mokwa and E. Spiegel, "Surface micromachined pressure sensors with integrated CMOS read-out electronics," *Sensor and Actuator A: Physical*, vol. 43, pp. 157-163, May 1994.

[8] David W. Monk, and Richard O. Gale, "The Digital Micromirror Device for Projection Display," *Microelectronic Engineering*, vol. 27, pp. 489-493, 1995.

[9] ADI Introduces Industry's Smallest Accelerometers.

[10] S. M. Yuan, Z. Y. Zhou, G. H. Wang and C. G. Liu, "MEMS-based piezoelectric array microjet," *Microelectronic Engineering*, vol. 66, pp. 767-772, April, 2003.

[11] C. T. Ko, S. H. Tseng, and Michael S.-C. Lu, "A CMOS Micromachined Capacitive Tactile Sensor With High-Frequency Output," *Journal of Microelectromechanical Systems*, vol. 15, no. 6, pp. 1708-1714, Dec. 2006.

[12] Ludwig KA, Uram JD, Yang J, Martin DC, and Kipke DR, "Chronic neural recordings using silicon microelectrode arrays electrochemically deposited with a poly(3,4-ethylenedioxythiophene) (PEDOT) film," *Journal of Neural Engineering*, vol 3, pp. 59–70, 2006.

[13] J. E. Ford, V. A. Aksyuk, D. J.David J. Bishop, and J. A. Walker, "Wavelength add-drop switching using tilting micromirrors," J. Lightwave Technol., vol. 17, pp. 904–911, May

1999.

[14] L. Y. Lin, E. L. Goldstein, and R. W. Tkach, "Free-space micromachined optical switches for optical networking," *IEEE Journal of Selected Topics Quantum Electron*: Special Issue on Microoptoelectromechanical Systems (MOEMS), vol. 5, pp. 4–9, Jan.–Feb. 1999.

[15] W. Noell, L. Dellmann, C. Marxer,K.Weible, M. Hoffmann, and N. F. de Rooij, "Hybrid 4 X 4 optical cross connector based on MEMS switches and integrated optical waveguides," in Proc. IEEE/LEOS Int. Conf. on Optical MEMS, Okinawa, Japan, 2001, pp. 13–14.

[16] L. Fan, S. Gloeckner, P. D. Dobblelaere, S. Patra, D. Reiley, C. King, T. Yeh, J. Gritters, S. Gutierrez, Y. Loke, M. Harburn, R. Chen, E. Kruglick, M. Wu and A. Husain, "Digital MEMS switch for planar photonic crossconnects," in Tech. Dig. Optical Fiber Conference (OFC 2002), Anaheim, CA,Mar. 2002, pp. 93–94.

[17] V. A. Aksyuk, S. Arney, N. R. Basavanhally, D. J. Bishop, C. A. Bolle, C. C. Chang, R. Frahm, A. Gasparyan, J. V. Gates, R. George, C. R. Giles, J. Kim, P. R. Kolodner, T. M. Lee, D. T. Neilson, C. Nijander, C. J. Nuzman, M. Paczkowski, A. R. Papazian, F. Pardo, D. A. Ramsey, R. Ryf, R. E. Scotti, H. Shea and M. E. Simon, "238 X 238 micromechanical optical cross connect," *IEEE Photonics Technology Letters*, vol. 15, pp. 587–589, Apr. 2003.

[18] Y. Mizuno, O. Tsuboi, N. Kouma, H. Soneda, H. Okuda, Y. Nakamura, S. Ueda, I. Sawaki, and F. Yamagishi, "A 2-axis comb-driven micromirror array for 3D MEMS switches," in Proc. IEEE/LEOS Int. Conf. on Optical MEMS, Lugano, Switzerland, 2002, Paper TuB4, pp. 17–18.

[19] D. M. Marom, D. T. Neilson, D. S. Greywall, N. R. Basavanhally, P. R. Kolodner, Y. L. Low, C. A. Bolle, S. Chandrasekhar, L. Buhl, S.-H. Oh, C.-S. Pai, K. Werder, H. T. Soh, G. R. Bogart, E. Ferry, F. P. Klemens, K. Teffeau, J. F. Miner, S. Rogers, J. E. Bower, R. C. Keller and W. Mansfield, "Wavelength-selective 1 X 4 switch for 128 WDM channels at 50 GHz spacing," in Tech. Dig. Optical Fiber Conference (OFC 2002), Anaheim, CA, Mar. 2002, Postdeadline Paper FB7.

[20] D. Hah, S. Huang, H. Nguyen, H. Chang, H. Toshiyoshi, and M. C.Wu, "A low voltage, large scan angle MEMS micromirror array with hidden vertical comb-drive actuators for WDM routers," in Proc. Tech. Dig. Optical Fiber Conference (OFC 2002), Anaheim, CA, Mar. 2002, pp. 92–93.

[21] D. Hah, S. Huang, H. Nguyen, H. Chang, J.-C. Tsai, H. Toshiyoshi, and M. C.Wu, "Low voltage MEMS analog micromirror arrays with hidden vertical comb-drive actuators," in

Proc. Tech. Dig. Solid-State Sensor, Actuator, and Microsystems Workshop, Hilton Head Island, SC, June 2002, pp. 11–14.

[22] T. Ducellier, J. Bismuth, S. F. Roux, A. Gillet, C. Merchant, M. Miller, M. Mala, Y. Ma, L. Tay, J. Sibille, M. Alavanja, A. Deren, M. Cugalj, D. Ivancevic, V. Dhuler, E. Hill, A. Cowen, B. Shen, R. Wood, "The MWS 1 X 4: a high performance wavelength switching building block," in Proc. Tech. Dig. 28th European Conference on Optical Communication (ECOC 2002), Copenhagen, Denmark, Sep. 8–12, 2002, Paper 2.3.1.

[23] C. Marxer, P. Griss, and N. F. de Rooij, "A multichannel variable optical attenuator for power management in fiber optic networks," in Proc. 10th Int. Conf. Sensors and Actuators (Transducer '99), Sendai, Japan, June 1999, pp. 798–799.

[24] M. J. Little, "Compliant MEMS and their use in optical components," in Proc. Tech. Dig. Optical Fiber Conference (OFC 2002). CA, Mar. 2002, pp. 95–97.

[25] C. J. Chang-Hasnain, "Tunable VCSEL," IEEE J. Select. Topics Quantum Electron., vol. 6, pp. 978–987, Nov. 2000.

[26] F. Sugihwo, M. C. Larson, and J. S. Harris Jr., "Micromachined widely tunable vertical cavity laser diodes," J. Microelectromech. Syst., vol. 7, pp. 48–55, Mar. 1998.

[27] D. Hah, T. Y. Huang, J. C. Tsai, H. Toshiyoshi, M. C. Wu, " Low-Voltage, Large-Scan Angle MEMS Analog Micromirror Arrays With Hidden Vertical Comb-Drive Actuators," *Journal of Microelectromechanical Systems*, vol. 13, no. 2, April, 2004.

[28] Wilfried Noell, Pierre-André Clerc, Laurent Dellmann, Benedikt Guldimann, Hans Peter Herzig, Omar, Manzardo, Cornell Marxer, Ken Weible, René Dändliker, and Nico de Rooij, "Applications of SOI-based optical MEMS," *IEEE Journal of Selected Topics in Quantum Electronics*, vol. 8, No. 1, pp. 148-154, Jan./Feb. 2002.

[29] R. A. Conant, J. T. Nee, K. Y. Lau, and R. S. Muller, "Dynamic Deformation of Scanning Mirrors," O*ptical MEMS 2000, IEEE/LEOS Intern. Conf. on Optical MEMS*, Tech. Digest, 49-50, Kauai, HI, 20-24 August 2000.

[30] R. A. Conant, J. T. Nee, K. Y. Lau, and R. S. Muller, "A FLAT High-Frequency Scanning Micromirror," *Solid-State Sensor and Actuator Workshop*, Hilton Head, South Carolina, pp. 6-9 , June 2000.

[31] P. Kopka, M. Hoffmann, and E. Voges, "Coupled U-shaped cantilever actuators for 1 x 4 and 2 x 2 optical fibre switches," *Journal of Micromechanics and Microengineering*, vol. 10, pp. 260-264, 2000.

[32] W. C. Chen, C. Lee, C. Y. Wu, and W. Fang, "A new latched 2×2 optical switch using bi-directional movable electrothermal H-beam actuators," *Sensors and Actuators A*,

Vol.123-124, pp. 563–569, 2005.

[33] C. Marxer, C. Thio, M. A. Gretillat, N. F. Rooij, R. Battig, O. Anthamatten, B. Valk and P. Vogel, “Vertical mirrors fabricated by deep reactive ion etching for fiber-optic switching applications”, *Journal of Microelectromechanical System*, Vol. 6, No. 3, 1997, pp. 277-285.

[34] W. H. Juan, and S. W. Pang, “High-Aspect-Ratio Si Vertical Micromirror Arrays for Optical Switching” *Journal of Microelectromechanical systems*, Vol. 7, No. 2, pp. 207-213, 1998.

[35] B. Schwartz and H. Robbins, “Chemical Etching of Silicon” *Journal of the Electrochemical Society*, 123 (12), pp. 1903-1909.

[36] H. Linde, C. Whiting and D. Benoit, “Etch Characteristic of Various Materials in Ethanolamine Etchants,” *Sensors and Actuators A*, vol. 63, pp.251,1997.

[37] A. Merlos, M. Acero, M. H. Bao, J. Bausells and J. Estsve, “ TMAH/IPA Anisotropic Etching C haracteristics,” *Sensors and Actuators A, vol. 37-38*, pp.737,1993.

[38] X. Li, M. Bao and S. Shen, “Maskless Etching of Three-Dimensional Silicon Structures in KOH,” *Sensors and Actuators A, vol. 57*, pp.47, 1996.

[39] R. T. Howe, R. S. Muller, K. J. Gabriel, W.S.N. Trimmer, ”Silicon micromechanics: sensors and actuators on a chip”, *IEEE Spectrum* Vol. 27, Issue: 7, Jul 1990 , p.p.29-31,34-35.

[40] M. Gad-el-Hak, “The MEMS handbook: Design and Fabrication,” chapter 8, pp. 8-3, 2003.

[41] M. Madou, “Fundamentals of MICROFABRICATION,” chapter 2, pp. 57, 2002.

[42] S. A. McAuley, H. Ashraf, L. Atabo, A. Chambers, S. Hall, J. Hopkins, G. Nicholls, “Silicon micromachining using a high-density plasma source,” *Journal of Physics d : Applied Physics*, Vol. 34, pp.2769-2774

[43] S. Jensen, “Inductively Coupled Plasma Etching for Microsystems,” PHD thesis, MIC-Department of Micro- and Nanotechnology Technical University of Denmark, pp. 3, 2004.

[44] F. L¨armer and A. Schilp, “Method for anisotropically etching silicon,” German Patent DE4241045,1992.

[45] 郭文正, “高深寬比懸浮結構之製程開發及在微機電式光開關之應用,” PH.D Thesis, 台灣大學機械工程研究所, pp.3, 2006

[46] The CIC CMOS MEMS design platform for heterogeneous integration, Chip Implementation Center, CIC, Taiwan, Document no. CIC-CID-RD-08-01, 2008.

[47] J. B¨uhlery, F. P. Steiner and H. Baltes, "Silicon dioxide sacrificial layer etching in surface micromachining," *Journal of Micromechanics and Microengineering*, vol. 7, pp. R1-R4, 1997.

[48] A. Witvrouw, B. D. Bois, P. D. Moor, A. Verbist, C. V. Hoof, H. Bender and K. Baert, "A comparison between wet HF etching and vapor HF etching for sacrificial oxide removal," *SPIE Proc.* 4174, pp. 130–141,2000.

[49] S. Kim, G. Barbastathis, and H. L. Tuller, "MEMS for Optical Functionality," *Journal of electroceramics*, Vol. 12, pp. 133–44, 2004.

[50] Van Kessel P F, L. J. Hornbeck, R. E. Meier and Douglass M R, "A MEMS-based projection display," *Proceedings of the IEEE* vol. 86, pp. 1687–704, 1998.

[51] A. Jain, H. Qu, S. Todd and H. Xie, "A thermal bimorph micromirror with large bi-directional and vertical actuation," *Sensors and Actuator A*, Vol. 122, pp. 9–15, 2005.

[52] H. Xie, Y. Pan, and G. K. Fedder, "Endoscopic optical coherence tomographic imaging with a CMOS-MEMS micromirror," *Sensors and Actuators A*, vol. 103, pp. 237–41, 2003.

[53] K. Anderson and K. Curtis, "Polytopic Multiplexing," *Optics Letters*, vol.29, pp. 12, 2004.

[54] H. Horimai and X. Tan, "Advanced collinear holography," *Optical Review*, vol. 12, pp. 90–42, 2005.

[55] A. Tuantranont, L. A. Liew, V. M. Bright, W. Zhang and Y. C. Lee, "Phase-only micromirror array fabricated by standard CMOS process," *Sensors and Actuators A*, vol. 89, pp. 124–34, 2001.

[56] F. Filhol, E. Defay, C. Divoux, C. Zinck and M. T. Delaye, "Resonant micro-mirror excited by a thin-film piezoelectric actuator for fast optical beam scanning," *Sensors and Actuators A*, vol. 123–124, pp. 483–9, 2005.

[57] I. Kanno, T. Kunisawa, T. Suzuki and H. Kotera, "Development of deformable mirror composed of piezoelectric thin films for adaptive optics," *IEEE Journal of Select Topic Quantum Electronics*, vol. 13, pp. 155–61, 2007.

[58] X. H. Xu, Y. Feng, B. Q. Li and B. R. Chu, "Integration of displacement sensor into bulk PZT thick film actuator for MEMS deformable mirror," *Sensors and Actuators A*, vol. 147, pp. 242–7, 2008.

[59] W. G. Wu, Q. H. Chen, G. Z. Yan, D. Q. Yin, Z. Y. Chen, Y. L. Hao, A. S. Xu and Y. Y. Wang, "Micro torsion mirror actuated by compound electrostatic driving structure," *Sensors and Actuators*, vol. 135, pp. 758–64, 2007.

[60] T. Fleischmann, K. Kubota, P. O. Vaccaro, T. S. Wang, S. Saravanan and N. Saito, "Self-assembling GaAs mirror with electrostatic actuation using micro-origami," *Physical E*, vol. 24, pp. 78–81, 2004.

[61] C. H. Ji, M. Choi, S. C. Kim, S. H. Lee, H. S. Kim, Y. Yee and J. U. Bu, "An electrostatic scanning micromirror with diaphragm mirror plate and diamond-shaped reinforcement frame," *Journal of Micromechanics and Microengineering*, vol. 16, pp. 1033–9, 2006.

[62] F. R. Hu, J. Yao,C. K. Qiu and D. J. Wang, "A new design of large stroke micro-deformable mirror actuated by electrostatic repulsive force," *Proc. 2nd Int. Conf. on Integration and Commercialization of Micro and Nanosystems (Hong-Kong, China)*, pp 117–20, 2008.

[63] A. P. Lee, C. F. McConaghy, G. Sommargren, P. Krulevitch and E. W. Campbell, "Vertical-actuated electrostatic comb drive with in situ capacitive position correction for application in phase shifting diffraction interferometry," *Journal of Microelectromechanical systems, vol.* 12, pp. 960–71, 2003.

[64] J. Pons, A. Rodriguez and L. M. Castaner, "Voltage and pull-in time in current drive of electrostatic actuators," *Journal of Microelectromechanical systems*, Vol. 11, pp. 196–205, 2002.

[65] N. Sabate, R. Rubio, C. Calaza, J. Santander, L. Fonseca, I. Gracia, C. Cane, M. Moreno and S. Marco, "Mirror electrostatic actuation of a medium-infrared tunable Fabry-Perot interferometer based on a surface micromachining process," *Sensors and Actuators A,* vol. 123–124, pp. 584–9, 2005.

[66] D. Hah, C. A. Choi, C. K. Kim and C. H. Jun, "A self-aligned vertical comb-drive actuator on an SOI wafer for a 2D scanning micromirror," *Journal of Microelectromechanical systems*, vol. 14, pp. 1148–56, 2004.

[67] M. H. Kiang, O. Solgaard, R. S. Muller and K. Y. Lau, "Surface-micromachined electrostatic-comb driven scanning micromirrors for barcode scanners," *Proc. IEEE MEMS '96 (San Diego, CA)*, pp 192–7, 1996.

[68] H. Choo, R. Kant, D. Garmire, J. Demmel and R. S. Muller, "Fast, MEMS-based, phase-shifting interferometer," *Proc. Solid-State Sensor and Actuator Workshop (Hilton Head, SC)*, pp 94–5, 2006.

[69] Y. C. Ko, J. W. Cho, Y. K. Mun, H. G. Jeong, W. K. Choi, J. W. Kim, Y. H. Park, J. B. Yoo and J. H. Lee, "Eye-type scanning mirror with dual vertical combs for laser display," *Sensors and Actuators A*, vol. 126, pp. 218–26, 2006.

[70] J. L. A. Yeh, H. Jiang and N. C. Tien, "Integrated polysilicon and DRIE bulk silicon micromachining for an electrostatic torsional actuator," *Journal of Microelectromechanical systems*, vol. 8, pp. 456–65, 1999.

[71] R. R. A. Syms, "Surface tension powered self-assembly of 3-D micro-optomechanical structures," *Journal of Microelectromechanical systems*, vol. 8, pp. 448–55, 1999.

[72] H. Xie, Y. Pan and G. K. Fedder, "A CMOS-MEMS mirror with curled-hinge comb drives," *Journal of Microelectromechanical systems*, vol. 12, pp. 450–7, 2003.

[73] R. Nowak, Y. Miyagawa, C. L. Li, S. Nakao, S. Maruno and S. Miyagawa, "Post-deposition reduction of internal stress in thin films: The case of HfN coatings bombarded with Au ions," *Materials Letters*, vol. 33, pp. 31–6, 1997.

[74] T. G. Bifano, H. T. Johnson, P. Bierden and R. K. Mali, "Elimination of stress-induced curvature in thin-film structures," *Journal of Microelectromechanical systems*, vol. 11, pp. 592–7, 2002.

[75] B. Mi, D. A. Smith, H. Kahn, F. L. Merat, A. Heuer and S. M. Phillips, "Static and electrically actuated shaped MEMS mirrors," *Journal of Microelectromechanical system,* vol. 14, pp. 29–36, 2005

[76] R. T. Chen, H. Nguyen and M. C. Wu, "A low voltage micromachined optical switch by stress-induced bending," *Proc. IEEE MEMS '99,* pp 424–8, 1999.

[77] National Applied Research Laboratories, National Chip Implementation Center, Hsinchu Science Park, Taiwan, ROC, http://www.cic.org.tw.

[78] R.D. Blevins, "Formulas for natural frequency and mode shape (Malabar, Fl: Krieger)," p.p. 156–60, 1984.

[79] J. H. Comtois, V. M. Bright, S. C. Gustafson, and M. A. Michalicek, "Implementation of hexagonal micromirror arrays as phase-mostly spatial light modulators," *Proc. SPIE*, vol. 2641, pp. 76–87, Oct. 1995.

[80] Y. H. Min and Y. K. Kim, "Modeling, design, fabrication and measurement of a single layer polysilicon micromirror with initial curvature compensation," *Sensors and Actuators A,* vol. 78, no. 1, pp. 8–17, Jan. 1999.

[81] M. A. Michalicek and V. M. Bright, "Flip-chip fabrication of advanced micromirror arrays," *Sensors and Actuators A*, vol. 95, no. 2–3, pp. 152–167, Jan. 2002.

[82] A. Tuantranont and V. M. Bright, "Segmented silicon-micromachined microelectromechanical deformable mirrors for adaptive optics," *IEEE Journal of Select Top Quantum Electronic*s, vol. 8, no. 1, pp. 33–45, Jan. 2002.

[83] I. W. Jung, U. Krishnamoorthy, and O. Solgaard, "High fill-factor two-axis gimbaled tip-tilt-piston micromirror array actuated by self-aligned vertical electrostatic combdrives," *Journal of Microelectromechanical systems*,, vol. 15, no. 3, pp. 563–571, Jun. 2006.

[84] V. M. Lubecke, F. Pardo, and V. A. Lifton, "Polyimide spacers for flip-chip optical MEMS," *Journal of Microelectromechanical systems*, vol. 16, no. 4, pp. 959–968, Aug 2007.

[85] D. H. Yeom, N. J. Park, and S. Y. Jung, "Digital controller of novel voice coil motor actuator for optical image stabilizer," in *Proc. Int. Conf. Contr., Automat. Syst.* 2007, Oct. 2007, pp. 2201–2206.

[86] K. Sato, S. Ishizuka, A. Nikami, and M. Sato, "Control techniques for optical image stabilizing system," *IEEE Transactions of the Consumer Electronics*, vol. 39, pp. 461-661, 2005.

[87] Yasuhiro Okamoto and Ryuichi Yoshida, "Development of linear actuators using piezoelectric elements, "*Electronics and Communications in Japan Part III*," vol. **81,** No. 11, p. 11, 1998.

[88] G. R. Chen, Y. M. Yeh, S. J. Wang, and H. C. Chiang, "A novel structure for digital image stabilizer," *IEEE Asia-Pacific Conf. on Circuits and Systems*, pp. 101-104, 2000.

[89] A. Mohamed, H. Elsimar and M. Ismail, "Analysis, and optimization of a CMOS vertical thermal actuator," *Symposium Proceeding on Design, Test, Integration and Packaging of MEMS/MOEM*, pp. 214-7, 2003.

[90] Popa, D.O.; Kang, B. H.; Wen, J.T.; Stephanou, H.E.; Skidmore, G.; Geisberger, A.;, "Dynamic Modeling and Open-Loop Control Of Thermal Bimorph MEMS Actuators," *in Proc. IEEE Conf. on Robotics and Automation*, Taipei, Taiwan, pp. 1470, 2003.

[91] A. Tuantranont, V. M. Bright, "Micromachined thermal multi- morph actuators fabricated by multi-users MEMS process," *in Proceedings of IEEE international conference on industrial technology (IEEE ICIT '02)*, vol. 2, pp. 941–944.

[92] C. H. Ji, Y. K. Kim and B. K. Choi, "Design and fabrication of electromagnetic micromirror with bulk silicon mirror plate and aluminum spring," *in Proc. IEEE/LEOS Optical MEMS*, pp. 97–8, 2000.

[93] J. Y. Park, Y. J. Yee, H. J. Nam and J. U. Bu, "Micromachined RF MEMS tunable

capacitors using piezoelectric actuators," *Microwave Symposium Digest, IEEE MTT-S International* vol. **3**, p. 2111, 2001.

[94] Y. Haddab, N. Chaillet, and A. Bourjault, "A Microgripper Using Smart Piezoelectric Actuators," *in Proceeding on 2000 Intelligent Robots and Systems*, vol. 1, pp. 659-664, 2000.

[95] E. S. HUNG and S. D. SENTURIA, "Generating efficient dynamical models for microelectromechanical systems from a few finite-element simulation runs," *Journal of Microelectromechanical Systems*, vol. **8**, pp. 280–289, 1999.

[96] X. H. Mu, M. Kahrizi and L. Landsberger , "Design &fabrication of out-of-plane electrostatic actuators for optical application," *in Proc. IEEE Canadian Conf. on Electrical and Computer Engineering (IEEE CCECE)*, vol. 1, pp. 133–6, 2003.

[97] J. C. Chiou and Y. J. Lin, "A Novel Large Displacement Electrostatic Actuator: Pre-stress Comb-drive Actuator," *Journal of Micromechanics and Microengineering*, Vol. 15, pp.1641-1648, 2005.

[98] W. C. Tang, T.-C. H. Nguyen, and R. T. Howe, "Laterally Driven Polysilicon Resonant Microstructures," *Proc. IEEE Micro Electro Mechanical Systems*, pp 53-9, 1989.

[99] S. E. Alper and T. Akin, "A single-crystal silicon symmetrical and decoupled MEMS gyroscope on an insulating substrate," *Journal of Microelectromechanical Systems*, vol. 14, pp. 707–17, 2005.

[100] J. Wu, R. Yue, X. Zeng, M. Kang, Z. Wang, and L. Liu, *in Proceedings of the first IEEE International Conference on Nano/Micro Engineered and Molecular Systems*, NEMS '06, Zhuhai, China, 18–21 January 2006, pp. 1152–1155

[101] D. Sachs, S. Nasiri, and D. Goehl, "Image Stabilization Technology Overview," [http://www.invensense.com/shared/pdf/ImageStabilizationWhitepaper_051606.pdf]

[102] C. Gormley, K. Y. Yallup, W. A. Nevin, J. Bhardwaj, H. Ashraf,P. H. Huggett and A. Blackstone, "State of the art deep silicon anisotropic etching on SOI bonded substrates for dielectric isolation and MEMS applications," *Fifth Int. Symp. Wafer Bonding Science, Technology and Applications,* 1999 (The Fall Meeting of the Electrochemical Society, USA)

CCHUNG 著作

Journal

1. Jin-Chern Chiou, Chen-Chun Hung, Li-Jung Shieh, "A Novel CMOS-MEMS Based Optical Electrostatic Phase Shifter Array with Low Driving Voltage and High Fill Factor," *IEEE Journal of Quantum Electronics(Accepted).(2.1 點)*
2. J. C. Chiou, Chen-Chun Hung, Chun-Ying Lin, "Design, Fabrication, and Actuation of MEMS-Based Image Stabilizer for Photographic Cell Phone Applications," *Journal of Micromechanics and Microengineering(Accepted). (2.1 點)*
3. J. C. Chiou, Chen-Chun Hung, Chun-Ying Lin and Y. J. Lin, "Design, Fabrication, and Actuation of MEMS-Based Image Stabilizer," *Journal of Japan Applied Physics*, vol. 49(2010)014201. *(1.2 點)*
4. Jin-Chern Chiou, Chen-Chun Hung, Li-Jung Shieh and Zhao-Long Tsai, "A Novel Electrostatic MOEMS Phase Shifter Array Using CMOS-MEMS Process," *Journal of Micro/Nanolithography, MEMS, and MOEMS*. vol. 9, 010303, Jan. 19. 2010. *(1.2 點)*
5. J. C. Chiou, Chen-Chun Hung and C. W. Chang, "Transparent microprobe array fabricated by MEMS hot embossing technology for photodynamic therapy application," *IEICE Electronic Express,* Vol. 7, No. 9, pp. 569-576, May. 10. 2010. (0.7)

Conference

1. J. C. Chiou, C. C. Hung, L. J. Shieh and Z. L. Tsai, "CMOS-MEMS based optical phase shifter array with high fill factor," Proceedings of the *IEEE/LEOS Optical MEMS and Nanophotonics 2009,* Clearwater beach, FL, USA, August 16-20, 2009.
2. . C. Chiou, L. J. Shieh, Y. J. Lin, C. C. Hung, S. W. Tsai and C. Y. Lin, "CMOS-MEMS electrostatic cantilever resonator with low driving voltage," Proceedings of the *13th Nano and Microsystem Technology Conference,* Hsinchu, Taiwan, July 9-10, 2009.
3. 洪振鈞、邱俊誠、林煒挺, "利用熱致動器驅動之雙開關光衰減器," *Optics and Photonics Taiwan 2004*, Chung Li, Taiwan, Dec. 18-19, 2004.
4. 邱俊誠、洪振鈞、謝禮忠、蔡櫂隆、侯冠州、張志瑋，"利用 CMOS MEMS 及後製程製作之靜電式低電壓驅動光相位調制器陣列"，第十三屆奈米工程暨微系統技術研討會，2009 年 7 月 9-10 日，新竹。

Patent

1. J. C. Chiou, Chen-Chun Hung and C. W. Chang, "A Rapid Batch Fabrication Method in Manufacturing Physiological Signal Sensing Chip" **American patent no. 7429333B2***(0.7 點)*